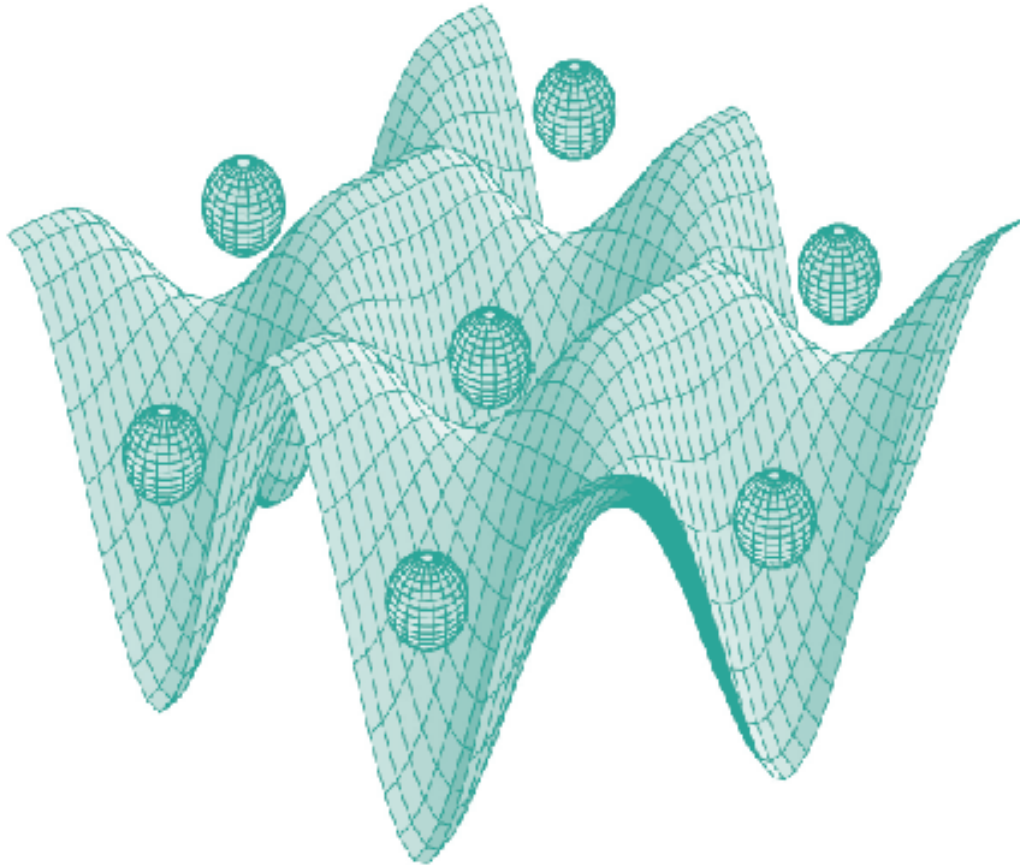




STUDIA UNIVERSITATIS  
BABEȘ-BOLYAI



# PHYSICA

---

2/2014

**STUDIA  
UNIVERSITATIS BABEŞ-BOLYAI  
PHYSICA**

**2/2014  
December**

---

**EDITORIAL OFFICE OF STUDIA UBB PHYSICA:**

1, M. Kogălniceanu St., Cluj-Napoca, ROMANIA, Phone: +40 264 405300

[http://www.studia.ubbcluj.ro/serii/physica/index\\_en.html](http://www.studia.ubbcluj.ro/serii/physica/index_en.html)

---

**EDITOR-IN-CHIEF:**

Professor Aurel POP, Ph.D., Babeş-Bolyai University, Cluj-Napoca, Romania

**EDITORIAL BOARD:**

Professor Simion AŞTILEAN, Ph.D., Babeş-Bolyai University, Cluj-Napoca, Romania

Professor Istvan BALLAI, Ph.D., The University of Sheffield, United Kingdom

Zoltan BALINT, Ph.D., Ludwig Boltzmann Institute Graz, Austria

Professor Titus BEU, Ph.D., Babeş-Bolyai University, Cluj-Napoca, Romania

Prof. Boldizsár JANKÓ, Ph.D., University of Notre Dame, USA

Professor Emil BURZO, Ph.D., Babeş-Bolyai University, Cluj-Napoca, Romania,  
member of Romanian Academy

Professor Vasile CHIŞ, Ph.D., Babeş-Bolyai University, Cluj-Napoca, Romania

Professor Olivier ISNARD, Ph.D., University J. Fourier & Institut Neel, Grenoble,  
France

Professor Ladislau NAGY, Ph.D., Babeş-Bolyai University, Cluj-Napoca, Romania

Professor Zoltan NEDA, Ph.D., Babeş-Bolyai University, Cluj-Napoca, Romania

Professor Jurgen POPP, Ph.D., Dr.h.c., Institute of Physical Chemistry, Friedrich-  
Schiller-University Jena, Germany

Professor György SZABÓ, Ph.D., Research Institute for Technical Physics and  
Materials Science, Hungarian Academy of Sciences, Budapest, Hungary

Professor Simion SIMON, Ph.D., Babeş-Bolyai University, Cluj-Napoca, Romania

Professor Romulus TETEAN, Ph.D., Babeş-Bolyai University, Cluj-Napoca, Romania

Professor Dietrich ZAHN, Ph.D., Dr.h.c., Technical University, Chemnitz, Germany

**EXECUTIVE EDITOR:**

Lecturer Claudiu LUNG, Ph.D., Babeş-Bolyai University, Cluj-Napoca, Romania

YEAR  
MONTH  
ISSUE

Volume 59 (LIX) 2014  
DECEMBER  
2

**S T U D I A**  
**UNIVERSITATIS BABEȘ-BOLYAI**  
**PHYSICA**

2

---

**STUDIA UBB EDITORIAL OFFICE:** B.P. Hasdeu no. 51, 400371 Cluj-Napoca, Romania,  
Phone + 40 264 405352

---

**CUPRINS – CONTENT – SOMMAIRE – INHALT**

SIMONA CINTA PINZARU, <i>Raman Spectroscopy at Babes-Bolyai University-Historical Retrospective</i> .....	5
AL. OKOS, P. BORDET, N. LEOPOLD, C. LUNG, A. POP, <i>Raman Spectroscopy of Pb(V<sub>1-x</sub>M<sub>x</sub>)O<sub>3</sub> Perovskite Compounds</i> .....	23
B. MARTA, C. LEORDEAN, T. ISTVAN, R. BARITCHI, S. ASTILEAN, <i>Optimization of Various Parameters for Graphene Synthesis by Thermal Chemical Vapor Deposition (CVD) on Copper Substrate</i> .....	35
RADU SILAGHI-DUMITRESCU, DANIELA CIOLOBOC, <i>Peroxide Binding to Fe(IV) Centers: Involvement of Fe(III)-Superoxide Redox Isomers</i> .....	47
I.J. HIDI, L. BAIA, J. POPP, M. BAIA, <i>Vibrational Study of 1-Phenyl-Pyrazole and 4-Me-1-Phenyl-Pyrazole Compounds</i> .....	59

LILIANA BIZO, <i>New Indium-Based Oxide with Oxygen-Deficient Fluorite-Type Structure: <math>In_{5.5}Sn_{0.5}Sb_{0.5}Te_{0.5}O_{12}</math></i> .....	69
D. CIURCHEA, O. COMȘA, C. COSMA, <i>Education and Training in Nuclear Sciences: First Steps towards European Integration</i> .....	79
RALUCA LUCHIAN, RÉKA-ANITA DOMOKOS, COSMINA CHIȘ, MIHAI VASILESCU, EMIL VINȚELER, VASILE CHIȘ, <i>Methods and Models for Calculating NMR Spectra: Levetiracetam as a Test Case</i> .....	85
R.V. BARITCHI, G. KATONA, B. MARTA, S. ASTILEAN, <i>Microwave-Assisted Synthesis of Carbon Nanoparticles Using a High Performance Microwave Reactor</i> .....	99

# **RAMAN SPECTROSCOPY AT BABES-BOLYAI UNIVERSITY – HISTORICAL RETROSPECTIVE**

**SIMONA CINTA PINZARU<sup>a</sup>**

**ABSTRACT.** This paper provides a historical description of the Raman spectroscopy research topics and developments at Babes-Bolyai University, since the first published results with the experimental spectrographic techniques to the current equipment and applications in a time span of 75 years. A short image gallery of the historical laboratory equipment from the personal collection of the author is provided. First results and applications as well as the Raman laboratory development is discussed in the context of international scientific development and cooperation. The founders of a real Raman Spectroscopy School at Babes-Bolyai University are acknowledged.

**Keywords:** *Raman spectroscopy, Babes-Bolyai University, Raman spectrograph, historical Raman equipment, Raman scientometry*

## **INTRODUCTION**

### **Historical context**

History Museum of the Babes-Bolyai University keeps documents proving the existence of the higher education in Cluj during the sixteenth to nineteenth century, where the Franz Joseph Hungarian University activity functioning in Cluj between 1872-1918 is particularly richly illustrated. In this

---

<sup>a</sup> *Babes-Bolyai University, Biomolecular Physics Department, Kogalniceanu 1, RO-400084 Cluj-Napoca, Romania, simona.cinta@phys.ubbcluj.ro*

time period Transylvania was part of the Austro-Hungarian Empire. The development of the Romanian University "Regele Ferdinand" (King Ferdinand) continued in the period 1919-1945. A document from 1933 clearly shows the Romanian name of the University of Cluj containing the Faculty of Science (Fig. 1).

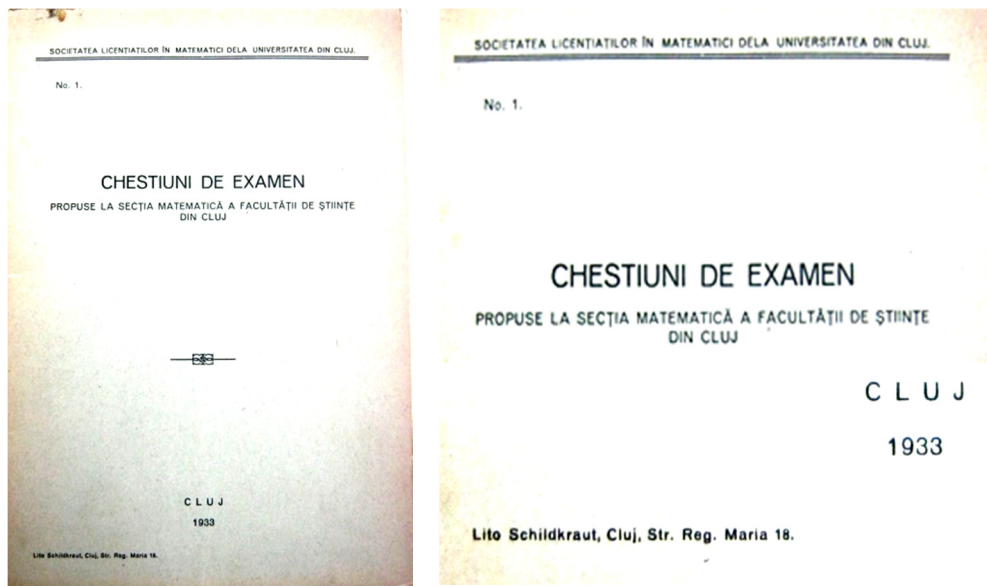


**Fig. 1.** Document cover dated 1933 and showing the Romanian Name of the University of Cluj which included the Faculty of Science. Images from the right side show details on the document.



After the instauration of the communism regime in Cluj, between 1945-1959 there were two separated universities, namely Romanian, called "Victor Babes" and Hungarian University "Bolyai". Documentary evidence kept in the History Museum of Babes-Bolyai University, emphasized that many of the teachers and researchers of these institutions were subjected to repression by the communist regime.

## First Raman spectroscopy evidence in Cluj

Shortly after the discovery of the Raman effect by the Sir Chandrasekhara Venkata Raman, an Indian physicist whose ground breaking work in the field of light scattering gained him the 1930 Nobel Prize for Physics [1], Hariton Tintea, a young assistant at the Institute of Molecular Physics, Acoustics and Optics in Cluj, presented his two doctoral theses in the Faculty of Science of the “King Ferdinand” University of Cluj, Romania (Fig. 2).

According to the document dated in February 24, 1940, the first part of the thesis treated the UV absorption of the toluene derivatives in vapor phase, while the Raman effect and the molecular structure was set as the second thesis (Fig. 2). To the best of our knowledge this is the first document proving the early Raman studies in the Babes-Bolyai University.

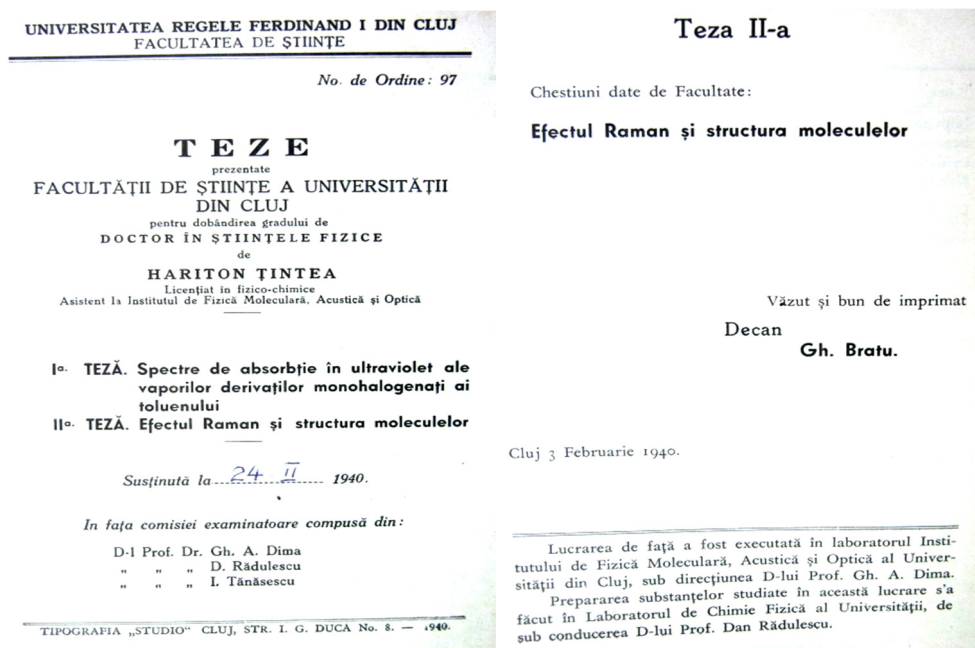


**Fig. 2.** Cover photos of the theses presented by Hariton Tintea at the “King Ferdinand” University of Cluj, 1940, stating “The Raman Effect and Molecular Structure”.

“King Ferdinand” University of Cluj was the former name of the current Babes-Bolyai University.

The theses being released in 1940, it is obvious that the experimental approaches were conducted in the first decade of the Raman effect discovery, suggesting a well-documented literature review for that time and the interest of the Romanian scientific community for the “new radiation”.

The radiation effect which bears Raman name was observed on February 28, 1928 and in the next day C. V. Raman published an article titled "A new radiation" in the Indian Journal of Physics [2]. The Nobel Prize motivation (1930) "*for his work on the scattering of light and for the discovery of the effect named after him*" bought in the scientific community a large interest for the new inelastic scattered radiation. The effect was first measured in liquids and later in crystals [2]. C. V. Raman investigated 60 liquids for light-scattering and made systematic studies of the phenomenon. He found that it was shown markedly by water, ether, all the monohydric alcohols and a few other compounds [3]. He noticed that the liquids which exhibit the effect are substances whose molecules are known to be polar.

### **International scientific context of Raman spectroscopy**

An exhaustive historical retrospective on the Raman spectroscopy worldwide was provided by Dr. Dr.H.C. Wolfgang Kiefer, Professor of Physical Chemistry at the University of Würzburg, Germany, currently retired while still working in his own-settled Eisingen-Lasel-Lab. He is recognized as one of the most active player on the international scene of Raman spectroscopy field worldwide and awarded contributor to the development of Raman spectroscopy. An appreciation of his huge contribution in the field was released on the occasion of his retirement on February 2006 [4] and five year later on the occasion of his 70-th anniversary [5]. In the brilliant talk at the XXIII International Congress on Raman Spectroscopy (ICORS) in Bangalore, India, the home country of C.V. Raman, W. Kiefer reviewed the very first results on Raman spectroscopy field. He was particularly focused on the first six editions of the International Conference on Raman Spectroscopy and presented original and well documented evidences on the early time of Raman spectroscopy. According

to him and thanks to his personal photos and documents collections and supplemented by his coworkers, R. Claus, Derek A. Long and H. W. Schrotter, Kiefer highlighted the very first report in a conference in 1961 of the Raman spectrum of benzene excited with a ruby laser and recorded on a photographic plate. He also explained how the first meeting dedicated solely to Raman spectroscopy was born and held in Ottawa, 1969, in answer to the scientific community needs to discuss and share their first results on Raman spectroscopy. The 23-rd ICORS meeting returned to Bangalore after more than three decades (since 1978) to celebrate Raman through the homecoming conference, The meeting was held at the Indian Institute of Science, Bangalore, the original home of Sir C. V. Raman where many of Raman's spectroscopic studies were carried out. It was the place where C. V. Raman first headed as an Indian director.

Kiefer also has chaired the 1992 edition of the ICORS in Wurzburg [6]. The latest ICORS edition (2014) was chaired by the former W. Kiefer's disciples, Professor Jürgen Popp and Volker Deckert (Jena, Germany) where the exciting moment of Raman Lifetime Award ceremony proclaimed W. Kiefer as winner. This meeting outlined an absolute record in bringing together more than 900 Raman spectroscopy scientists worldwide indicating the continuously increasing interest of the scientific community for Raman techniques and applications [7].

From these facts it is obvious that the early historical international context was timely fitted with the first interest in Raman spectroscopy in Cluj.

### **Early Raman studies**

The first applications of the new type of molecular analysis were first focused on recording and assigning the Raman spectra of some interesting molecules. British Chemical and Physiological Abstracts released in February 1940 [8] [[http://delibra.bg.polsl.pl/Content/5980/P-323\\_1940\\_I\\_February\\_AO.pdf](http://delibra.bg.polsl.pl/Content/5980/P-323_1940_I_February_AO.pdf)] summarized a number of 24 abstracts dealing with Raman spectroscopy

applied to analyze Raman spectra of gaseous and liquid samples like  $\text{SiH}_4$ ,  $\text{NH}_3$ ,  $\text{C}_2\text{H}_2$ , nitrates, uranyl salts, tetra- and hexa-coordinated complexes. chlorides, cyanides, and nitrites; fluorenes, aluminium and arsenic trimethyls; other notes on the occurrence of the overtones in Raman effect, the observation of the rotational Raman lines near the Rayleigh line, and mention on the Raman-Krishnan theory on the refractivity of liquids. We reproduce here an early explanation: *“In general the principal  $\nu$  for the liquid is slightly < that for the vapour, and the difference is related to the no. of electrons in the mol.”* [8] [[http://delibra.bg.polsl.pl/Content/5980/P-323\\_1940\\_I\\_February\\_AO.pdf](http://delibra.bg.polsl.pl/Content/5980/P-323_1940_I_February_AO.pdf)].

In the early '60-ths, molecules like the iodine, n-alkans (ethane, propane, n-butane, n-pentane, n-hexane), cyclohexane, benzene, carbon tetrachloride, carbon disulfide, chloroform, acetonitrile, methanol, methyl bromide, methyl chloride, acetylene, and vinyl acetylene [8-11], sulfur hexafluoride [12-14] were of high interest because of their symmetry, overtones observed in some cases and interesting behavior in Raman spectroscopy on passing from the solid or liquid to the vapor phase. The overtone progression in the resonance Raman effect of iodine vapor showed a remarkably fine structure which later became one of the most studied molecule for didactic purpose in the students labs program worldwide, including at the Babes-Bolyai University. The observed resonance Raman lines [15] could be explained in terms of Q branches, S band heads and vibrational “hot” band structure. Comparing the observed Raman spectra with calculated Q, S and O branches, using spectroscopic constants derived from the high resolution fluorescence measurements of Rank and Rao, Kiefer and Bernstein [15] have been able to assign all observed Raman lines. The spectroscopic constants  $\omega_e$  and  $\omega_e x_e$  for the ground state of iodine have been determined, whereas the constants  $\omega_e y_e$  and  $\alpha_e$  could only be estimated.

### **First Romanian results**

In his doctoral theses, H. Tintea systematically investigated the benzene and toluene derivatives and compared the spectra with those of the already existent main compounds from literature. He prepared himself

in the lab orto-, meta- and para-fluoro benzene and toluene respectively and continued with chloro- and brom derivatives. It must be pointed out a remarkable sample preparation and impressive knowledge in chemical synthesis. For the gaseous phases he built in the lab the necessary devices to fill the small glass bulbs with the gases and to measure their spectra. The spectra were recorded on spectral plates with the finest grain emulsion using a Hilger spectrograph (Fig. 3) with a constant deviation quartz prism of 6 cm base length. On the same plates he recorded the atomic emission spectra of iron for reference purpose to finally calculate the positions of the observed bands by linear interpolation with the help of the famous Kayser's Tables. The *kayser* unit, was associated with  $1 \text{ cm}^{-1}$  (wavenumber) after the name of German spectroscopist Heinrich Kayser (1853-1940) whose studies on the atomic spectra highlighted the need for a proper unit easy-to-use in the optical spectroscopy within the CGS system. Țintea was disappointed not being able to observe the rotational structure of the vibrational bands.

Years later, Hariton Țintea became professor of Optics at the Faculty of Physics and among his students, T. Iliescu took up since 1970 and continued Raman spectroscopy studies. However, doctoral thesis presented by T. Iliescu in 1976 dealt with absorption and luminescence and not with Raman spectra. The context was under the full communism regime with restriction for publication internationally. The first internationally published paper was authored by Iliescu (1984): "Absorption, fluorescence and phosphorescence spectra of F, Cl, Br-Naphtalenes in crystalline matrixes at 77K" [16]. The article highlights in the experimental section: "*A Hilger E 31, f/3.5 spectrograph was employed to obtain the absorption and fluorescence spectra, while the phosphorescence spectra were obtained with a spectrograph Zeiss with 3 prisms. The 2537 and 3021 Å lines from a 1000 W mercury lamp were used to excite the spectra.*" However, the students of the late '70-ths already had the possibility to study Raman effect in a practical lab work as revealed by the old, unpublished lab documents. The lab procedure required recording the Raman spectrum on a photographic plate and to read the observed bands position with the help of an Abbe comparator for wavelength determinations (Fig. 3).

The calculations were usually followed by wavenumber conversion and further differences calculation to the excitation line provided by the mercury lamp with adequate filter. As such obtained wavenumbers differences finally revealed the Raman active modes experimentally recorded. Because of the extremely weak scattering intensity and the limited detection possibilities, a sample exposure usually required 6 to 9 hours for obtaining a good quality Raman spectrum on a photographic plate.

### **Four generations of Raman spectroscopy equipment**

The time to upgrade for a double monochromator GDM 1000 came in the late 70-ths where high quality Raman spectra excited with He-Ne or Ar ion lasers could be obtained Fig. 3(b). The GDM-1000 double grating monochromator Carl-Zeiss Jena model, with focal length 2x1 m, with good detection capability provided by a photomultiplier with range of 0,5-500 with adjustable voltage (600-1400 V), integration time 0,1-30 s, and an XY-stage with paper recorder, opened new exciting experimental opportunities. As such, Iliescu's group started to investigate molecular dynamics and among the topics it should be mentioned vibrational relaxation of dimethylsulfoxide in solutions (1985-1990) [17, 18].

Additional research topic on the structural investigation of the various oxide glass systems [19-21] using Raman spectroscopy has been flourished.

Meanwhile, the surface enhanced Raman scattering (SERS) effect, discovered in 1974 [22] stimulated the Romanian researchers at Babes-Bolyai University to explore the Raman enhancement capability of an electrochemically roughened Ag electrode as well as the colloidal Ag nanoparticles prepared by the Creighton method [23]. Acridine derivatives were largely studied. The first paper on SERS published in a national journal (*Studia Universitatis Babes-Bolyai, seria Physica*, 1995) reported Raman and SERS spectra of acridone recorded with the GDM 1000 double grating monochromator [24] and followed by the characterization of triazine derivatives [25-28].

In the First Day of Orthodox Easter of the year 1995, Professor W. Kiefer landed for the first time in Cluj-Napoca aiming to visit the “Raman spectroscopy lab” from Babes-Bolyai University and to meet researchers and students. In reward for his hospitality as chair of the ICORS in Wurzburg (1992), Kiefer was invited by Iliescu to visit Romania, Cluj and the university. Kiefer was not aware on the different date of the Orthodox Easter to the Catholic one. Except the three people waiting for the guest, T. Iliescu, S. Astilean and S. Cinta, the university was empty. It was however, a perfect context for fruitful and festive discussion on the technical problems encountered during Raman measurement on GDM-1000. After rolling out tens of meters of Raman spectra recorded on paper, the discussion got to the end with an invitation for the author of this paper- at that time PhD student- to measure and perform experiments with his equipment in his headed laboratories in Würzburg. Several months later, the invitation was honored after successfully application for a Soros scholarship. The moment marked the beginning of a fruitful and long cooperation reaching 20 years in 2015.

Practically since 1997 the number of published papers reporting Raman spectroscopy investigations on various pharmaceutical, biological, chemical syntheses compounds, oxide materials and many others, increased substantially and an increased number of students started to conduct PhD in the Raman spectroscopy field. The first thesis in the SERS topic was presented in 1998 by the author [29].

Inspired by the Raman spectroscopy equipment and applications possibility from *Institut Für Physikalische-Chemie* of the University of Würzburg, the Romanian researchers succeeded to acquire “the third generation” Raman spectrometer namely a Fourier Transform Raman (FT-Raman) equipment in 2000 followed by the first Raman microscope acquired in Romania (RAMANSCOPE II), fiber optic coupled with the FRA106S Raman module of the FT-IR Equinox 55 (Bruker) spectrometer in 2002 [30]. A workshop in cooperation with the Bruker Optics was organized to bring together the scientists and potentially interested people from various research

fields [31]. This upgrade was possible because as young researcher, the author was awarded with a research grant financed by the World Bank and Romanian Government.

A Witec confocal Raman microscope (CRM) was acquired in 2008 in the Professor Astileanu's group [32] and additionally, two miniaturized, compact, DeltaNU Raman instruments with integrated lasers operating at 523 nm and 632.8 nm respectively, were acquired in 2010 through the jointly financed efforts through the research grants.

The youngest Raman equipment acquired in 2012 at Babes-Bolyai University was a Renishaw InVia Reflex confocal Raman spectrometer coupled with the NT-MDT Ntegra Spectra SPM microscope [33]. The acquisition was possible through an infrastructure project coordinated in the Physics counterpart of the university by the dean of Physics Faculty, Professor O. Cozar and after his retirement taken by Professor Vasile Chis, the current department director. Raman/AFM combines high resolution AFM imaging capabilities with the structural characterization of the sample. Micro-Raman spectroscopy is conducted with a research-grade optical microscope (Leica) coupled to a high-performance Raman spectrometer that provides a powerful non-invasive Raman analysis of delicate samples. The instrument provides both highly specific and sensitive analysis and imaging for a wide range of material types. It is perfectly suited for rapid, non-destructive analysis in life science, materials science, (bio)physics, chemistry, nanotechnology, biophotonics and plasmonics. Raman microscopy enables physico-chemical molecular analysis with spatial resolution of less than 1  $\mu\text{m}$  (lateral) and less than 2  $\mu\text{m}$  (depth). Raman shifts within 100  $\text{cm}^{-1}$  of the excitation frequency can be measured at excitation wavelengths of 325, 442, 532, 632.8, 785 and 830 nm with a spectral resolution 0.5  $\text{cm}^{-1}$  in visible and 1  $\text{cm}^{-1}$  in UV and NIR. Raman imaging on small surfaces is possible using an automated scan stage that has reduced total mapping times to a compatibility level for *in vivo* diagnostic and monitoring on biosamples.

RAMAN SPECTROSCOPY AT BABES-BOLYAI UNIVERSITY- HISTORICAL RETROSPECTIVE



**Fig. 3.** Four generations of Raman spectroscopy equipment at Babes-Bolyai University: a) Hilger spectrograph (left) with the constant deviation quartz prism; Abbe comparator (right) allowing to read the wavelength by comparison with the positions of the iron reference spectral atlas; They were used in the period from 1933 to early '70-ths; b) Double grating GDM 1000 monochromator with photomultiplier as detection system and XY stage for spectra recording on paper rolls (used between 1970-1998); c) FT-IR, FT-Raman & micro-Raman Bruker equipment (since 2002, still running); d) Confocal Renishaw InVia Reflex Raman microscope coupled with the NT-MDT Ntegra Spectra SPM microscope; 5 lasers with 6 available lines, 325,442, 532, 633, 785 and 830 nm respectively, spectral resolution  $0.5\text{ cm}^{-1}$  in visible and  $1\text{ cm}^{-1}$  in UV and NIR (since 2013).



**Fig. 4.** Founders of the Raman Spectroscopy School at Babes-Bolyai University  
Professors Traian Iliescu (left) and Wolfgang Kiefer (right).

Picture taken on November 2012 in Aula Magna Hall of Babes-Bolyai University,  
on the occasion of Dr. H. Causa Ceremony of Professor Jürgen Popp, from Jena.

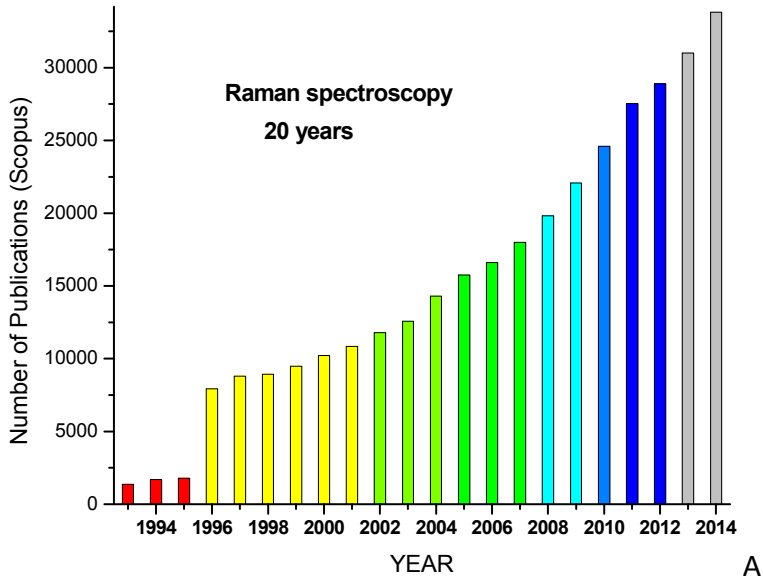
The four currently active Raman spectroscopy laboratories comprised in the Biomolecular Physics Department at Babes-Bolyai University (<http://phys.ubbcluj.ro/departamente/btism.htm>) allow a wide range of technical Raman applications, from conventional vibrational spectroscopy structural investigations, to Raman imaging, polarized Raman, resonance Raman, NIR-Raman, UV-Raman, SER(R)S, NIR-SERS, low-wavenumbers Raman, photoluminescence, simultaneous Raman/AFM while nanomaterial manipulation, for various interdisciplinary research topics [34-39].

The year 2008 pointed out the first expanded application from molecules characterization to tissue complex biosamples [34], through the study on the possibility to incubate tissue with nanoparticles and recording SERS spectra. The findings were published as *Rapid Communication* in *Journal of Raman Spectroscopy* and practically opened a new field in the applied Raman spectroscopy, toward Raman diagnostic and therapy monitoring. Further applications in food control, pharmaceuticals, drug delivery in cells or tissue, environmental monitoring, aquaculture sector, as well as on new, smart or advanced (nano)materials are in due course.

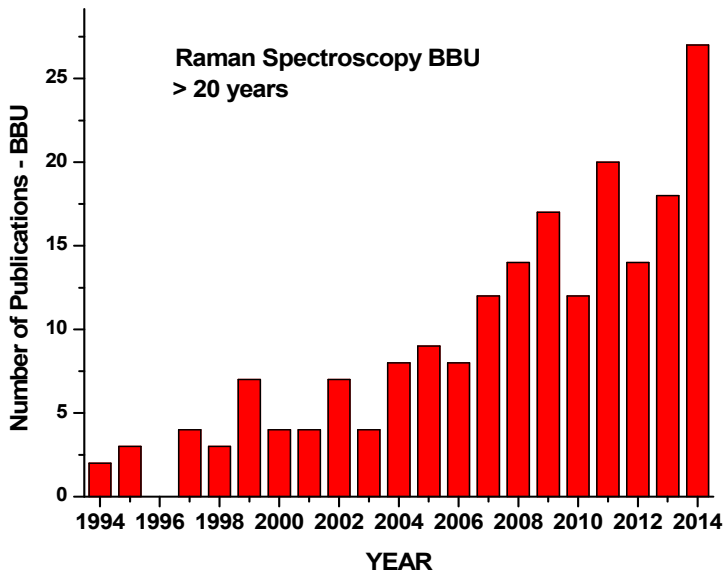
Taking a retrospective look, a real Raman Spectroscopy School was built in the university and the founders of this enterprise (Fig. 4) are highly acknowledged.

### **Scientometry on Raman spectroscopy**

In order to highlight quantitatively the growth and development on Raman spectroscopy at Babes-Bolyai University the scientific production in the topic in terms of publication output as per Science Citation Index (1982–2005) is shown in the Fig. 5 in comparison with the worldwide output. During 1994–2014 a total of 215 papers (PubMed found only 27) were published by the Romanian scientists in the field ‘Raman spectroscopy, meaning an average of more than 10 papers per year. Comparing with the worldwide publications trend in the same time span, the tendency is not keeping the exponential grow as in the case of Fig. 5 a), which can be related to other, non-scientific factors, like number of people involved, financial support, etc. The growth trend is however, clearly defined.



A



B

**Fig. 5.** Graphical display of the number of publications in the topic of Raman spectroscopy in the 20 years period from 1994 to 2014: Top: worldwide, bottom: affiliated to Babes-Bolyai University. Data available from Science Citation Index and Science Direct (accessed on January 15, 2015).

## REFERENCES

- [1]. C. V. Raman: A new radiation, *Indian J. Phys.* 2 (1928) 387.
- [2]. C.V. Raman and K. S. Krishnan: *Nature*, 121 (1928) 501.  
<http://www.uky.edu/~holler/raman.html>
- [3]. S. Bhagavantam, "Chandrasekhara Venkata Raman 1888-1970". *Biographical Memoirs of Fellows of the Royal Society* 17: 564–526 (1971).  
doi:10.1098/rsbm.1971.0022.
- [4]. A. Materny, J. Popp, M. Schmitt, H. W. Schrotter and A. M. Zheltikov, Wolfgang Kiefer, An Appreciation, *J. Raman Spectrosc.*, 37: 1–19, (2006).
- [5]. Jürgen Popp, Michael Schmitt, Arnulf Materny, Preface – The Many Facets of Raman Spectroscopy *Zeitschrift für Physikalische Chemie International journal of research in physical chemistry and chemical physics.* 225, 6-7, 643–646, (2011).
- [6]. Proc. XXIV ICORS, 10-15 August 2014, Jena, Germany, Eds. J. Popp, V. Deckert, 2014.
- [7]. Proc. Thirteenth International Conference on Raman Spectroscopy, 31 August - 4 Sept. 1992, Eds. W. Kiefer, M. Cardona, G. Schaack, F.W. Schneider, H.W. Schrötter, John Wiley&Sons, Chichester, England, 01/1992.
- [8]. H.W. Schrötter, H.J. Bernstein, Absolute Raman Intensities, *J. Mol. Spectrosc.*, 7, 1–6, 1961, 464-465.
- [9]. Z. Kecki, H.J. Bernstein, Intensity in the Raman effect: Part X. Some absolute intensities in methanol vapor, *J. Mol. Spectros.* 15, 3, 1965, 378-385.
- [10]. W. Kiefer, Registrierung von Ramanspektren mit einem quasikontinuierlichen Rubinlaser, *Ber. Bunsenges. Physikal. Chemie* 72, 1062 (1968).
- [11]. W. Kiefer und H.W. Schrötter, Verbesserung des Signal-Rausch-Verhältnisses bei der Registrierung von Ramanspektren mit 50-Hz-Rubinlaser-Erregung, *Z. Angew. Physik* 25, 236 (1968).
- [12]. H.F. Shurvell, H.J. Bernstein, The Raman spectrum of solid sulfur hexafluoride, *J. Mol. Spectrosc.*, 30, 1–3, 1969, 153-157.
- [13]. H.W. Schrötter and H.J. Bernstein: *J. Mol. Spectrosc.* 7 (1961) 464.
- [14]. H.F. Shurvell, H.J. Bernstein, The Raman spectrum of solid sulfur hexafluoride, *J. Mol. Spectrosc.* 30, 1–3, 1969, 153-157.

- [15]. W. Kiefer, H.J. Bernstein, Vibrational-rotational structure in the resonance Raman effect of iodine vapor, *J. Mol Spectros.*, 1972; 43(3), 366-381. DOI: 10.1016/0022-2852(72)90048-3.
- [16]. T. Iliescu, I Milea and P.M. Abdolrahman, *J. Mol. Str.*, 115 (1984), 209-212.
- [17]. I. Bratu, T. Iliescu, I. Milea, Molecular reorientational motion in liquid deuterated dimethyl-sulfoxide (DMSO-d<sub>6</sub>) from Raman line widths, *Journal of Molecular Liquids*, 30, 4, (1985), 231-236.
- [18]. T. Iliescu, S. Astilean, I. Bratu, Raman study of vibrational relaxation of dimethylsulfoxide in solutions, *J. Mol. Liquids*, 47, (1990), 129-137.
- [19]. T. Iliescu, S. Simon, D. Călugăr, Raman spectroscopy of oxide glass system (1-x) (yB<sub>2</sub>O<sub>3</sub>.zLi<sub>2</sub>O) .xMO (MO = CuO, V<sub>2</sub>O<sub>5</sub>) *J. Mol. Struct.*, 267, 1992, 231-233.
- [20]. T. Iliescu, S. Simon, D. Maniu, I. Ardelean, Raman spectroscopy of oxide glass system (1-x) [yB<sub>2</sub>O<sub>3</sub>.zLi<sub>2</sub>O].xGd<sub>2</sub>O<sub>3</sub> *J. Mol. Struct.*, 294, 1993, 201-203.
- [21]. T. Iliescu, I. Ardelean, S. Simon, Raman study of B<sub>2</sub>O<sub>3</sub>-PbO-Gd<sub>2</sub>O<sub>3</sub> glasses *Solid State Comm.*, 90, 8, 1994, 507-509.
- [22]. M. Fleischmann, P.J. Hendra and AJ McQuillan, Raman Spectra of Pyridine Adsorbed at a Silver Electrode, *Chem. I Phys. Lett.* 26 (2): 163–166. doi:10.1016/0009-2614(74)85388-1
- [23]. T. Iliescu, M. Vlassa, M. Caragiu, I. Marian, S. Astilean, Raman study of 9-methylacridine adsorbed on silver sol, *Vib. Spectrosc.* 8, (3), 1995, 451–456.
- [24]. I. Marian, T. Iliescu, M. Caragiu, S. Ghizdavu, S. Cîntă, Aspects in Spectroelectrochemical Raman Analysis, *Studia Univ. Babes-Bolyai Seria Chemia*, 1, 14 (1994).
- [25]. S. Cîntă, T. Iliescu and S. Crăciun, Surface-enhanced Raman Scattering of 9, (10H) Acridone on silver sols *Studia Univ. Babes-Bolyai Seria Physica*, nr. 1, 25 (1995).
- [26]. T. Iliescu, S. Cîntă, S. Astilean, I. Bratu, The pH influence on the PP vitamin Raman spectra, *Studia Univ. Babes-Bolyai, Seria Physica*, Nr. 2, p. 39-47 (1995).
- [27]. S. Cîntă, T. Iliescu, M. Vlassa, M. Venter, I. Beldean, Raman, IR and SERS studies of 2,4-diamino-6-phenyl-1,3,5- triazine *Studia Univ. Babes-Bolyai, Seria Physica*, Nr. 1, p.3-10 (1995).

- [28]. I. Marian, S. Cîntă, E. Veress, M. Venter, Surface Enhanced Raman Scattering of KSCN on the Covered Redox Glass Electrodes, *Studia Univ. Babeș-Bolyai, Seria Physica*, 41, 54, 1996.
- [29]. S. Cîntă, Raman and SERS studies on the metal-adsorbate complex for biologically interest molecules, Doctoral Thesis, BCU, Cluj-Napoca, 1998.
- [30]. [http://www.phys.ubbcluj.ro/~cozar/omnia/cozar\\_pres.pdf](http://www.phys.ubbcluj.ro/~cozar/omnia/cozar_pres.pdf)
- [31]. S. Cîntă Pinzaru, FT-IR, FT-Raman & Micro-Raman spectroscopy and Applications, Bruker workshop, Cluj-Napoca, Romania, 2002.
- [32]. S. Cîntă Pinzaru, Surface-enhanced Raman Scattering (SERS): cutting edge in sensing technologies and applications, in Workshop „Introduction to Confocal Raman and Scanning Probe Microscopy”, Cluj-Napoca, Romania, 2008; <http://www.witec-instruments.de/en/eventsseminars/files/FlyerCluj08.pdf>
- [33]. <http://www.phys.ubbcluj.ro/raman/>
- [34]. S. Cîntă Pinzaru, Book Review: Raman and SERS Investigations of Pharmaceuticals, Authors: M. Baia, S. Astilean, T. Iliescu ([www.interscience.wiley.com](http://www.interscience.wiley.com)), *J. Raman Spectrosc.*, 40, 6 (2009) 709.
- [35]. D. Moigno, I. Pavel, S. Cîntă and W. Kiefer, Recent Research Developments in Organometallic Chemistry”, Vol. 4 (2001) Ed. S.G. Pandalay, (ISBN:81-7736-064-7), Research Signpost, Trivandrum, India: Cap.: “Vibrational Spectroscopy and Theoretical Studies on organometallic complexes”, P.11-39.
- [36]. T. Iliescu, S. Cîntă Pînzaru, D. Maniu, R. Grecu, S. Aștilean, “Aplicații ale spectroscopiei vibraționale”, Ed. Casa Cărții de Știință, Cluj-Napoca (ISBN 973-686-292-5), 2002.
- [37]. T. Iliescu, Simona Pinzaru, Spectroscopia Raman și SERS cu aplicații în biologie și medicină, First edited by M. Trifu,; Casa Cărții de Știință, ISBN: 978-973-133-887-3, 2011.
- [38]. S. Cîntă Pînzaru, I.E. Pavel, Surface Enhanced Raman Spectroscopy- Analytical, Biophysical and Life Science Applications, Chapter 6, SERS and Pharmaceuticals, Editor S. Schluecker, WILEY-VCH Verlag, p.129-154, 2010.
- [39]. <http://www.unidu.hr/datoteke/4476/RIKAGU-workshop-Dubrovnik.pdf>
- [40]. S. Cîntă Pînzaru, L.M. Andronie, I. Domsa, O. Cozar and S. Astilean, (2008), Bridging biomolecules with nanoparticles: surface-enhanced Raman scattering from colon carcinoma and normal tissue. *J. Raman Spectrosc.*, 39: 331–334. doi: 10.1002/jrs.1907



## RAMAN SPECTROSCOPY OF $\text{Pb}(\text{V}_{1-x}\text{M}_x)\text{O}_3$ PEROVSKITE COMPOUNDS

AL. OKOS<sup>a,b</sup>, P. BORDET<sup>a</sup>, N. LEOPOLD<sup>b</sup>,  
C. LUNG<sup>b</sup> and A. POP<sup>b,\*</sup>

**ABSTRACT.** The perovskite oxide  $\text{Pb}(\text{V}_{1-x}\text{M}_x)\text{O}_3$  (M=Ti,Fe and  $x=0.00;0.25$ ) was synthesised by solid state reaction under high pressure – high temperature conditions. Using Raman scattering spectroscopy, single phase formation of PVO ( $x=0.00$ ) with the shift of phonon modes was confirmed. Raman spectroscopy was used as a local probe sensitive to even subtle changes of symmetry after the partial substitution of V with  $x=0.25$  Ti and Fe.

**Keywords:** *PbVO<sub>3</sub>, high pressure - high temperature synthesis, Raman spectroscopy.*

### INTRODUCTION

Of central importance for understanding the fundamental properties of ferroelectrics is dynamics of crystal lattice. Perovskite and perovskite derived phases,  $\text{ABO}_3$ , provide the main inorganic ferroelectric materials used in applications. These are based on a cubic lattice with A ions on the cube corners and B ions at the cube centers, inside corner sharing octahedral

---

<sup>a</sup> Néel Institute, CNRS/UJF, UPR2940, 25 rue des Martyrs, BP 166 38042, Grenoble Cedex 9

<sup>b</sup> Babes-Bolyai University, Faculty of Physics, Str. Kogălniceanu, Nr. 1, RO-400084 Cluj-Napoca, Romania

\* Corresponding author: aurel.pop@phys.ubbcluj.ro

O cages. One strategy for synthesizing multiferroics is to substitute one of the perovskite sites with magnetic ions in materials where the ferroelectricity is driven by the other site, as for example in BiFeO<sub>3</sub>.

Thus, perovskite vanadates offer the possibility of combining a magnetic B-site ion with insulating behavior and stereochemical activity on both the A and B-sites. This was recently realized by the high pressure synthesis of PbVO<sub>3</sub> (PVO).

PVO is insulating and occurs in the tetragonal, non-centrosymmetric structure, like PbTiO<sub>3</sub>, but with a very large tetragonality,  $c/a = 1.23$ . The structural distortion may be described as off centering of Pb and V accompanied by a distortion of the VO<sub>6</sub> octahedral cage.

X-ray diffraction (XRD) [4], and Raman spectroscopy [5-12] have been used for stress analysis of ferroelectric materials. Raman spectroscopy is complementary to XRD methods as it is a local probe and is sensitive to even subtle changes of symmetry. Moreover, ferroelectricity and thus Raman modes are strongly influenced by mechanical deformation of the sample resulting, for example, from hydrostatic pressure or stress [6, 7,13-16]. Both PbVO<sub>3</sub> and PbTiO<sub>3</sub> adopt a tetragonal symmetry (space group P4mm or C<sup>1</sup><sub>4v</sub>) with one formula per unit cell [31]. Both undergo a tetragonal to cubic phase transition. The transition of PbTiO<sub>3</sub> occurs at 490° C but the (T-C) transition of PbVO<sub>3</sub> only takes place under high pressure conditions where investigations are harder to perform.

Therefore the discussion's starting point will be the cubic structure of PbTiO<sub>3</sub>. There are 12 vibration modes for the cubic phase which belong to the irreducible representation  $3T_{1u} + T_{2u}$ . The  $T_{1u}$  modes are only infrared (IR) active and the  $T_{2u}$  is a silent mode neither Raman nor IR active therefore no Raman signal should be obtained for the cubic phase. On the tetragonal phase, each  $T_{1u}$  mode splits and produces an  $A_1$  and an E mode (for a total of  $3A_1 + 3E$  modes) and the  $T_{2u}$  mode splits into  $B_1 + E$  modes. The  $A_1$  and E modes are infrared and Raman active and the corresponding phonons are polarized in the z-direction or in the x-y plane, respectively. The B1 mode is only Raman active [17].

The Raman tensors are presented below, for each mode, and the direction of polarization is indicated in parentheses.

$$A_1(z) = \begin{bmatrix} a & \cdot & \cdot \\ \cdot & a & \cdot \\ \cdot & \cdot & b \end{bmatrix} \quad B_1 = \begin{bmatrix} c & \cdot & \cdot \\ \cdot & -c & \cdot \\ \cdot & \cdot & \cdot \end{bmatrix} \quad E(x) = \begin{bmatrix} \cdot & \cdot & -e \\ \cdot & \cdot & \cdot \\ -e & \cdot & \cdot \end{bmatrix} \quad E(y) = \begin{bmatrix} \cdot & \cdot & \cdot \\ \cdot & \cdot & e \\ \cdot & e & \cdot \end{bmatrix}$$

Due to long-range electrostatic forces, all  $A_1$  and  $E$  modes split into transverse (TO) and longitudinal (LO) components. Depending on the phonon propagation direction ( $x$ ,  $y$  or  $z$ ), only pure TO or LO can be observed in Raman spectra, as presented in table 1.

**Table 1.** Assignment of TO and LO modes according to the phonon propagation direction.

Propagation direction	Phonon assignment		
	E(x)	E(y)	$A_1(z)$
x	LO	TO	TO
y	TO	LO	TO
z	TO	TO	LO

In this note the synthesis and Raman spectroscopy of the  $\text{PbV}_{1-x}\text{M}_x\text{O}_3$  ( $M=\text{Ti,Fe}$  and  $x=0.00,0.25$ ) perovskites will be presented. The Raman spectra are also analysed in correlation with the nature of substitution in vanadium position.

## EXPERIMENTAL

$\text{PbV}_{1-x}\text{M}_x\text{O}_3$  ( $x=0.00,0.25$  and  $M=\text{Ti,Fe}$ ) polycrystalline samples were prepared by solid state reaction under high pressure, high temperature conditions (HP-HT) in a CONAC type apparatus. Almost single phase samples were obtained at pressures of 6 GPa and temperatures of 950° C [18-20]

The chemical composition of the samples was confirmed by EDX measurements. As an example, for  $x=0.25\text{Ti}$  sample the composition is  $\text{Pb}_{0.99}\text{V}_{0.73}\text{Ti}_{0.27}\text{O}_3$  which is close to the nominal composition of  $\text{PbV}_{0.75}\text{Ti}_{0.25}\text{O}_3$ .

The Raman spectra were recorded using a Renishaw inVia Raman Microscope. The HeNe laser emitting at 633 nm with a power of 50 mW was used. The spectral resolution of the recorded spectra was  $\sim 4\text{ cm}^{-1}$ . For all normal Raman measurements a 40x objective and the 10% neutral density filter was used. The registered spectra are the average of 9 accumulations with 10 s integration time. Raman spectra were collected for the same 4 representative samples,  $\text{PbVO}_3$  ( $x=0.00$ ),  $\text{PVT}_{25}$  ( $x=0.25$ ,  $M=\text{Ti}$ ),  $\text{PVF}_{25}$  ( $x=0.25$ ,  $M=\text{Fe}$ ) at RT using a laser radiation with a wavelength of 633 nm. The peaks of Raman spectra were attributed to vibration modes by comparing the spectra obtained by us to spectra reported in literature for  $\text{PbTiO}_3$  [21, 22-25].  $\text{PbVO}_3$  and  $\text{PbTiO}_3$  are isostructural and the Raman spectra they present are similar so  $\text{PbTiO}_3$  is a good model for the interpretation of the Raman spectra of  $\text{PbVO}_3$ .

## RESULTS AND DISCUSSION

Figure 1 shows the Raman spectra obtained by measurements in different regions of the same sample  $\text{PbVO}_3$ . The striking feature for these spectra (and for spectra of the other 3 samples) is the change of some peaks intensities and the shift of peak positions depending on the regions from which data was collected. A reasonable explanation of this behaviour is the presence of local inhomogeneities and of the strain. Nevertheless the spectra are similar and the identification of (most of) the vibration modes is possible. More probable, responsible for the presence of supplementary peaks in the samples is the presence of small quantities of impurities which are easily detected by the Raman spectroscopy.

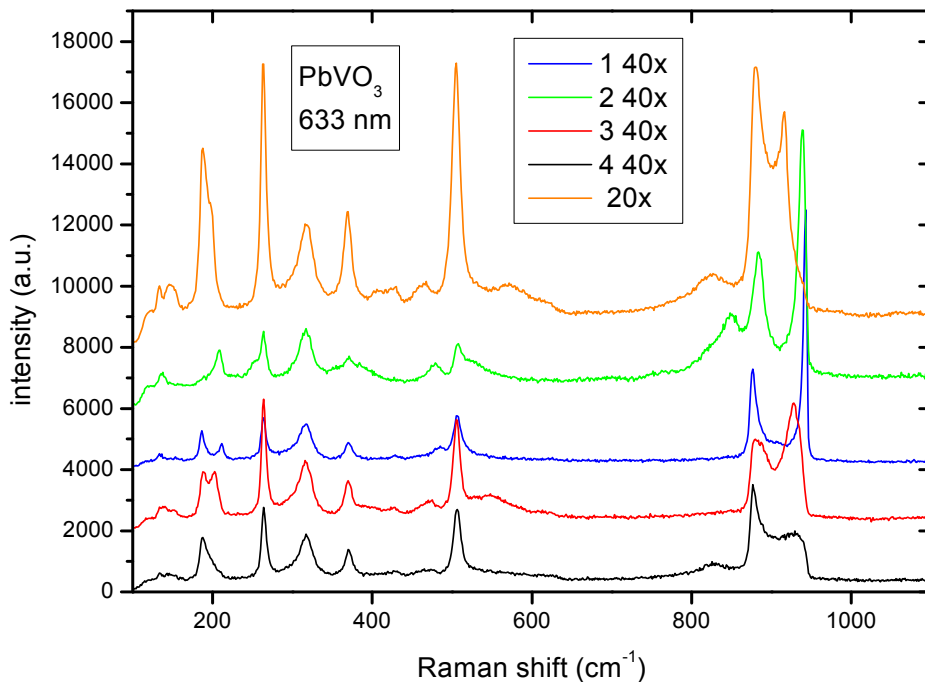


**Fig. 1.** Raman spectra for  $\text{PbVO}_3$ . The data was collected using a laser wavelength of 633 nm. Two objectives were used of 40X respectively 20X. The laser power was set a 5% and the integration time was 10 seconds. 9 integrations were made.

A representative Raman spectrum of PVO was selected in figure 2. The Raman peaks were attributed to vibration modes according to the rules discussed above and data available in literature. There are 3 regions on the spectra associated with the following vibrations of the cations of the  $\text{PbVO}_3$  unit cell:

- Region I including peaks at low wavenumbers, up to  $220 \text{ cm}^{-1}$  associated with the vibrations of the Pb-O bonds. These peaks appear at approximately  $147$   $188$  and  $200 \text{ cm}^{-1}$
- Region II, with peaks between  $220$  and  $550 \text{ cm}^{-1}$  attributed to the V-O2-V bending motion. These peaks appear at  $318$ ,  $370$  and  $506 \text{ cm}^{-1}$

- Region III made of peaks at high wavenumbers (in the range 830 to 930  $\text{cm}^{-1}$ ) attributed to the V-O1 stretching with peaks appearing at 880 and 917  $\text{cm}^{-1}$

The spectrum is dominated by the peaks attributed of the V-O1 vibration of the strong short vanadyl bond. The small peaks marked with star are not identified.

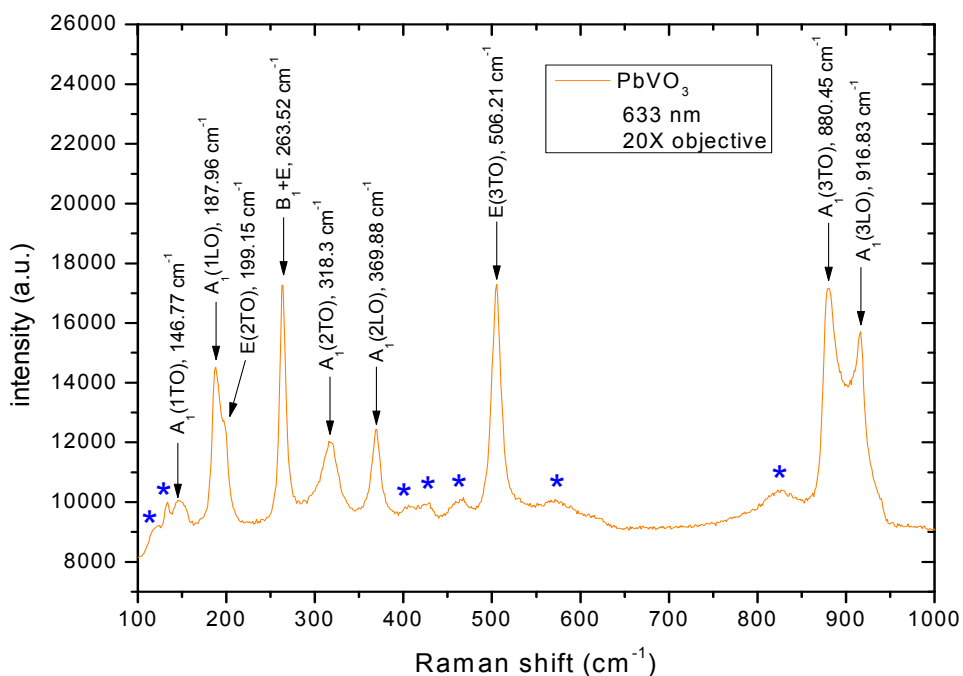


**Fig. 2.** Vibration modes for  $\text{PbVO}_3$ . The peaks marked with star are not identified. The data was collected using the 20X objective. The laser power was set a 5% and the integration time was 10 seconds. 9 integrations were made.

Figure 3 shows the vibration modes assignment for data collected for the PVT\_25 sample. The spectra for PVT\_25 and  $\text{PbVO}_3$  are similarly, however the spectra for the PVF\_25 sample are characterized by broad overlapping peaks.

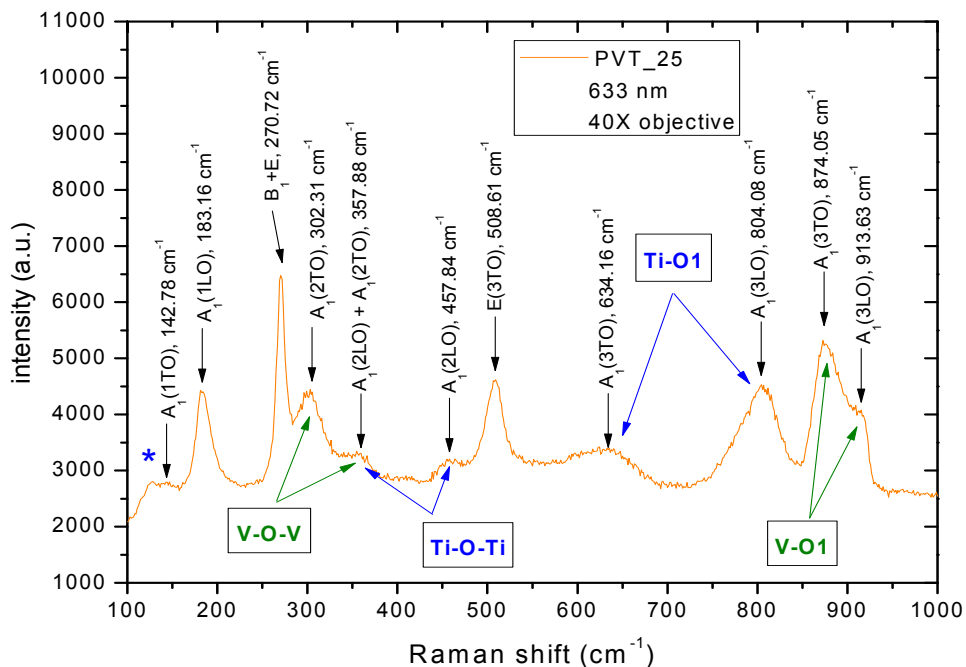


**Fig. 3.** Raman vibration modes for PVT\_25. The peaks marked with star are not identified. The data was collected using the 40X objective. Laser power was set at 5% and the integration time was 10s. 9 integrations were made.

The peaks from the spectrum of PVT\_25 can be related to the peaks of the parent compound,  $\text{PbVO}_3$  and can be organized on the same 3 regions.

- Region I, from 100 to 230  $\text{cm}^{-1}$ , where peak positions appear at 143 and 183  $\text{cm}^{-1}$ .
- Region II between 230 and 520  $\text{cm}^{-1}$ , where peak positions appear approximately at 270, 358, 458 and 508  $\text{cm}^{-1}$ .
- Region III above 520  $\text{cm}^{-1}$ , where peak positions appear approximately at 634, 804, 874 and 914  $\text{cm}^{-1}$ .

By comparing the Raman spectra for  $\text{PbTiO}_3$  [24] and for  $\text{PbVO}_3$  it appears that the  $A_1(3\text{TO})$  and  $A_1(3\text{LO})$  can be attributed separately to the Ti-O1 and to the V-O1 stretching vibrations. It might be inferred that the V-O1 bond is shorter and stronger than the Ti-O1 bond (where O1 denotes the apical oxygen) since it appears at higher wavenumbers. It can also be supposed that the sample contains local structural fluctuations caused by the fact that  $\text{Ti}^{4+}$  forms a weaker bond to the apical oxygen and hence a different coordination. This result is consistent with observations based on diffraction experiments.

It seems that the peaks from region II can also be separated according to the atom bonds that correspond to them. The peak observed at about  $358\text{ cm}^{-1}$  appears to contain the contributions from the  $A_1(2\text{TO})$  mode for the Ti-O-Ti bending oscillation and the  $A_1(2\text{LO})$  mode for the V-O-V bending oscillation.

Figure 4 shows the vibration mode assignment for data collected for the PVF\_25 sample. When Fe substituted V in  $\text{PbVO}_3$ , the effect of the substitution is dramatically different from the effect of the Ti substitution. The spectra for the PVF\_25 sample are different from the spectra of the Ti counterpart and the spectra of  $\text{PbVO}_3$  as they present essentially only two very broad peaks. For PVF\_25 it appears that there is a convolution of the  $A_1(3\text{TO})$  and  $A_1(3\text{LO})$  which generates a single broad peak centered at about  $842\text{ cm}^{-1}$ . This peak is associated to the B site cation – apical oxygen stretching oscillation. Similarly, the peak that appears at about  $307\text{ cm}^{-1}$  seems to represent the convolution of the  $A_1(2\text{TO})$  and  $A_1(2\text{LO})$ , attributed to the O–(B site cation)–O bending oscillations. The large width of the peaks at  $842$  and  $307\text{ cm}^{-1}$  could be explained by the fact that the sample contains 3 different cations at the same crystallographic place ( $\text{V}^{4+}$ ,  $\text{V}^{5+}$ ,  $\text{Fe}^{3+}$ ), each cation forming a different bond with the oxygen anions from the surrounding pyramid and each bonding is responsible for the development of a characteristic peak located at a slightly different wavenumber. Therefore what is observed is the convolution of these peaks. The peaks marked with star are not identified.

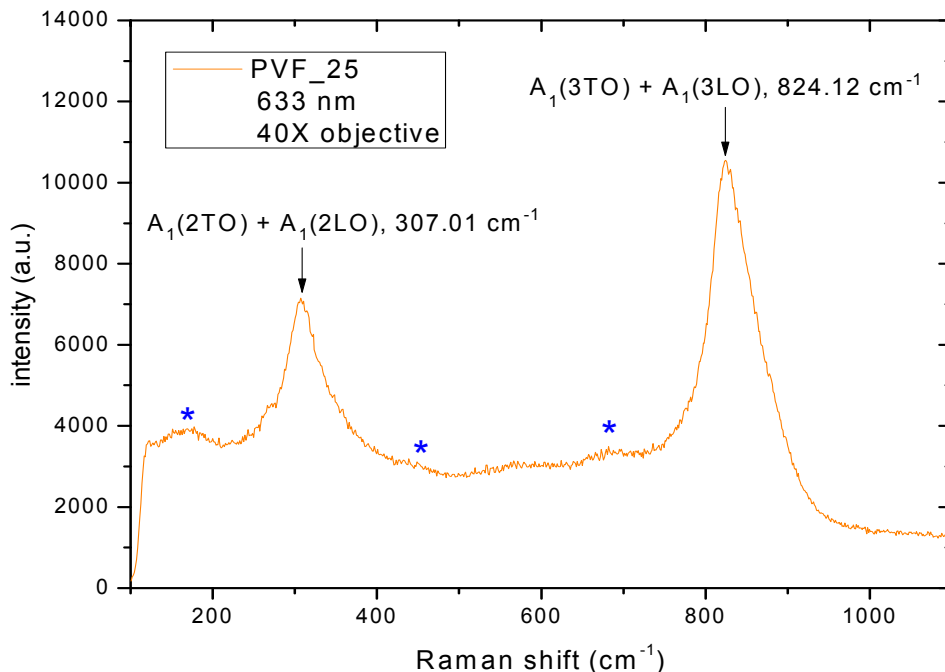


**Fig. 4.** Raman vibration modes for PVT\_25. The data was collected using the 40X objective. Laser power was set at 5% and the integration time was 10s. 9 integrations were made.

More information can be obtained by comparing the spectra of the four samples. This is shown on figure 5.

It can be observed that the most active vibrations are those that appear at high wavenumbers respectively  $A_1(3\text{TO})$  and  $A_1(3\text{LO})$  and belong to the B site cation - apical oxygen stretching. Their evolution is marked by line (1). Line (2) marks the evolution of the  $A_1(2\text{TO})$  and by extension  $A_1(2\text{LO})$  modes, associated to the bending of the O-B cation-O bond.

Two main effects are visible. The first effect is the widening and coalescence of peaks, which was described earlier.

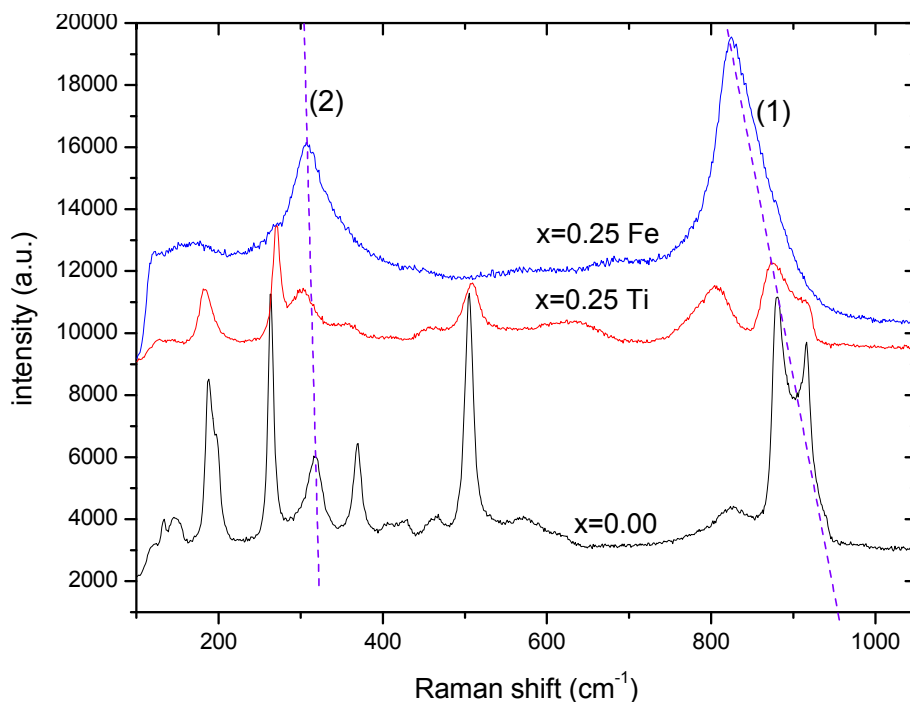


**Fig. 5.** The Raman spectra for  $x=0.00$  and  $x=0.25$  Ti and Fe samples. Two lines are plotted for eye guidance and to indicate the evolution of the vibration modes considered.

The second effect observed is the displacement of the peak position, more evident for line (1). The peaks at high wavenumbers (about  $800\text{ cm}^{-1}$ ) are displaced towards lower wavenumbers as the substitution degree increases. This suggests the weakening of the average B site cation - apical oxygen bond and is clearly observed between the sample containing 25% Fe.

## CONCLUSIONS

Solid state reaction under HP-HT conditions (6 GPa and  $950^\circ\text{C}$ ), lead to single phase of bulk  $\text{PbVO}_3$  and  $\text{PbV}_{1-x}\text{M}_x\text{O}_3$  ( $x=0.25$  and  $\text{M}=\text{Ti},\text{Fe}$ ) samples. EDX confirmed the nominal chemical composition of samples.

The most active Raman vibrations in our sample are  $A_1(3\text{TO})$  and  $A_1(3\text{LO})$  and belong to the B site cation - apical oxygen stretching (at high wavenumbers).

For the value  $x=0.25$ , the Raman spectra was found to be strongly dependent on the nature of 3d ions ( $\text{M}=\text{Ti}, \text{Fe}$ ) which substitute vanadium in  $\text{PbVO}_3$ .

In sample with  $x=0.25$  Ti, the ion  $\text{Ti}^{4+}$  is responsible for the local structural fluctuations because of the weaker bond to the apical oxygen and hence the formation of a different coordination.

The sample with  $\text{M}=\text{Fe}$  shows a spectra with only two very broad peaks, and are different from the spectra of undoped  $x=0.00$  and  $\text{M}=\text{Ti}$  doped samples. The Raman spectra for the  $x=0.25$  Fe can be explained by the fact that the sample contains 3 different cations at the same crystallographic place ( $\text{V}^{4+}$ ,  $\text{V}^{5+}$ ,  $\text{Fe}^{3+}$ ), with different bond length with oxygen anions.

## REFERENCES

- [1]. J.Wang, J.B. Neaton, H. Zheng, V. Nagarajan, S.B. Ogale, B. Liu, D. Viehland, V. Vaithyanathan, D.G. Schlom, U.V. Waghmare, N.A. Spaldin, K.M. Rabe, M. Wuttig, and R. Ramesh, *Science* 299, 1719 (2003).
- [2]. R.V. Shpanchenko, V.V. Chernaya, A.A. Tsirlin, P.V. Chizhov, D.E. Sklovsky, E.V. Antipov, E.P. Khlybov, V.Pomjakushin, A.M. Balagurov, J.E. Medvedeva, E.E. Kaul and C. Geibel, *Chem. Mater.* 16, 3267 (2004).
- [3]. A.A. Belik, M. Azuma, T. Saito, Y. Shimakawa, and M. Takano, *Chem. Mater.* 17, 269 (2005).
- [4]. E. Ching-Prado, A. Reynes-Figueroa, R.S. Katiyar, S.B. Majimder, and D.C. Agrawal, *J. Appl. Phys.* 78, 1920-1925 (1995).
- [5]. D. Valim, A.G. Souza Filho, P.T.C. Freire, J. Mendes Filho, C.A. Guavany, R.N. Reispaud, and E.B. Araujo, *J. Phys. D: Appl. Phys.*, 37, 744-747 (2004).
- [6]. J.A. Sanjurjo, E. Lopez-Cruz, and G. Burns, *Phys. Rev. B*, 28, 7260-7268 (1983).
- [7]. F. Cerdeira, W.B. Holzappel, and D. Bauerle, *Phys. Rev. B* 11, 1188-1192 (1975).

- [8]. D. Fu, T. Ogawa, H. Suzuki and K. Ishikawa, *Appl. Phys. Lett.* 77, 1532-1534 (2000).
- [9]. A.-D. Li, D. Wu, C.-Z. Ge, P. Lu, W.-H. Ma, M.-S. Zhang, C.-Y. Xu, J. Zuo, and N.-B. Ming, *J. Appl. Phys.*, 85, 2146-2150 (1999).
- [10]. P.S. Dobal, S. Bhaskar, S.B. Majamder, and R.S. Katiyar, *J. Appl. Phys.* 86, 828-834 (1999).
- [11]. L. Sun, Y.F. Chen, L. He, C.Z. Ge, D.S. Ding, T. Yu, M.-S. Zhang, and N.B. Ming, *Phys. Rev. B*, 55, 12218-12222 (1997).
- [12]. S.-H. Lee, H.M. Jang, S.M. Cho, and G.-C. Yi, *Appl. Phys. Lett.* 80, 17, 3165-3167 (2002).
- [13]. H. Zheng, J. Kreisel, Y.H. Chu, R. Ramesh, and L. Salamanca-Riba, *Appl. Phys. Lett.*, 90, 113113 1-3 (2007).
- [14]. I.A. Kornev, L. Bellaiche, P. Bouvier, P.E. Janolin, B. Dkhil, and J. Kreisel, *Phys. Rev. Lett.*, 95, 196804 1-4 (2005).
- [15]. I.A. Kornev and L. Bellaiche, *Phase Transitions*, 80, 385-413 (2007).
- [16]. G.A. Samara and E.L. Venturini, *Phase transitions*, 79, 21-40 (2006).
- [17]. Ausrine Bartasyte, *IEEE Transactions on Ultrasonics Ferroelectrics and Frequency Control*, 54, 2623-2631 (2007).
- [18] Al. Okos, Aurel Pop, Celine Darie, P. Bordet, *Studia UBB Chemia*, LVIII, 3, p. 57-62 (2013).
- [19]. Al. Okos, C. Colin, C. Darie, O. Raita, P. Bordet, A. Pop, *Journal of Alloys and Compounds* 602, pp. 265-268 (2014).
- [20]. A. Okos, A. Pop, C. Darie, P. Bordet, *Optoelectronics and Advanced materials- Rapid Communications* Vol. 8, No.3-4, p. 198 - 200 (2014).
- [21]. P. Bordet, C. Bougerol, C. Brachet, S. de Brion, G. Chouteau, F. Hipper, J. Kreisel, « Recherche par Synthèse haute pression de Nouvelles Perovskites Multiferroïques de Type (Bi,Pb)MO<sub>3</sub>, (M=métal de transition) », Meeting of the GDR NEEM, Aspet, France, 29 June-2 July 2004.
- [22]. S.D. Cheng, *Thin Solid Films*, 375, 109-113 (2000).
- [23]. Emre Erdem, *Journal of the European Ceramic Society*, 30, 289–293 (2010).
- [24]. A. Bartasyte, *Phase Transitions*, 84, 509–520 (2011).
- [25]. Al.Okos, *PhD Thesis*, "Synthesis and Characterization of Pb(V<sub>1-x</sub>M<sub>x</sub>)O<sub>3</sub> (M = Ti,Fe) compounds", 2014.

# OPTIMIZATION OF VARIOUS PARAMETERS FOR GRAPHENE SYNTHESIS BY THERMAL CHEMICAL VAPOR DEPOSITION (CVD) ON COPPER SUBSTRATE

B. MARTA<sup>a</sup>, C. LEORDEAN<sup>a</sup>, T. ISTVAN<sup>b</sup>,  
R. BARITCHI<sup>a</sup>, S. ASTILEAN<sup>a,b,\*</sup>

**ABSTRACT.** In the present study we report the synthesis of graphene through Chemical Vapor Deposition (CVD) and study the effects that different reaction parameters, such as the temperature and the gases used in the process, have upon the substrate and the resulting graphene, in order to optimize the synthesis process.

**Keywords:** *Graphene, CVD, synthesis*

## 1. INTRODUCTION

Graphene, a two-dimensional nanoscale allotrope of carbon, consisting of one layer of  $sp^2$  hybridized carbon atoms, bound in a honeycomb-like structure [1], is a promising material with many useful properties, including those of light transparency and electrical conductivity [2]. Over the past few years, research on graphene increased dramatically because of new methods to produce and study it [3]. There are usually two general approaches to synthesize graphene, namely, top-down, and bottom-up [4].

---

<sup>a</sup> *Nanobiophotonics and Laser Microspectroscopy Center, Interdisciplinary Research Institute in Bio-Nano-Sciences, Babes-Bolyai University, 1, M. Kogalniceanu Str., 400084, Cluj-Napoca, Romania*

<sup>b</sup> *Biomolecular Physics Dept., Faculty of Physics, Babes-Bolyai University, 1, M. Kogalniceanu Str., 400084, Cluj-Napoca, Romania*

\* *Corresponding author: simion.astilean@phys.ubbcluj.ro*

The top-down method generally utilizes pristine graphite, which, through different physical (e.g. scotch-tape exfoliation) or chemical (e.g. oxidative exfoliation) procedures is “broken” into thinner layers until it reaches a few atoms or even mono-atomic thickness (graphene)[5]. This approach can yield high quality graphene, with low defects, but it’s hardly scalable to millimeter or centimeter long flakes needed for various applications. Another approach is the bottom-up procedure in which carbon-rich molecules such as gaseous hydrocarbons (e.g. methane or acetylene) are decomposed in their constituting atoms through physic-chemical reactions, and the resulting carbon atoms bind together to form graphene, carbon quantum dots(CQD), or carbon nanotubes (CNT) [6]. The advantage of the bottom-up method is the fact that it allows the growth of graphene to an area of a few square centimeters, varying the reaction parameters (e.g. growth time).

Researchers have proposed many different uses for graphene ranging from flexible touch screens to transistors, solar cells, optical modulators, etc. Many of these proposals rely on graphene grown via chemical vapor deposition (CVD), a bottom-up method, which is a relatively new technique for producing large-area, high-quality graphene) [6]. Once created, CVD graphene is transferable to diverse substrates, making the technique versatile for many applications.

In the present study utilize the CVD method to grow graphene on thin copper films deposited on SiO<sub>2</sub>/Si substrates and study the effect different parameters in the recipe have on the graphene and substrate in order to optimize the synthesis process.

## **2. EXPERIMENTAL**

### **2.1. Chemicals and regents**

Argon (99.999%), Nitrogen (99.999%), CH<sub>4</sub> (99.9995%) and H<sub>2</sub> (99.999%) gases were purchased from Linde. 4” substrates consisting in copper (Cu) film of 500 nm thickness deposited on SiO<sub>2</sub>/Si wafers were provided by AIXTRON Nanoinstrument Ltd.

## 2.2. CVD setup

The schematic of AIXTRON's Black Magic BM II Flexible 2" R&D Reactor used in this study is illustrated in Figure 1. The gases are mixed and transported through the gas inlet and released into the reaction chamber through the showerhead. The catalytic substrate in this study is a thin copper (Cu) film deposited on SiO<sub>2</sub>/Si is placed on the heater. Chemical Vapour Deposition (CVD) synthesis is achieved by means of an energy transfer from an energy source (such as a resistively heated coil or plasma) to a hydrocarbon in gas phase (such as methane or acetylene). The energy transferred is used to break down the molecule into reactive carbon atoms. The carbon then diffuses towards the heated substrate, where it will bind to the catalytic surface. As the synthesis process takes place at low pressures, the reactor is connected to a pump system and an outlet system to dilute (using a ballast gas, N<sub>2</sub> in our case) and evacuate the by-products out of the reaction chamber.

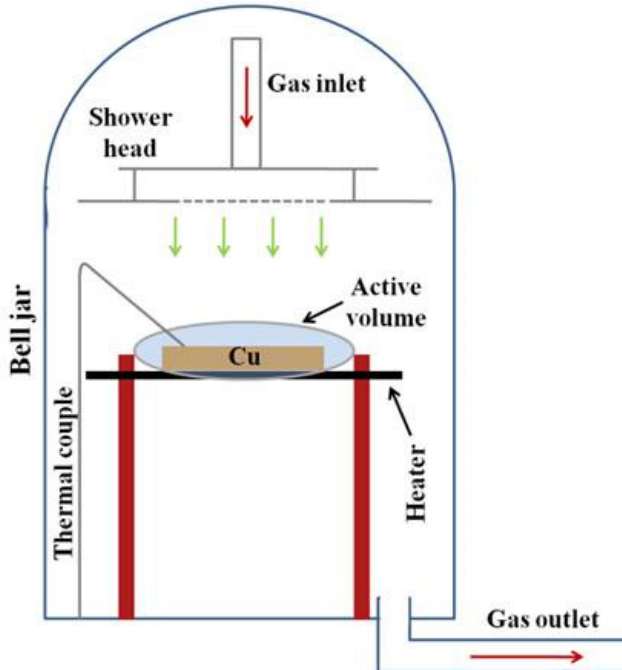


**Fig. 1.** Schematic of the CVD system used in this study.

### 2.3. Characterizing equipments

Copper substrate morphology was characterized by optical microscopy, scanning electron microscopy (SEM) using a FEI QUANTA 3D FEG system and atomic force microscopy (AFM) in tapping mode using a WITec alpha 300 R system. The quality of graphene layer was characterized by Raman spectroscopy using the Renishaw inVia Reflex Raman Microscope equipped with a RenCam CCD detector. The Raman microscope was coupled with an 80 mW He-Cd laser emitting at 442 nm and the spectra collected using a using a 0.9 NA objective of 100× magnification. Typical integration times were 10s and the power used was 750  $\mu$ W.

## 3. RESULTS AND DISCUSSION

### 3.1. CVD Graphene Synthesis

The graphene synthesis starts by pumping the CVD reactor down to 0.2 mbar in order to eliminate the air in the chamber (see Figure 2). Next Ar gas is set to flow in the reactor at 1000 standard cubic centimeters per minute (sccm) for 60 seconds. The Ar valve is then closed and the system is pumped down to 0.15 mbar. The process is repeated, flowing Ar at 1000 sccm for 60 seconds and then pumping it down to 0.1 mbar.

Run	Flow	Annealing	Growth	Cooling
Ar	1000 sccm	960 sccm	960 sccm	960 sccm
N <sub>2</sub> (ballast)	8000 sccm	8000 sccm	8000 sccm	8000 sccm
H <sub>2</sub>		40 sccm	40 sccm	40 sccm
CH <sub>4</sub>			10 sccm	

**Fig. 2.** Table containing the gas flow during the phases of a typical CVD synthesis process.

Finally, a mix of H<sub>2</sub>/Ar (40/960 sccm) is flowed in the reaction chamber, while heating the substrate at 760/770/780 °C using 3 standard operating procedures (SOP) for ramping up the temperature (see Figure 3). After the reaction temperature is reached, the substrate is kept under constant H<sub>2</sub>/Ar flow at this temperature for 5 min in order to stabilize gas flow, temperature fluctuations and to anneal the substrate. Next, 10 sccm of CH<sub>4</sub> is introduced in the reaction chamber along with the H<sub>2</sub>/Ar mixture for another 5 min. This represents the growth phase in which the carbon atoms resulting from methane molecule decomposition under the heat diffuse onto the copper substrate and start to form graphene through epitaxial growth. This process is sustained for 5 minutes at 760/770/780 °C. After that the methane flow is stopped and the system cooled down at 150 °C using SOPs for ramping down the temperature under H<sub>2</sub>/Ar flow (40/960 sccm). Next, the H<sub>2</sub> and Ar valves are closed and the reaction chamber is pumped down to 0.2 mbar. After that, air can be flowed in the installation, the bell jar can be lifted and the substrate removed. During the whole synthesis process N<sub>2</sub> is flowed at 8000 sccm to dilute the by-products and assure proper elimination.

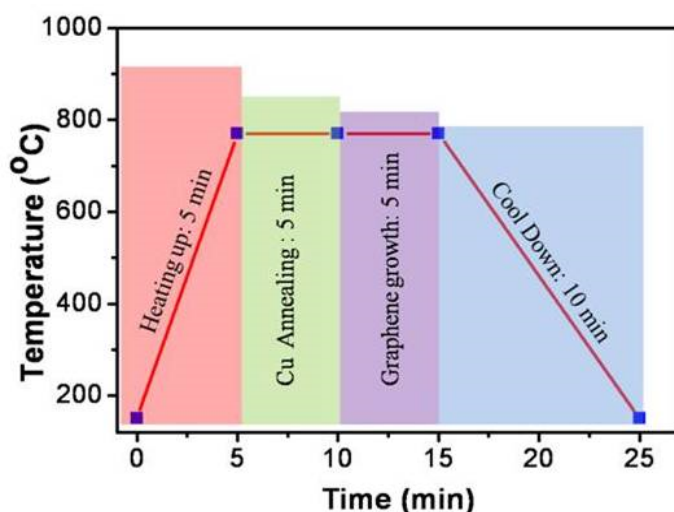


Fig. 3. Representing scheme of the CVD synthesis process.

In the experiments made to determine the influence of the gases used on the substrate (see section 2.2.2), the recipe used was similar to the one mentioned above, with some adjustments, namely: the substrate annealed in H<sub>2</sub> had a 1000 sccm H<sub>2</sub> flow in the annealing phase instead of H<sub>2</sub>/Ar, followed by a “growth” phase (the reheating) without CH<sub>4</sub>, in which Ar was introduced in the reaction chamber and the H<sub>2</sub>/Ar ratio adjusted gradually through an SOP at 40/960 sccm.

### **3.2. Synthesis parameters**

In order to improve the quality of the graphene synthesized through the CVD process, several parameters should be taken into account and optimized. Among the most important are growth and annealing temperature, gases purity, growth time, gas flow and pressure [7]. In the present work we study the effect of temperature and the gases used on the graphene quality. These two parameters have a major influence upon the results.

#### **3.2.1. Temperature**

First and foremost, we studied the effect of temperature during annealing and growth on the quality of graphene and the integrity of the substrates. As shown in Figure 4, the copper substrate suffers fragmentation and mass loss as function of temperature during the synthesis process. The fragmentation is a common behavior, caused by heating and rearranging of the copper atoms in larger microcrystals. This can be beneficial, the edges of these copper “islands” offering nucleation sites on which graphene can start to grow, although accumulation of carbon in these regions can lead to the development of multi-layers [8]. However, due to overheating of the substrate, the copper starts to evaporate and small holes start to form in the thing copper film. On top of these holes graphene growth is inhibited, so these holes can actually affect the continuity of the graphene layer, when trying to synthesize large-area, defect-free graphene. As shown in Figure 4(c), at 780 °C, the substrate suffers significant mass loss, leading to impartial coverage with graphene. The substrates prepared at 760 and 770 °C (Figure 4(a) and (b)) show more promise, having less damaged sites.

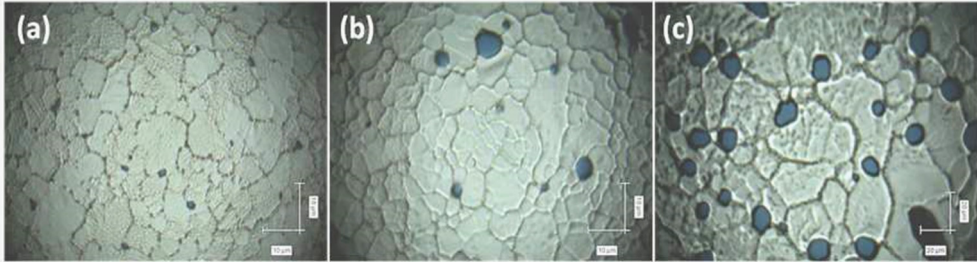


**Fig. 4.** Optical images of the copper substrates after CVD synthesis at (a) 760 °C, (b) 770 °C, (c) 780 °C.

We employed Raman spectroscopy to investigate the quality of the graphene obtained through each of the three recipes. In graphene, the Stokes phonon energy shift caused by laser excitation creates two main peaks in the Raman spectrum: G ( $1580\text{ cm}^{-1}$ ), a primary in-plane vibrational mode, and 2D ( $2690\text{ cm}^{-1}$ ), a second-order overtone of a different in-plane vibration, D ( $1350\text{ cm}^{-1}$ ) [9]. The D and 2D peak positions are dispersive (depend on the energy of the excitation laser)[10]. The 2D peak suffers significant changes (namely a splitting of the peak, into an increasing number of modes, which combine to form a shorter, and much wider 2D peak) as the number of the graphene layers increases. The G peak is also suffers a small redshift with the increasing number of layers. Thus the intensity ratio between the 2D and G peak ( $I_{2D}/I_G$ ) along with the full width at half maximum of the 2D peak (FWHM) can be used to accurately determine the number of graphene layers [11]. The intensity of D peak can be linked to the “disorder”, namely, atom displacement or other structural defects in graphene, and can be a good indicator of the quality (e.g. good conductivity) of graphene [12].

As it can be seen from Figure 5(a), although optically the substrate looks promising, there is poor coverage of the substrate with carbon, which is in graphitic form, denoted by the large 2D peak and a  $I_{2D}/I_G$  ratio of 1.3. By contrast, the graphene obtained at 770 °C (Figure 5(b)) has a good quality, as it results from the Raman spectra. The  $I_{2D}/I_G$  ratio (between 5-7) and the

FWHM of the 2D peak (between  $46\text{-}55\text{ cm}^{-1}$ ) hint the formation of monolayer to a few layers (2-3) of graphene [13]. The  $780\text{ }^\circ\text{C}$  recipe (Figure 5(c)) also yields graphene with a thickness ranging from monolayer to a few layers, as resulting from the  $I_{2D}/I_G$  ratios (between 4-8) and the FWHM of the 2D band between ( $49\text{-}53\text{ cm}^{-1}$ ) [13].

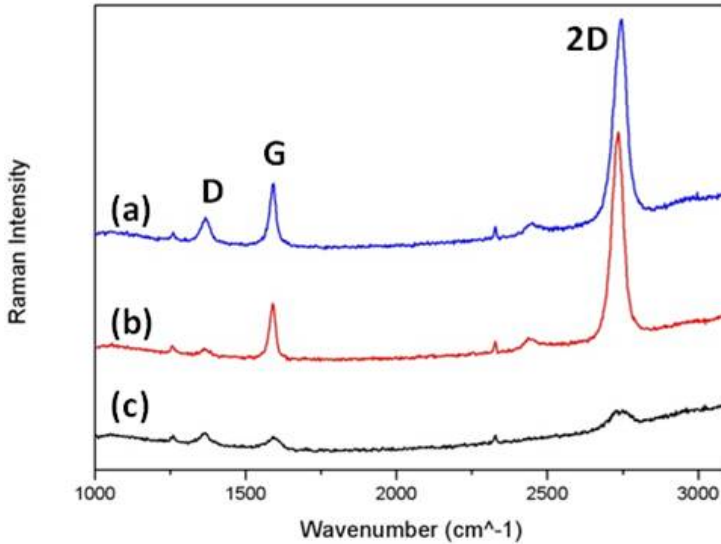


**Fig. 5.** Raman spectra of graphene synthesized on Cu substrates at different synthesis temperatures: (a)  $760\text{ }^\circ\text{C}$ , (b)  $770\text{ }^\circ\text{C}$ , (c)  $780\text{ }^\circ\text{C}$ . The spectra were recorded with  $442\text{ nm}$  laser line (He-Cd).

However the substrate shows more discontinuities in graphene coverage due to the holes caused by intensive evaporation of copper. It is also worth mentioning that the graphene obtained with this recipe has a more pronounced D peak, indicating a lower quality and more structural defects [13]. Thus we conclude that  $770\text{ }^\circ\text{C}$  is the optimal temperature for graphene synthesis among the ones tested for this particular substrate type and recipe.

### 3.2.2. Gases

Furthermore, we study the effects of different gases upon the morphology of substrate. During the annealing and deposition, the gases present in the CVD chamber could influence not only the growth rate of graphene, but also on the morphology of the substrate. A different morphology of the substrate can lead to different results, namely different flake sizes for graphene [14]. As it can be seen from the AFM map in Figure 6 (a), the substrate has a flat surface. When annealed in  $H_2$  atmosphere (Figure 6 (b)) the substrate becomes fragmented into micrometer sized “islands” formed of copper microcrystals. On the other hand, when the annealed substrate is heated again in an  $Ar/H_2$  atmosphere, its roughness changes significantly. Both when annealing or re-heating after annealing in  $H_2$ , in an  $Ar/H_2$  mixture, the substrate shows some “spikes” with heights between 10-30 nm. These spikes seem to occur due to the presence of Ar in the reaction chamber.

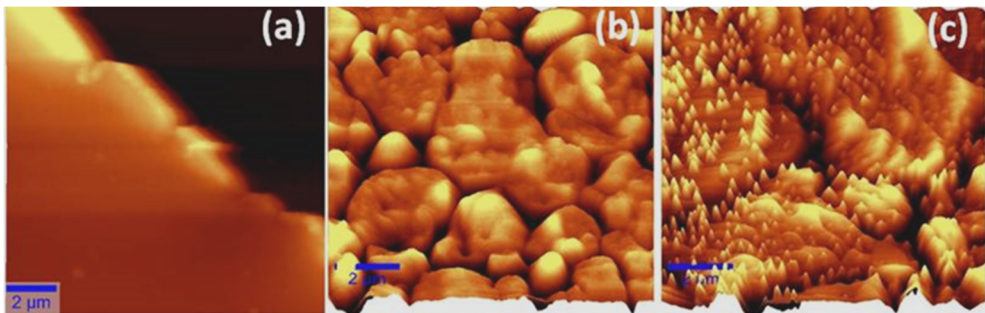


**Fig. 6.** AFM images of the (a) copper substrate before CVD synthesis, (b) copper substrate after annealing (5 min at 770 C) in  $H_2$  (1000 sccm), and (c) copper substrate after annealing(5 min at 770 °C) in  $H_2$  (1000 sccm) followed by another annealing (5 min at 770 °C) in  $Ar/H_2$  (960/40 sccm) atmosphere.

Next, we ran the whole recipe two times, once without  $CH_4$  in the growth phase (Figure 7(a)), and another time with a 10 sccm  $CH_4$  flow in the growth phase (Figure 7(b)). As it can be seen from the AFM maps, although the morphology of the copper substrate doesn't change (fragmentation of

the copper substrate and the spikes appear in both cases), the substrate appears more flattened due to the graphene film present on top of it which induces a thin deformation-resistant layer for the AFM tip. The SEM image (Figure 7 (c)) confirms the morphology of the substrate from figure 5 (b). The spikes seen in the AFM maps appear to be dendritic formations of copper with a height of 10-30 nm and a width of a few tens of nanometers.

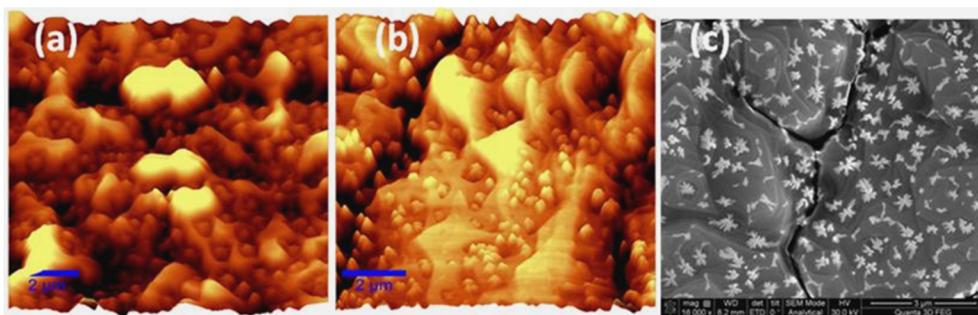


**Fig. 7.** AFM images of (a) copper substrate after 10 min at 770 °C in Ar/H<sub>2</sub> (960/40 sccm) atmosphere, (b) copper substrate after annealing (5 min at 770 °C) in Ar/H<sub>2</sub> (960/40 sccm) followed by synthesis (5 min at 770 °C) in Ar/H<sub>2</sub>/CH<sub>4</sub> (960/40/10 sccm). (c) SEM image of the copper substrate from (b).

The gases used don't seem to affect too much the quality of graphene although the morphology of the substrate changes significantly. Extensive work is required to determine and better understand the formation and effect upon graphene of the metallic “spikes” formed in the presence of Ar.

#### 4. CONCLUSIONS

In this study we managed to obtain large-area, high-quality graphene using a temperature optimized CVD recipe. Firstly, we concluded that the synthesis temperature plays a crucial role in the CVD process, affecting the quality of the graphene and the integrity of the substrate.

Secondly, we analyzed the effect that the gases used in the recipe have upon the Cu substrate. An interesting morphological change in the surface roughness of the substrate, which can be linked to the presence of Argon in the reaction chamber, was observed. The optimization of these parameters to control the quality of graphene is needed to implement the graphene into nanodevice fabrication.

## REFERENCES

- [1] C. Riedl, C. Coletti, and U. Starke, *J. Phys. Appl. Phys.*, vol. 43, 374009 (2010).
- [2] A.N. Grigorenko, M. Polini, and K. S. Novoselov, *Nat. Photonics*, 6, 749 (2012).
- [3] A.K. Geim and K. S. Novoselov, *Nat. Mater.*, 6, 183 (2007).
- [4] J.M. Tour, *Chem. Mater.*, 26, 163 (2013).
- [5] M. Lotya, Y. Hernandez, P.J. King, R.J. Smith, V. Nicolosi, L.S. Karlsson, F.M. Blighe, S. De, Z. Wang, I.T. McGovern, G.S. Duesberg, and J.N. Coleman, *J. Am. Chem. Soc.*, 131, 3611 (2009).
- [6] K.S. Kim, Y. Zhao, H. Jang, S.Y. Lee, J.M. Kim, K.S. Kim, J.-H. Ahn, P. Kim, J.-Y. Choi, and B.H. Hong, *Nature*, 457, 706 (2009).
- [7] A. Dathbun and S. Chaisitsak, *2013 8th IEEE International Conference on Nano/Micro Engineered and Molecular Systems (NEMS)*, 1018 (2013).
- [8] Y. Zhang, L. Gomez, F. N. Ishikawa, A. Madaria, K. Ryu, C. Wang, A. Badmaev, and C. Zhou, *J. Phys. Chem. Lett.*, 1, 3101 (2010).
- [9] R. Saito, M. Hofmann, G. Dresselhaus, A. Jorio, and M.S. Dresselhaus, *Adv. Phys.*, 60, 413 (2011).
- [10] A.C. Ferrari, *Solid State Commun.*, 143, 47 (2007).
- [11] A.C. Ferrari, J.C. Meyer, V. Scardaci, C. Casiraghi, M. Lazzeri, F. Mauri, S. Piscanec, D. Jiang, K.S. Novoselov, S. Roth, and A.K. Geim, *Phys. Rev. Lett.*, 97, 187401 (2006).
- [12] C. Thomsen and S. Reich, *Phys. Rev. Lett.*, 85, 5214 (2000).
- [13] A.C. Ferrari and D.M. Basko, *Nat. Nanotechnol.*, 8, 235 (2013).
- [14] I. Vlassiouk, M. Regmi, P. Fulvio, S. Dai, P. Datskos, G. Eres, and S. Smirnov, *ACS Nano*, 5, 6069 (2011).



## PEROXIDE BINDING TO Fe(IV) CENTERS: INVOLVEMENT OF Fe(III)-SUPEROXIDE REDOX ISOMERS

RADU SILAGHI-DUMITRESCU<sup>a,\*</sup> and DANIELA CIOLOBOC<sup>a</sup>

**ABSTRACT.** Hydroperoxide binding to Fe(IV)-oxo centers is known experimentally. In related Fe(III) centers, peroxide binding to iron is often accompanied by redox isomerism phenomena, where the metal and the peroxy ligand exchange one electron. Here, the electronic structure of Fe(IV)-hydroperoxo adducts is investigated with density functional calculations (DFT), showing that a Fe(III)-superoxide redox isomer is accessible, and that the equilibrium between this redox isomer and the Fe(IV)-hydroperoxo is shifted by the nature of the remaining ligands, with nitrogen ligands and especially an oxo ligand favoring the Fe(IV) redox isomer.

**Keywords:** *ferryl, redox isomerism, DFT, peroxide, iron enzymes*

### INTRODUCTION

Fe(IV)-oxo ( $[\text{FeO}]^{2+}$ , ferryl) centers are well-established components of various catalytic reaction intermediates in oxygenases as well as in model complexes.(1-4) Such are the Compound II species of several hemoproteins (where the ferryl is inserted in a heme),(4,5) Compound I (which compared to

---

<sup>a</sup> *Departments of Chemistry, Babes-Bolyai University, 11 Arany Janos Street, Cluj-Napoca, Romania*

\* *Corresponding author: rsilaghi@chem.ubbcluj.ro*

Compound II has one missing electron on the porphyrin ligand, which thus becomes a cation radical coupled to the  $S=1$  ferryl center),(4,5) and a number of non-heme iron centers in enzymes such as ketoglutarate-dependant monooxygenases and, to some extent Rieske dioxygenases.(1) The nature of bonding within the ferryl moiety has been discussed extensively,(6-16) and shown to involve, as key players, two singly occupied  $\pi^*$  iron-oxygen orbitals, in a picture very similar to that seen in molecular oxygen. The essentially *even* manner in which electron density is distributed between iron and oxygen within this  $\pi^*$  system according to density functional calculations (DFT) has allowed for speculations on the issue of which atom these electrons belong to formally; thus depending on the choice (iron vs. oxygen), redox isomers such as Fe(IV)-oxo, Fe(III)-oxyl and Fe(II)-oxygen atom can all be invoked. Hartree-Fock (HF) and post-HF results have been invoked in order to question the entirely covalent picture yielded by DFT; detailed analyses of related systems have also pointed out to the concept that formally Fe(IV)-oxo systems may in fact show significant contributions from Fe(III) or even Fe(II) redox isomers.(17)

Ferric-hydroperoxo centers are also well-known in many enzymes and model compounds; with few exceptions, they are intermediates en route to formation of the ferryl species, discussed above. The electronic structures of ferric-hydroperoxo centers was studied extensively, and there appears to be a consensus according to which the alternative redox isomer, Fe(II)-OOH<sup>0</sup>, is not an important part of the structure in any of the biologically-relevant centers examined to date.(18-23)

An Fe(IV)-alkylperoxo center was described by Que and co-workers(24) in a model compound; this complex appears to be a hybrid between the above-discussed ferryl and ferric-hydroperoxo systems, and therefore presents an interesting problem of electronic structure, insofar as it may in principle allow redox isomers wherein the hydroperoxo ligand has become oxidized to yield a protonated superoxide, OOH<sup>0</sup> (or its alkyl derivatives). This possibility is explored in the present manuscript with computational methods, and it is shown that depending on the remaining ligands at the iron, the Fe(IV)-hydroperoxo system can indeed offer a distinctly wider range of electronic structures than its better characterized ferric-hydroperoxo counterparts.

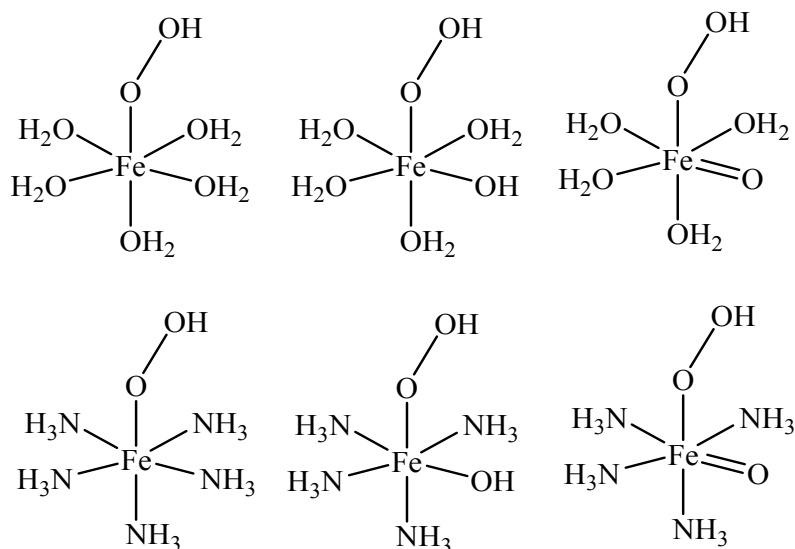
## EXPERIMENTAL

Figure 1 shows the models employed in the present work. Geometries were optimized without any constraints using the BP86 functional, which uses the gradient corrected exchange functional proposed by Becke (1988)(25) and the correlation functional by Perdew (1986),(26) and the 6-31G\*\* basis set were used as implemented in *Spartan*.(27) For the SCF calculations, a fine grid was used and the convergence criteria were set to  $10^{-6}$  (for the root-mean square of electron density) and  $10^{-8}$  (energy), respectively. For geometry optimization, convergence criteria were set to 0.001 au (maximum gradient criterion) and 0.0003 (maximum displacement criterion). Charges and spin densities were derived from Mulliken population analyses after DFT geometry optimization. Molecular dynamic (MD) simulations were performed using the extended Lagrangian approach with the ADMP (Atom Centered Density Matrix Propagation) model using the same functional and basis sets used for the optimizations as implemented in Gaussian09.(28) MD calculations were run at room temperature, with converged SCF result at each point, with a time step of 1 femtosecond.

## RESULTS AND DISCUSSION

The models employed in the present study (Figure 1) include octahedral systems with an Fe(IV) center bound to a hydroperoxide; the remaining five ligands are water or ammonia, unless one of them is substituted by a hydroxide or by an oxo ligand.

Table 1 shows key geometrical and electronic structure parameters for the DFT-optimized geometries of the models shown in Figure 1. These data will be examined in terms of their ability to distinguish between the two possible redox isomers for interest in this study: Fe(IV)-OOH<sup>-</sup> and Fe(III)-OOH<sup>0</sup>.



**Figure 1.** Models employed in the present study.

**Table I.** Key geometrical parameters, partial atomic charges and spin densities (the latter shown in parentheses) for the models employed in the present study.

	Fe-OOH	O-OH	Fe	O <sup>a</sup>	OH <sup>b</sup>	O/OH <sup>c</sup>
[Fe(H <sub>2</sub> O) <sub>5</sub> (OOH)] <sup>2+</sup>	1.85	1.36	0.76 (1.15)	-0.09 (0.38)	0.39 (0.33)	-
[Fe(H <sub>2</sub> O) <sub>4</sub> (OH)(OOH)] <sup>+</sup>	1.80	1.41	0.71 (1.28)	-0.18 (0.31)	0.21 (0.18)	0.01 (0.27)
[Fe(H <sub>2</sub> O) <sub>4</sub> (O)(OOH)]	1.81	1.48	0.64 (1.32)	-0.30 (-0.02)	0.06 (-0.02)	-0.47 (0.70)
[Fe(H <sub>3</sub> N) <sub>5</sub> (OOH)] <sup>2+</sup>	1.85	1.39	0.53 (1.50)	-0.10 (0.39)	0.33 (0.26)	-
[Fe(H <sub>3</sub> N) <sub>4</sub> (OH)(OOH)] <sup>+</sup>	1.82	1.43	0.55 (1.37)	-0.22 (0.31)	0.14 (0.14)	-0.05 (0.27)
[Fe(H <sub>3</sub> N) <sub>4</sub> (O)(OOH)]	1.86	1.50	0.58 (1.28)	-0.34 (0.02)	0 (-0.01)	-0.43 (0.74)
Free HOOH <sup>0</sup>	-	1.48	-	0	0	-
Free OOH <sup>0</sup>	-	1.35	-	-0.20 (0.70)	0.20 (0.30)	-

<sup>a</sup>iron-bound oxygen within the OOH ligand.

<sup>b</sup>non-iron-bound oxygen within the OOH ligand (charge and spin density summed up with those of the proton attached to this oxygen atom).

<sup>c</sup>oxo or hydroxo ligand (charge and spin density summed up with that of the proton, if any).

The O-O bond for the iron complexes in Table 1 varies between 1.50 and 1.36 Å. At one end are the models where there are no oxo or hydroxo ligands cis to the hydroperoxide. Here, the O-O bond is within 0.01-0.03 Å of that computed for free superoxide,  $\text{OOH}^0$ , suggesting that an Fe(III)-superoxide redox isomer would be most appropriate for describing the electronic structure in these two models. Indeed, internal bond lengths between diatomic ligands were previously shown to be one of the most accurate indicators of electronic structures in problematic redox isomerism cases of iron complexes.<sup>(29)</sup> Spin densities computed for the OOH ligand in the two models,  $[\text{Fe}(\text{H}_2\text{O})_5(\text{OOH})]^{2+}$  and  $[\text{Fe}(\text{H}_3\text{N})_5(\text{OOH})]^{2+}$ , are 0.71 and, respectively, reasonably close to the  $\sim 1$  unit expected of a true superoxide ligand. Furthermore, the overall charges on the OOH ligand in these two models, of 0.30 and 0.08, are very far from the -1 charge expected of a hydroperoxide ligand. One can therefore see that very much like in the case of the ferryl moiety, the Fe(IV) center can take advantage of the redox isomerism ability of the ligand, hydroperoxide, and engage in electron transfer so that an Fe(III)-type structure needs to be taken in consideration.

At the opposite end to the penta-aqua and penta-ammine models, are  $[\text{Fe}(\text{H}_2\text{O})_4(\text{O})(\text{OOH})]$  and  $[\text{Fe}(\text{H}_3\text{N})_4(\text{O})(\text{OOH})]$ , featuring an oxo ligand cis to the OOH, and in which the O-O bond lengths are 1.48 and 1.50 Å, respectively. These values are now essentially identical, if not even slightly larger, to what is computed in free hydrogen peroxide, suggesting that in these models the OOH ligand has a very strong hydroperoxide character. Indeed, spin densities on the OOH group have dropped to  $\sim 0.01$  and the sum of partial atomic charges is distinctly negative: -0.24 and -0.34 units, respectively.

The models where a hydroxide ligand is found cis to the hydroperoxide can be feature O-O bond lengths intermediate between those of the oxo and those of the non-oxo models: 1.41 and 1.43 Å, which is  $\sim$  half way between what is computed for free hydrogen peroxide and free superoxide (1.48 to 1.36 Å).

Figure 2 illustrates O-O evolution in time as they result from molecular dynamic calculations on two of the models,  $[\text{Fe}(\text{NH}_3)_4(\text{O})(\text{OOH})]^+$  and  $[\text{Fe}(\text{HO}_2)_4(\text{O})(\text{OOH})]^+$ . The O-O bond oscillates with an amplitude of

$\sim 0.2 \text{ \AA}$  between  $1.4 \text{ \AA}$  – length typical for superoxide O-O bond, up to  $\sim 1.6 \text{ \AA}$  – slightly longer than the one computed for free hydroperoxide at equilibrium. These geometric fluctuations that take place on a very short time scale may suggest also changes in electronic structure in terms of the relative contribution of the two redox isomers.

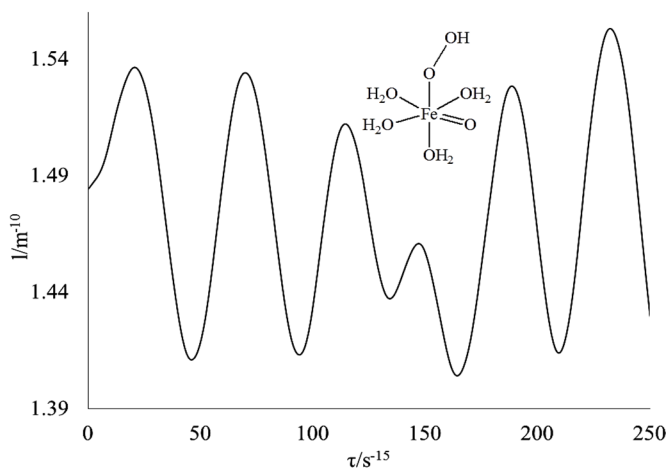


**Figure 2.** O-O bond lengths over a course of 250 femtoseconds in the  $[\text{Fe}(\text{NH}_3)_4(\text{O})(\text{OOH})]^+$  (upper panel) and  $[\text{Fe}(\text{HO}_2)_4(\text{O})(\text{OOH})]^+$  (lower panel) models.

The iron-oxygen bond in high-valent oxo and hydroxo complexes may also be deemed to be subject to redox isomerism; thus the Fe(IV)-(hydr)oxo state would be in competition with an Fe(III)-(hydr)oxyl redox isomer.<sup>(16)</sup> Figure 3 displays molecular dynamic results monitoring the Fe(IV)-O bond in the Fe-oxo and Fe-hydroxo models  $[\text{Fe}(\text{NH}_3)_4(\text{O})(\text{OOH})]^+$ ,  $[\text{Fe}(\text{HO}_2)_4(\text{O})(\text{OOH})]^+$  and  $[\text{Fe}(\text{HO}_2)_4(\text{OH})(\text{OOH})]^0$ . The iron-oxo bond oscillates between  $\sim 1.56 \text{ \AA}$  – value lightly shorter than computed an Fe-N *triple* bond - and  $\sim 1.68 \text{ \AA}$  – value close to a Fe-O double bond. The iron-hydroxo bond oscillates with an amplitude of  $0.14 \text{ \AA}$  between  $1.66 \text{ \AA}$ , value attributable to Fe-O double bond, up to  $1.8 \text{ \AA}$  value slightly longer than computed at equilibrium for Fe(III)-hydroxo. Such oscillations over a few hundred femtoseconds suggest that interconversion between redox isomers may occur extremely rapid at non-zero temperatures.

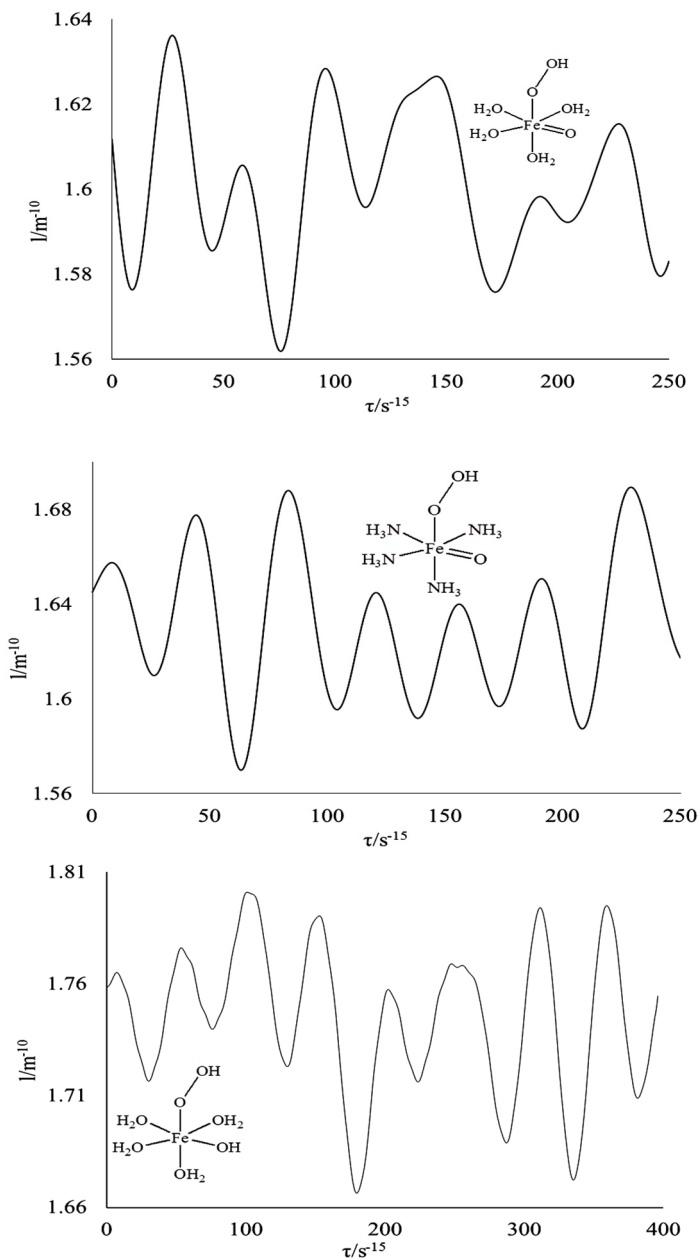


**Figure 3.** Fe-O bond lengths in the [Fe(NH<sub>3</sub>)<sub>4</sub>(O)(OOH)]<sup>+</sup> (upper panel) and [Fe(H<sub>2</sub>O)<sub>4</sub>(O)(OOH)]<sup>+</sup> (middle panel) and [Fe(H<sub>2</sub>O)<sub>4</sub>(OH)(OOH)]<sup>2+</sup> (lower panel).

## CONCLUSIONS

The Fe(IV) center was found to engage in redox isomerism phenomena with a hydroperoxide ligand, in a manner controlled by the remaining iron ligands. Thus, an additional oxo ligand appears to offer even more capability for redox isomerism than the OOH, and therefore the hydroperoxide ligand remains intact; a partial effect along the same lines has the hydroxide ligand. However, in the absence of such competitors, Fe(IV) engages in electron transfer with hydroperoxide, leading to a structure clearly describable as Fe(III) bound to neutral superoxide, OOH<sup>0</sup>.

## Acknowledgements

Funding from the Romanian Ministry of Education and Research (PCCE 140/2008 and PCE 488/2012) is gratefully acknowledged.

## REFERENCES

1. Costas, M., Mehn, M.P., Jensen, M.P. and Que, L.J. (2004) Dioxygen Activation at Mononuclear Nonheme Iron Active Sites: Enzymes, Models and Intermediates. *Chem. Rev.* 2, 939-986
2. Solomon, E.I., Decker, A. and Lehnert, N. (2003) Non-heme iron enzymes: contrasts to heme catalysis. *Proc Natl Acad Sci U S A* 100, 3589-3594
3. Silaghi-Dumitrescu, R., Reeder, B.J., Nicholls, P., Cooper, C.E. and Wilson, M.T. (2007) Ferryl haem protonation gates peroxidatic reactivity in globins. *Biochem J* 403, 391-395
4. Silaghi-Dumitrescu, R. (2004) The nature of the high-valent complexes in the catalytic cycles of hemoproteins. *J. Biol. Inorg. Chem.* 9, 471-476
5. Sono, M., Roach, M.P., Coulter, E.D. and Dawson, J.H. (1996) Heme-containing oxygenases. *Chem. Rev.* 96, 2841-2888
6. Shaik, S., de Visser, S.P., Ogliaro, F., Schwarz, H. and Schröder, I. (2002) TSR. *Curr. Opin. Chem. Biol.* 6, 556-567

7. Shaik, S., Cohen, S., de Visser, S.P., Sharma, P.K., Kumar, D., Kozuch, S., Ogliaro, F. and Danovich, D. (2004) The "Rebound Controversy": An Overview and Theoretical Modeling of the Rebound Step in C-H Hydroxylation by Cytochrome P450. *Eur. J. Inorg. Chem.*, 207-226
8. Shaik, S., de Visser, S.P. and Kumar, D. (2004) External electric field will control the selectivity of enzymatic-like bond activations. *J Am Chem Soc* 126, 11746-11749
9. Shaik, S., de Visser, S.P. and Kumar, D. (2004) One oxidant, many pathways: a theoretical perspective of monooxygenation mechanisms by cytochrome P450 enzymes. *J Biol Inorg Chem* 9, 661-668
10. Shaik, S., Kumar, D., de Visser, S.P., Altun, A. and Thiel, W. (2005) Theoretical perspective on the structure and mechanism of cytochrome P450 enzymes. *Chem Rev* 105, 2279-2328
11. Shaik, S., Kumar, D. and de Visser, S. P. (2008) A Valence Bond Modeling of Trends in Hydrogen Abstraction Barriers and Transition States of Hydroxylation Reactions Catalyzed by Cytochrome P450 Enzymes. *J Am Chem Soc* 130, 10128-10140
12. Harris, D.L. (2001) High-valent intermediates of heme proteins and model compounds. *Curr. Opin. Chem. Biol.* 5, 724-735
13. Harris, D.L. (2002) oxidation and electronic state dependence of proton transfer in the enzymatic cycle of cytochrome P450-eryF. *J. Inorg. Biochem.* 91, 568-585
14. Silaghi-Dumitrescu, R. and Makarov, S.V. (2010) Hydrocarbon activation by iron-nitrite adducts. *Eur J Inorg Chem* 34, 1830-1833
15. Silaghi-Dumitrescu, R. (2007) Electronic structures of Fe(IV) and Fe(V) systems with oxo, sulphido and nitrido ligands in octahedral environments. *Rev. Chim.* 58, 461-464
16. Silaghi-Dumitrescu, R. (2005) "High-valent" ferryl-oxo complexes: how "high" are they really? *Studia Univ. Babeş-Bolyai, Chemia* 50, 17-21
17. Silaghi-Dumitrescu, R. (2013) Redox activation of small molecules at biological metal centers. *Structure & Bonding* 150, 97-118
18. Silaghi-Dumitrescu, R. (2004) Factors controlling O-O bond cleavage in ferric-hydroperoxo complexes. *Proc. Rom. Acad. Series B* 3

19. Silaghi-Dumitrescu, R. and Cooper, C.E. (2005) Transient species involved in catalytic dioxygen/peroxide activation by hemoproteins: possible involvement of protonated Compound I species. *Dalton Trans.*, 3477-3482
20. Silaghi-Dumitrescu, R., Silaghi-Dumitrescu, I., Coulter, E.D. and Kurtz, D.M., Jr. (2003) Computational study of the non-heme iron active site in superoxide reductase and its reaction with superoxide. *Inorg. Chem.* 42, 446-456
21. Lehnert, N., Ho, R.Y.N., Que, L.J. and Solomon, E.I. (2001) spectroscopic properties and electronic structure of low-spin... *J. Am. Chem. Soc.* 123, 8271-8290
22. Lehnert, N., Ho, R.Y.N., Que, L.J. and Solomon, E.I. (2001) electronic structure of high-spin Fe<sup>3+</sup>-alkylperoxo. *J. Am. Chem. Soc.* 122, 12802-12816
23. Lehnert, N., Neese, F., Ho, R.Y., Que, L., Jr. and Solomon, E.I. (2002) Electronic structure and reactivity of low-spin Fe(III)-hydroperoxo complexes: comparison to activated bleomycin. *J. Am. Chem. Soc.* 124, 10810-10822
24. Jensen, M.P., Costas, M., Ho, R.Y., Kaizer, J., Mairata, I.P.A., Munck, E., Que, L., Jr., Rohde, J.U. and Stubna, A. (2005) High-Valent Nonheme Iron. Two Distinct Iron(IV) Species Derived from a Common Iron(II) Precursor. *J Am Chem Soc* 127, 10512-10525
25. Becke, A.D. (1988) Density-functional exchange-energy approximation with correct asymptotic behaviour. *Phys. Rev.*, 3098-3100
26. Perdew, J.P. (1986) Density-functional approximation for the correlation energy of the inhomogeneous electron gas. *Phys. Rev. B* 33, 8822-8824
27. Spartan, S. Spartan 5.0, Wavefunction, Inc., 18401 Von Karman Avenue Suite 370, Irvine, CA 92612 U.S.A. Spartan 5.0, Wavefunction, Inc., 18401 Von Karman Avenue Suite 370, Irvine, CA 92612 U.S.A.
28. Frisch, M.J., Trucks, G.W., Schlegel, H.B., Scuseria, G.E., Robb, M.A., Cheeseman, J.R., Montgomery, J., J.A., Vreven, T., Kudin, K.N., Burant, J.C., Millam, J.M., Iyengar, S.S., Tomasi, J., Barone, V., Mennucci, B., Cossi, M., Scalmani, G., Rega, N., Petersson, G. A., Nakatsuji, H., Hada, M., Ehara, M., Toyota, K., Fukuda, R., Hasegawa, J., Ishida, M., Nakajima, T., Honda, Y., Kitao, O., Nakai, H., Klene, M., Li, X., Knox, J. E., Hratchian, H. P., Cross, J.B., Bakken, V., Adamo, C., Jaramillo, J., Gomperts, R., Stratmann, R.E., Yazyev, O., Austin, A.J., Cammi, R., Pomelli, C., Ochterski, J.W., Ayala, P.Y., Morokuma, K., Voth, G.A., Salvador, P., Dannenberg, J.J., Zakrzewski, V.G., Dapprich, S., Daniels, A.D., Strain, M.C., Farkas, O., Malick, D.K., Rabuck, A.D., Raghavachari, K., Foresman, J.B., Ortiz, J.V., Cui, Q., Baboul,

- A.G., Clifford, S., Cioslowski, J., Stefanov, B. B., Liu, G., Liashenko, A., Piskorz, P., Komaromi, I., Martin, R.L., Fox, D.J., Keith, T., Al-Laham, M.A., Peng, C.Y., Nanayakkara, A., Challacombe, M., Gill, P.M.W., Johnson, B., Chen, W., Wong, M.W., Gonzalez, C. and Pople, J.A. (2009). Gaussian 09 r. A1; Gaussian, Inc., Wallingford CT
29. Silaghi-Dumitrescu, R. and Silaghi-Dumitrescu, I. (2006) DFT and the electromerism in complexes of iron with diatomic ligands. *J. Inorg. Biochem.* 100, 161-166



## VIBRATIONAL STUDY OF 1-PHENYL-PYRAZOLE AND 4-Me-1-PHENYL-PYRAZOLE COMPOUNDS

I.J. HIDI<sup>a,b</sup>, L. BAIA<sup>c</sup>, J. POPP<sup>a,b</sup>, M. BAIA<sup>c,\*</sup>

**ABSTRACT.** Pyrazole derivatives are known as compounds that can be used in pharmacological and medical applications. In the present study a detailed vibrational analysis of two pyrazole derivatives, 1-phenyl-pyrazole and 4-Me-1-phenyl-pyrazole, was performed by means of Raman and infrared (IR) spectroscopy corroborated by density functional theory (DFT) simulations. The optimization of the investigated compounds' geometry was initially obtained followed by a normal modes calculation. The obtained results showed a relatively good agreement between the experimental and theoretical data.

**Keywords:** *pyrazole derivatives, Raman, SERS, DFT*

### 1. INTRODUCTION

Pyrazole derivatives are commonly used in medicine for their analgesic, anti-inflammatory, antipyretic, antiarrhythmic, tranquilizing, muscle relaxing, psychoanaleptic and anticonvulsant, monoamine oxidase inhibiting, antidiabetic and antibacterial activities [1-3]. Moreover, these molecules have

---

<sup>a</sup> *Friedrich-Schiller University, Institute of Physical Chemistry & Abbe Center of Photonics, 07743 Jena, Germany*

<sup>b</sup> *Leibniz Institute of Photonic Technology, 07745 Jena, Germany*

<sup>c</sup> *Babes-Bolyai University, Faculty of Physics & Interdisciplinary Research Institute on Bio-Nano-Sciences, 400084 Cluj-Napoca, Romania*

\* *Corresponding author: monica.baia@phys.ubbcluj.ro*

been also reported as showing antifungal [4], insecticidal [5], herbicidal [6] activities. In order to understand their mode of action it is essential to find out if the structure of the adsorbed species is similar to that of the free molecule. The investigations reported herewith use a silver surface as an analogue for an artificial biological interface. After elucidating the adsorption mechanism of the molecule, the study can be expanded to the adsorption on membranes or other interesting biological surfaces for medical or therapeutic treatments [7].

In the present study, a detailed vibrational analysis of the pyrazole derivatives, 1-phenyl-pyrazole and 4-Me-1-phenyl-pyrazole was performed by means of IR and Raman spectroscopy corroborated by density functional theory (DFT) calculations.

## 2. EXPERIMENTAL

### Materials and Spectroscopic Methods

The pyrazole derivatives, 1-phenyl-pyrazole and 4-Me-1-phenyl-pyrazole were purchased from commercial sources as analytical pure reagents.

The FT-Raman spectra were recorded by using a Bruker Equinox 55 spectrometer with an integrated FRA 106 Raman module and a spectral resolution of  $2\text{ cm}^{-1}$ . Radiation of 1064 nm from an Nd-YAG laser was employed for Raman excitation. The infrared spectra were recorded with a Bruker IFS 25 spectrometer and a spectral resolution of  $2\text{ cm}^{-1}$ .

### Computational Details

Theoretical calculations of the structure and the harmonic vibrational wavenumbers of the investigated compounds were performed using the Gaussian 98 program package [8]. DFT calculations were carried out with Becke's 1988 exchange functional [9], the Perdew-Wang 91 gradient corrected correlation functional (BPW91) [10], and Becke's three parameter hybrid

method using the Lee-Yang-Parr correlation functional (B3LYP) [11] together with the 6-311+G\* Pople split-valence polarization basis, which was used for the geometry optimization and the normal modes calculation. No imaginary frequency modes were obtained for the optimized structures of the examined species proving that a local minimum of the potential energy surface was found.

### 3. RESULTS AND DISCUSSION

The two title compounds have an overall structure which consists of two planar cycles, a phenyl and a pyrazole ring. They are differentiated only by the presence of the methyl group in the case of 4-Me-1-phenyl-pyrazole. The schematic structure of the compounds with the labeling of the atoms is given in Fig. 1.

The optimized geometries of both pyrazole derivatives calculated at the B3LYP/6-311+G\* theoretical level are illustrated in Fig. 2. Analytical harmonic vibrational modes have also been calculated in order to ensure that the optimized structures correspond to minima on the potential energy surface. The theoretical calculations reveals that the value of the  $N_2N_1C_6C_{11}$  dihedral angle formed between the phenyl and pyrazole rings is of 143.73 and 157.68 degrees for 1-phenyl-pyrazole and 4-Me-1-phenyl-pyrazole compounds, respectively.

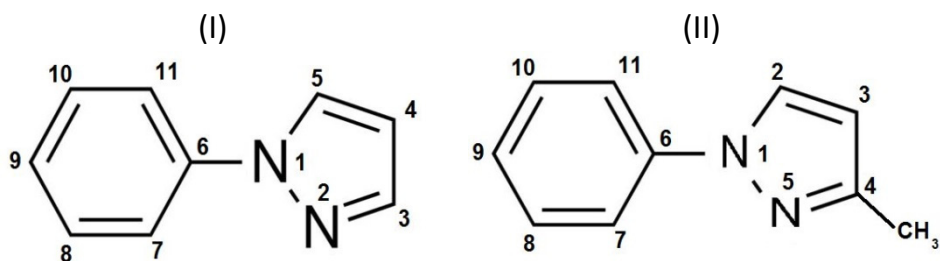


**Fig. 1.** Schematic structure of (I) 1-phenyl-pyrazole and (II) 4-Me-1-phenyl-pyrazole.

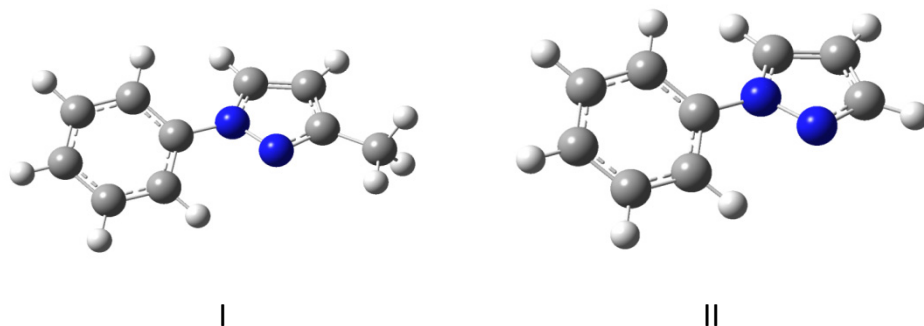


**Fig. 2.** Optimized geometry of (I) 1-phenyl-pyrazole and (II) 4-Me-1-phenyl-pyrazole compounds.

Krishnakumar et al. [12] have recorded the IR and Raman spectra of pyrazole and 3,5-dimethyl pyrazole and assigned the bands based on density functional calculations. In the present study, a detailed assignment of the vibrational modes of two other pyrazole derivatives based on the results of DFT calculations is given. The infrared (IR) and Raman spectra of the 1-phenyl-pyrazole and 4-Me-1-phenyl-pyrazole molecules in the spectral range  $400 - 3400 \text{ cm}^{-1}$  are displayed in **Fig. 3**.

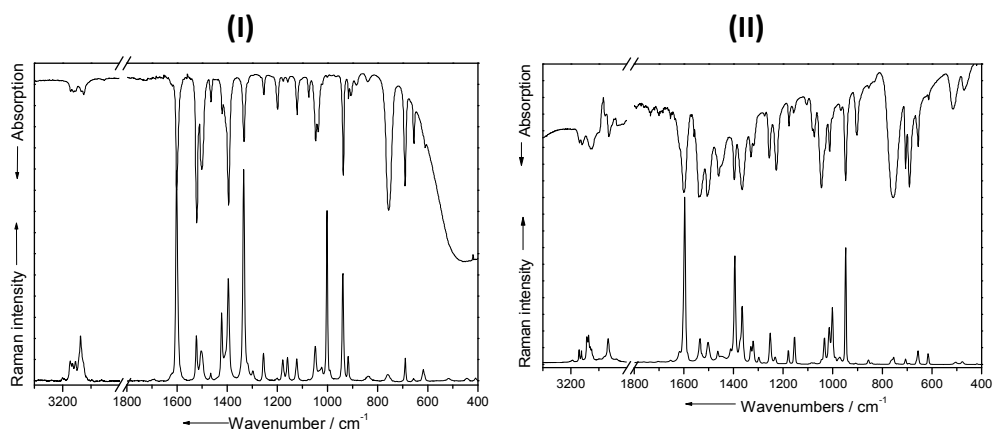


**Fig. 3.** FT-Raman and IR spectra of the (I) 1-phenyl-pyrazole and (II) 4-Me-1-phenyl-pyrazole molecules.

The assignment of the bands, which is summarized in **Tables 1** and **2**, is based on the visual inspection of normal mode displacement vectors by taking into account the vibrational bands' position and intensity. By comparing the calculated unscaled vibrational wavenumbers (not shown here) with the experimental results, we observed that, similar to previous studies [13, 12], the computed data using B3LYP method are larger than those calculated with BPW91 method.

The disagreement between theory and experimental results is a consequence of the anharmonicity and the general tendency of the quantum mechanical methods to overestimate the force constants at the exact equilibrium geometry [14]. It should be also mentioned that, the theoretical simulations were performed for the gas phase, while the experimental data were obtained from a liquid sample. In order to reduce the overall deviation between the unscaled and observed frequencies, scale factors are applied. The shown B3LYP values (Table 1 and 2) have been scaled by a factor of 0.963 as suggested by Rauhut and Pulay [14].

**Table 1.** Assignment of the theoretical wavenumber values ( $\text{cm}^{-1}$ ) to the experimental bands of 1-phenyl-pyrazole molecule.

IR	Raman	BPW91/ 6-311+G*	B3LYP/ 6-311+G*	Vibrational assignment
	277m	270	270	ring 1 +2 out-of-plane def.
	366m	357	352	C <sub>7, 6, 11</sub> + C <sub>5</sub> N <sub>1, 2</sub> bend.
	409w 446w 517w	399 434 505	402 429 505	ring 2 out-of-plane def.
611m	617m	611	609	ring 1 out-of-plane def. + C <sub>6, 7, 8</sub> + C <sub>9, 10, 11</sub> bend.
655m	650sh 657w	648	644	ring 1 out-of-plane def.
690s	690m	683	678	C <sub>8, 9, 10</sub> + C <sub>11, 6, 7</sub> bend.
756s	759mw	740	740	CH wagg (ring 2)
837mw 884mw	839mw	841 878	852 883	CH twist (ring 1 + 2)

906m		903	899	C <sub>3,4,5</sub> bend.
917m	917m	924	918	C <sub>5</sub> N <sub>1,2</sub> bend.
936s	938s	951	956	CH twist (ring 2)
1000vw	990sh 1001s	998 1014	979 1002	trigonal ring 2 str. ring 2 breathing
1020sh 1038m	1023m 1028sh	1029	1019	CH rock (ring 2)
1047m	1048m	1038	1024	CH bend. (ring 1)
1073m	1075vw	1075	1061	CH bend. (ring 2)
1121m	1111sh 1122m	1114	1099	ring 1 breathing
1159w 1176w	1159m 1178m	1157 1170	1142 1158	CH bend. (ring 2)
1198m	1200w	1187	1179	CH rock (ring 1)
1253m	1255m	1233	1227	C <sub>6</sub> N <sub>1</sub> C <sub>5</sub> bend.
1297vw	1298w	1314	1311	CH rock (ring 2)
1315sh	1318sh	1326	1315	N <sub>2</sub> C <sub>3</sub> + N <sub>1</sub> C <sub>5</sub> str.
1333m	1334s	1348	1291	C <sub>7,8</sub> + C <sub>9,10</sub> + C <sub>11,6</sub> str.
1394s	1396s	1398	1378	N <sub>2</sub> C <sub>3,4</sub> + C <sub>3,4,5</sub> str.
1421m	1422m 1435sh	1410	1397	N <sub>1</sub> C <sub>5,4</sub> str.
1465m	1465w	1455	1443	C <sub>7,8</sub> + C <sub>10,11</sub> str. + CH bend. (ring 2)
1502s	1504m	1492	1480	C <sub>8,9,10</sub> + C <sub>11,6,7</sub> str.
1522s	1523m	1512	1500	C <sub>4,5</sub> + C <sub>3</sub> N <sub>2</sub> + N <sub>1</sub> C <sub>6</sub> str.
1572sh 1601s 1619sh	1586sh 1602s 1620sh	1592 1602	1575 1585	C <sub>6,7</sub> + C <sub>9,10</sub> str. C <sub>7,8</sub> + C <sub>10,11</sub> str.
3051m 3071sh	3057sh 3073m	3100 3122	3049 3070	CH as. str. (ring 2)
3106m	3108m	3130	3078	CH s. str. (ring 2)
3123m 3143m	3129m 3146m	3169 3188	3114 3134	CH as. Str. (ring 1)
	3202w	3207	3153	CH s. str. (ring 1)

**Abbreviations:** ring 1 = pyrazole ring, ring 2 =phenyl ring, w=weak, m=medium, s=strong, sh=shoulder, stretch=stretching, bend=bending, twist=twisting, wag=wagging, rock=rocking, sym.=symmetric, as.=asymmetric. B3LYP values have been scaled by a factor of 0.963.

**Table 2.** Assignment of the theoretical wavenumber values ( $\text{cm}^{-1}$ ) to the experimental bands of 4-Me-1-phenyl-pyrazole molecule.

IR	Raman	BPW91/ 6-311+G*	B3LYP/ 6-311+G*	Vibrational assignment
	239m	228	227	ring 1 + 2 out-of-plane def.
	306m 322m	271 317	275 314	ring 1 out-of-plane def.
	368mw	355	351	$C_{7,6,11} + N_{5,1}C_2$ bend.
	419vw	399	401	ring 2 out-of-plane def.
470m	477w	454	450	ring 1 + 2 out-of-plane def.
503sh 514m	503w	508	507	ring 2 out-of-plane def.
613w	615m	615	612	ring 1 out-of-plane def. + $C_{6,7,8} + C_{9,10,11}$ bend.
655m	655m	652	649	ring 1 out-of-plane def. + $C_{4,12}$ str.
690s	691vw	698	691	$C_{7,6,11} + C_{8,9,10} + C_{2,3,4}$ bend.
705s	706mw	713	721	CH wag (ring 1)
756s	754m 758sh	738	738	CH wag (ring 2)
831vw 853w 901ms	843w 856mw 907vw	806 875 926	815 880 929	CH twist (ring 2)
947s	947s	938	932	$N_{5,1}C_2$ bend.
965w	972m	956	948	CH rock (ring 1) + CH twist ( $CH_3$ )
1000sh	988sh 1001m	988 1003	978 996	trigonal ring 2 str. $C_{3,4}N_5$ bend
1011m	1014m	1023	1010	ring 2 breathing
1031sh 1044s	1033m 1044sh	1033 1035	1026 1029	CH twist ( $CH_3$ ) + CH bend. (ring 1) + $N_{1,2}$ str.
1073m	1073vw	1072	1061	CH bend. (ring 1) + $N_1C_6$ str.
1082sh 1157mw 1176m	1086vw 1153m 1179m	1077 1156 1171	1065 1141 1158	CH bend. (ring 2)
1227s	1232m	1208	1199	CH rock (ring 1) + $N_{1,2}$ str.
1256ms	1252m	1235	1225	$C_6N_1C_2$ str. + CH rock (ring 1)
1317m	1320m	1314	1312	CH rock (ring 2)
1330m	1329m	1347	1291	$C_{6,7} + C_{8,9} + C_{10,11}$ str.

1366s	1364m 1372sh	1363 1373	1347 1361	CH wag (CH <sub>3</sub> ) C <sub>2,3</sub> + N <sub>5</sub> C <sub>4</sub> str.
1396s	1395s 1411sh	1391	1381	C <sub>4,12</sub> str. + CH wag (CH <sub>3</sub> ) + CH rock (ring 2)
1451sh	1450w	1446	1431	C <sub>2,3,4</sub> str. + CH bend. (CH <sub>3</sub> ) + CH rock (ring 2)
1458s	1463m	1459	1445	CH bend. (CH <sub>3</sub> )
1506s	1502m	1494	1481	C <sub>6</sub> N <sub>1</sub> + C <sub>8,9,10</sub> str.
1533s 1539s	1527sh 1534m	1532	1522	C <sub>2,3</sub> + C <sub>4,12</sub> str. + CH bend (CH <sub>3</sub> )
1599s 1617sh	1596s 1617sh	1591 1602	1574 1585	C <sub>6,7</sub> + C <sub>9,10</sub> str. C <sub>7,8</sub> + C <sub>10,11</sub> str.
2928m 3049m	2933m 3051sh	2972 3099	2920 3048	CH str. (CH <sub>3</sub> )
	3072m 3085m	3129 3153	3077 3102	CH str. (ring 2)
3119m 3137m	3123m 3140m	3176 3203	3122 3149	CH str. (ring 1)

**Abbreviations:** ring 1 = pyrazole ring, ring 2 = phenyl ring. ring 1 = pyrazole ring, ring 2 = phenyl ring, w=weak, m=medium, s=strong, sh=shoulder, stretch=stretching, bend=bending, twist=twisting, wag=wagging, rock=rocking, sym.=symmetric, as.=asymmetric. B3LYP values have been scaled by a factor of 0.963.

By analyzing **Fig. 3**, **Table 1** and **Table 2** it can be seen that the bands given by CH stretching in phenyl and pyrazole ring dominate the high wavenumber region (3200 – 2800 cm<sup>-1</sup>) of the IR and Raman spectra of both compounds. Moreover, in the case of 4-Me-1-phenyl-pyrazole, the CH stretching in methyl groups leads to the appearance of two Raman and IR bands located around 2930 and 3050 cm<sup>-1</sup>.

The stretching vibrations of the phenyl ring give rise to bands present in the range between 1620 and 1570 cm<sup>-1</sup> of all spectra. Furthermore, the strong Raman and IR bands around 1330 cm<sup>-1</sup> were attributed to the CC stretching vibrations of the same ring. The breathing vibration of phenyl structure gives rise to the medium intense IR and Raman bands at 1000 cm<sup>-1</sup> for

the first compound and at  $1010\text{ cm}^{-1}$  for the second compound, respectively. The Raman bands that occur around  $410 - 520\text{ cm}^{-1}$  are due to the out-of-plane deformation vibrations of the same structure.

Regarding the pyrazole ring, its stretching vibrations appear at about  $1422$  and  $1396\text{ cm}^{-1}$  in the spectra of compound I and at around  $1450$  and  $1364\text{ cm}^{-1}$  in the compound II spectra. In the case of the first compound, the Raman and IR bands around  $1120\text{ cm}^{-1}$  were ascribed to the breathing vibration, while the ones at  $650\text{ cm}^{-1}$  may be attributed to the out-of-plane deformation of the pyrazole ring. For the second compound, Raman bands that are due to the out-of-plane deformation occur around  $306-320\text{ cm}^{-1}$ . The medium intense Raman and IR bands around  $1255\text{ cm}^{-1}$  were attributed to the CNC bending vibration of the 1-phenyl-pyrazole molecule, while in the case of 4-Me-1-phenyl-pyrazole, at the same wavenumber, a band due to the stretching vibration of the same group appears.

## CONCLUSIONS

Two types of pyrazole derivatives, 1-phenyl-pyrazole and 4-Me-1-phenyl-pyrazole, were investigated in detailed from both an experimental and a theoretical point of view by using Raman and IR spectroscopy in combination with theoretical calculations based on DFT simulations. The first step in the theoretical approach was the finding of the optimized compound's geometry and after that the obtaining of the theoretical wavenumbers by involving different correlation functional (BPW91 and B3LYP) throughout the theoretical simulations. A relatively good agreement between the experimental and obtained theoretical data was achieved.

## REFERENCES

- [1] Y.A. Ivanenkov, K.V. Balakin and S.E. Tkachenko, *Drugs R D.* **9(6)**, 397 (2008).
- [2] M.J. Graneto et al., *J. Med. Chem.* **50(23)**, 5712 (2007).
- [3] P.E. Almeida da Silva et al., *Int. J. Antimicrob. Agents* **32(2)**, 139 (2008).

- [4] N. Singh, N.K. Sangwan and K.S. Dhindsa, *Pest Manag. Sci.* **56(3)**, 284 (2000).
- [5] K.A. Rowberg, M. Even, E. Martin and A.J. Hopfinger, *J. Agric. Food Chem.* **42(2)**, 374 (1994).
- [6] J.H.H. Eussen, J.L.G. Thus, K. Wellinga and B. Stork, *Pestic. Sci.* **29**, 101 (1990).
- [7] G. Dryhurst, *J. Electrochem. Soc.* **124**, 390 (1977).
- [8] M.J. Frisch, et al., Gaussian 98, Revision A7; Gaussian Inc.: Pittsburgh, PA, 1998.
- [9] A.D. Becke, *Phys. Rev.* **A38**, 3098 (1988).
- [10] J.P. Perdew and Y. Wang, *Phys. Rev.* **B45**, 13244 (1992).
- [11] A.D. Becke, *Chem. Phys.* **98**, 1372 (1993).
- [12] V. Krishnakumara, N. Jayamani and R. Mathammal, *Spectrochim. Acta A* **79**, 1959 (2011).
- [13] M. Baia, L. Baia, W. Kiefer and J. Popp, *J. Phys. Chem. B* **108**, 17491 (2004).
- [14] G. Rauhut and P. Pulay, *J. Phys. Chem.* **99**, 3093 (1995).

## NEW INDIUM-BASED OXIDE WITH OXYGEN-DEFICIENT FLUORITE-TYPE STRUCTURE: $\text{In}_{5.5}\text{Sn}_{0.5}\text{Sb}_{0.5}\text{Te}_{0.5}\text{O}_{12}$

LILIANA BIZO<sup>a</sup>

**ABSTRACT.** A new composition containing the entire series of  $4d^{10}$  cations,  $\text{In}^{3+}$ ,  $\text{Sn}^{4+}$ ,  $\text{Sb}^{5+}$  and  $\text{Te}^{6+}$ ,  $\text{In}_{5.5}\text{Sn}_{0.5}\text{Sb}_{0.5}\text{Te}_{0.5}\text{O}_{12}$ , which exhibits an ordered oxygen-deficient fluorite-type structure, has been synthesized by solid state reactions in air. The latter was studied from point of view of structural, optical and electrical properties and compared with  $\text{In}_6\text{TeO}_{12}$  and  $\text{In}_5\text{SnSbO}_{12}$ , previously reported. The structural results show an cation ordering of  $\text{Sb}^{5+}/\text{Te}^{6+}$  and  $\text{In}^{3+}/\text{Sn}^{4+}$  species on both octahedral and seven fold coordinated sites, respectively. Moreover the electrical conductivity of this new oxide, is enhanced by less than one order of magnitude with respect to  $\text{In}_4\text{Sn}_3\text{O}_{12}$  and it turns to a semi-metallic behavior in contrast to  $\text{In}_4\text{Sn}_3\text{O}_{12}$  which is a semi-conductor.

**Keywords:** transparent conducting oxides, oxygen-deficient fluorite-type structure, X-ray diffraction, Rietveld refinement, optical properties, electrical properties.

### INTRODUCTION

Transparent conducting oxides (TCOs) are important materials in the field of optoelectronics for various devices such as solar cells, liquid crystal displays, flat screen high definition televisions, high resolution screens of portable computers, thin film photovoltaics and electrochromic windows [1-4].

---

<sup>a</sup> Babes-Bolyai University, Faculty of Chemistry and Chemical Engineering, 11 Arany Janos str., 400028 Cluj-Napoca, Romania, lbizo@chem.ubbcluj.ro

Due to numerous applications, many investigations have been carried out recently in order to discover new n-type [5] or p-type [6] transparent conductors. Generally TCOs are predominantly n-type due to the ease of forming cation interstitials or oxygen vacancies [7]. Besides the most famous indium tin doped oxide  $\text{In}_2\text{O}_3\cdot\text{Sn}$  [8, 9], known as ITO, which crystallizes with the bixbyite structure, another oxide was identified for the composition  $\text{In}_4\text{Sn}_3\text{O}_{12}$  [10,11]. Electrical and optical properties of the latter, prepared in the form of thin films [12] were found to be very interesting, with characteristics close to ITO. The synthesis of solid solution  $\text{In}_{4+x}\text{Sn}_{3-2x}\text{Sb}_x\text{O}_{12}$  [13] by substitution of pair Sb(V)-In(III) for Sn(IV) demonstrate that introduction of antimony increase the electronic conductivity up to one order of magnitude with respect to  $\text{In}_4\text{Sn}_3\text{O}_{12}$ . Moreover Sb(V) shows a great ability to form  $\text{M}_7\text{O}_{12}$  ordered oxygen-deficient fluorite structure. On the other hand the introduction of another  $4d^{10}$  cation in the form of reported mixed tellurate  $\text{In}_6\text{TeO}_{12}$  [14], results in a increase of the cationic ordering on both sites, octahedral and seven-fold coordinated, respectively. Taking into account all of these, we successfully prepared a new composition which contain entire series of  $4d^{10}$  cations,  $\text{In}^{3+}$ ,  $\text{Sn}^{4+}$ ,  $\text{Sb}^{5+}$  and  $\text{Te}^{6+}$ , previously not reported. In the present paper structural, optical and electrical properties of the  $\text{In}_{5.5}\text{Sn}_{0.5}\text{Sb}_{0.5}\text{Te}_{0.5}\text{O}_{12}$  complex oxide were investigated in order to evaluate his potential as TCOs.

## EXPERIMENTAL

The studied composition,  $\text{In}_{5.5}\text{Sn}_{0.5}\text{Sb}_{0.5}\text{Te}_{0.5}\text{O}_{12}$  and  $\text{In}_4\text{Sn}_3\text{O}_{12}$ ,  $\text{In}_5\text{SnSbO}_{12}$  and  $\text{In}_6\text{TeO}_{12}$  for comparison were prepared by solid state reactions from mixtures of pure  $\text{In}_2\text{O}_3$ ,  $\text{SnO}_2$ ,  $\text{TeO}_2$  and  $\text{Sb}_2\text{O}_3$  in alumina crucibles heated in air. In the case of  $\text{In}_{5.5}\text{Sn}_{0.5}\text{Sb}_{0.5}\text{Te}_{0.5}\text{O}_{12}$  compositions the mixtures were initial heated at at 600 °C in order to ensure the full oxidation of Sb(III) into Sb(V) and than successive 12h annealings followed by air quenching were performed up to 1300 °C. After each annealing step, air quenching and regrinding was performed. The preparation of the other oxides was previously reported [13, 14]. Laboratory XRPD data for phase identification and Rietveld refinement were collected

using a Panalytical X'Pert diffractometer (CoKa1 radiation) equipped with an X'Celerator detector. The XRPD data were refined with the Fullprof programme [15]. Diffuse reflectance measurements were carried out using a double beam Cary Varian 100 Spectrofotometer in the range 190-900 nm with a scan rate of 600 nm/min. Resistivity data were measured with the four probe method on pellets sintered in air at 1300 °C using a PPMS (Physical Properties Measurements System) device.

## RESULTS AND DISCUSSION

### X-ray powder diffraction (XRPD)

Structure calculations of  $\text{In}_{5.5}\text{Sn}_{0.5}\text{Sb}_{0.5}\text{Te}_{0.5}\text{O}_{12}$  composition have been performed by Rietveld analysis of the XRPD data. The structural model of  $\text{In}_4\text{Sn}_3\text{O}_{12}$  was used [16], S.G.  $R\bar{3}$  with two sets of cationic positions 3(a) and 18(f) and two sets of oxygen positions 18(f), in the corresponding hexagonal cell. The calculated pattern fit with the experimental one, as shown in Figure 1. The structural results of  $\text{In}_{5.5}\text{Sn}_{0.5}\text{Sb}_{0.5}\text{Te}_{0.5}\text{O}_{12}$  composition, including cell parameters, atomic positions and cations distributions and our previous results obtained from Time of Flight Neutron Powder Diffraction (TOF NPD) for  $\text{In}_5\text{SnSbO}_{12}$  [14] and XRPD for  $\text{In}_6\text{TeO}_{12}$  [14] Rietveld analysis for comparison, are presented in Table 1.

The best structure calculations always correspond to total preferential localization of tellurium in octahedral 3(a) site, and cation which accompany  $\text{Te}^{6+}$  in this site is  $\text{Sb}^{5+}$ . This tendency of  $\text{Sb}^{5+}$  to accommodate a highly symmetrical octahedral coordination was previously observed [17]. The smaller sizes of  $\text{Sb}^{5+}$  (0.60 Å) and  $\text{Te}^{6+}$  (0.56 Å) compared to  $\text{In}^{3+}$  (0.80 Å) and  $\text{Sn}^{4+}$  (0.69 Å) are in agreement with this view point [18]. As expected on the basis of its larger size,  $\text{In}^{3+}$  occupies the distorted sevenfold coordinated site 18(f). The values of positional coordinates are very similar. The values of isotropic displacement parameter of  $\text{In}_{5.5}\text{Sn}_{0.5}\text{Sb}_{0.5}\text{Te}_{0.5}\text{O}_{12}$  composition are larger if compare to  $\text{In}_4\text{Sn}_3\text{O}_{12}$  and  $\text{In}_5\text{SnSbO}_{12}$ , this being a consequence of the introduction of  $\text{Te}^{6+}$  cations.

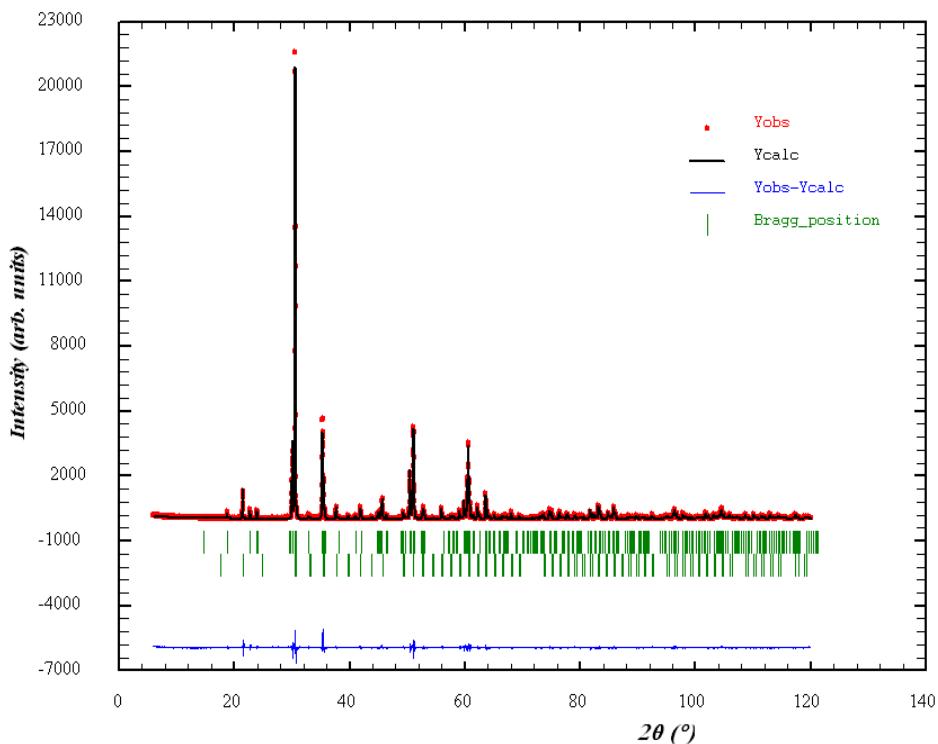


**Fig. 1.** Observed (dots), calculated (lines) and difference XRPD pattern of  $\text{In}_{5.5}\text{Sn}_{0.5}\text{Sb}_{0.5}\text{Te}_{0.5}\text{O}_{12}$  treated at  $1300^\circ\text{C}$ . Vertical bars indicate the positions of the reflections of the title phase (upper) and  $\text{In}_2\text{O}_3$  (lower).

**Table 1.** Atomic parameters of the composition  $\text{In}_{5.5}\text{Sn}_{0.5}\text{Sb}_{0.5}\text{Te}_{0.5}\text{O}_{12}$  and  $\text{In}_6\text{TeO}_{12}$  [14] –SG  $\bar{R}3$  from Rietveld refinement of XRPD data and for comparison TOF NPD data for  $\text{In}_5\text{SnSbO}_{12}$  [14].

Formula	$\text{In}_6\text{TeO}_{12}$ [14]	$\text{In}_{5.5}\text{Sn}_{0.5}\text{Sb}_{0.5}\text{Te}_{0.5}\text{O}_{12}$	$\text{In}_5\text{SnSbO}_{12}$ [14]
Hex. Cell			
$a_h$ (Å)	9.4407(2)	9.4494(5)	9.4479(1)
$c_h$ (Å)	8.9943(3)	8.9121(3)	8.9035(1)
Cationic site 3(a)			
$B$ (Å) <sup>2</sup>	0.19(7)	0.60(5)	0.41(11)

Formula	$\text{In}_6\text{TeO}_{12}$ [14]	$\text{In}_{5.5}\text{Sn}_{0.5}\text{Sb}_{0.5}\text{Te}_{0.5}\text{O}_{12}$	$\text{In}_5\text{SnSbO}_{12}$ [14]
Cationic site 18(f)			
x	0.2507(3)	0.2519(8)	0.2520(4)
y	0.2144(2)	0.2147(8)	0.2149940
z	0.3545(2)	0.3516(2)	0.3519(4)
$B(\text{\AA})^2$	0.43(3)	0.51(4)	0.40(6)
O <sub>1</sub> site 18(f)			
x	0.1825(18)	0.1865(8)	0.1907(4)
y	0.1520(28)	0.1597(0)	0.1664(4)
z	0.1178(17)	0.1138(7)	0.1171(4)
$B(\text{\AA})^2$	0.43(3)	2.48(2)	0.84(7)
O <sub>2</sub> site 18(f)			
x	0.2000(24)	0.19637	0.1938(4)
y	0.9823(24)	0.98141	0.9759(4)
z	0.3925(17)	0.39064	0.3945(4)
$B(\text{\AA})^2$	0.9(3)	1.48(7)	0.63(6)
Reliability factors			
R <sub>b</sub> %	3.8	3.79	3.2
R <sub>p</sub> %	10.2	10.4	9.7
R <sub>wp</sub> %	13.9	14.2	8.3

Of course, is very difficult to determine the cationic distribution in this type of structure since all the  $4d^{10}$  cations involved are isoelectronic.

As previously reported,  $\text{In}_6\text{TeO}_{12}$  cannot be prepared as a pure phase [14], the calculated amount of extra phase ( $\text{In}_2\text{O}_3$ ) is around of 13 wt%. For  $\text{In}_{5.5}\text{Sn}_{0.5}\text{Sb}_{0.5}\text{Te}_{0.5}\text{O}_{12}$  the calculated amount of the secondary bixbyite phase from Rietveld refinement is 8 wt%.

### Optical measurements

Diffuse reflectance spectra of  $\text{In}_{5.5}\text{Sn}_{0.5}\text{Sb}_{0.5}\text{Te}_{0.5}\text{O}_{12}$  and compared with  $\text{In}_4\text{Sn}_3\text{O}_{12}$ , and  $\text{In}_5\text{SnSbO}_{12}$  are presented in Figure 2. The spectra is shifted towards the larger energies. The introduction of  $\text{Te}^{6+}$  in the presence of  $\text{Sn}^{4+}$  and  $\text{Sb}^{5+}$  increase the maximum percent reflectance around 500 nm by around 20% with respect to  $\text{In}_4\text{Sn}_3\text{O}_{12}$ . Simultaneously, a increase of the optical bandgap by approximately 0.12 eV occurs.

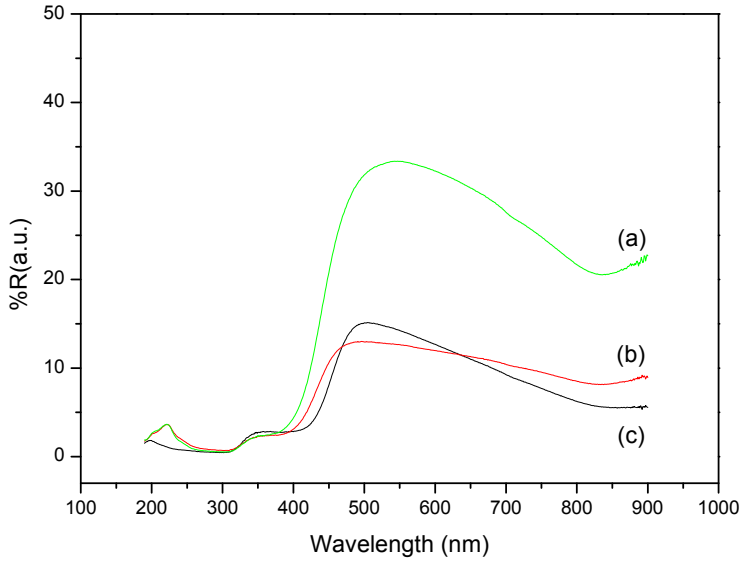


**Fig. 2.** Measured optical reflectance of  $\text{In}_{5.5}\text{Sn}_{0.5}\text{Sb}_{0.5}\text{Te}_{0.5}\text{O}_{12}$  (a),  $\text{In}_5\text{SnSbO}_{12}$  (b) and  $\text{In}_4\text{Sn}_3\text{O}_{12}$  (c).

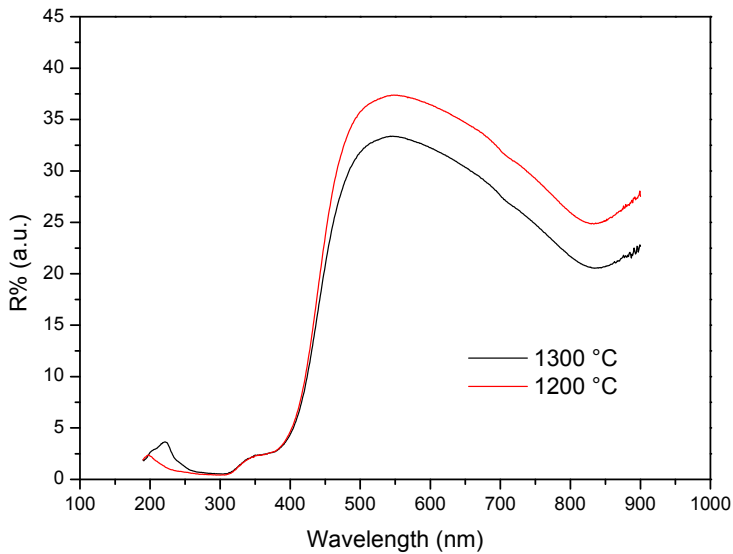


**Fig. 3.** Measured optical reflectance in the composition  $\text{In}_{5.5}\text{Sn}_{0.5}\text{Sb}_{0.5}\text{Te}_{0.5}\text{O}_{12}$  after 1200 °C and 1300 °C, respectively.

Regarding the influence of temperature on optical properties,  $\text{In}_{5.5}\text{Sn}_{0.5}\text{Sb}_{0.5}\text{Te}_{0.5}\text{O}_{12}$  sample was measured after two heating treatments, 1200 °C and 1300 °C, respectively. As visible from Figure 3, the maximum percent reflectance is lowered by 5 %. Increasing temperature from 1200 °C to 1300 °C does not induce strong modifications on the optical properties.

### Electrical measurements

Figure 4 includes the  $\rho = f(T)$  curves of the  $\text{In}_{5.5}\text{Sn}_{0.5}\text{Sb}_{0.5}\text{Te}_{0.5}\text{O}_{12}$ , composition and for reference  $\text{In}_4\text{Sn}_3\text{O}_{12}$  and  $\text{In}_5\text{SnSbO}_{12}$  samples, prepared in the same conditions. It should be mentioned that  $\text{In}_{5.5}\text{Sn}_{0.5}\text{Sb}_{0.5}\text{Te}_{0.5}\text{O}_{12}$  pellets for electrical measurement are sintered at 1300 °C instead of 1400 °C due to the instability of the  $\text{M}_7\text{O}_{12}$  phase and its transformation into bixbyite  $\text{In}_2\text{O}_3$  as deduced from structure calculation.

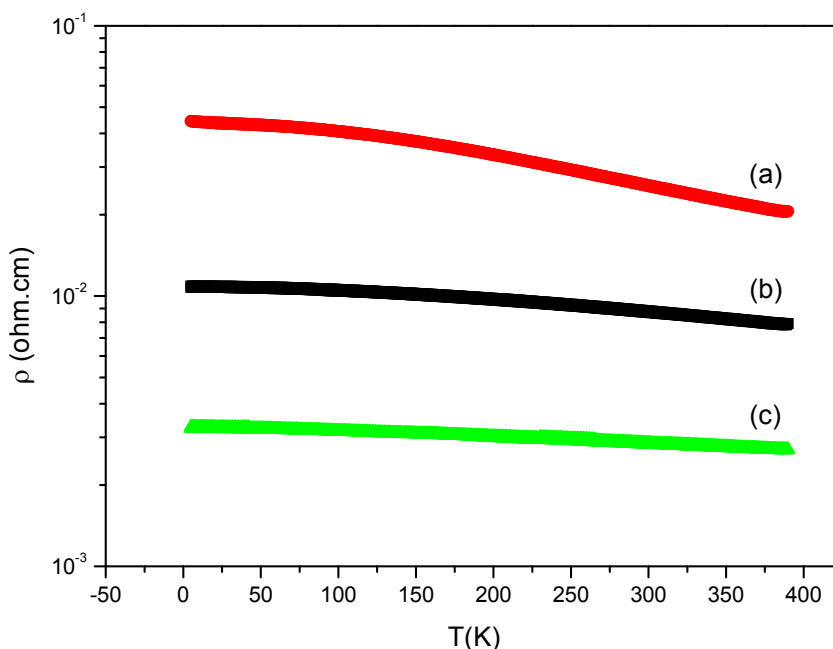


**Fig. 4.** Electrical resistivity ( $\Omega\cdot\text{cm}$ ) versus temperature (K) in  $\text{In}_4\text{Sn}_3\text{O}_{12}$  (a),  $\text{In}_{5.5}\text{Sn}_{0.5}\text{Sb}_{0.5}\text{Te}_{0.5}\text{O}_{12}$  (b) and  $\text{In}_5\text{SnSbO}_{12}$  (c).

The  $\rho = f(T)$  clearly show the increase of resistivity due to introduction of tellurium. If compare with  $\text{In}_4\text{Sn}_3\text{O}_{12}$  which exhibits a room temperature resistivity of  $2.6 \times 10^{-2} \Omega\cdot\text{cm}$  [13], there is clearly decrease of resistivity in the case of  $\text{In}_{5.5}\text{Sn}_{0.5}\text{Sb}_{0.5}\text{Te}_{0.5}\text{O}_{12}$ , about half an order of magnitude ( $\rho = 8.8 \times 10^{-3} \Omega\cdot\text{cm}$ ). Thus, the resistivity of the new oxide is half an order of magnitude smaller than that of  $\text{In}_4\text{Sn}_3\text{O}_{12}$  and less than one order of magnitude larger than that of the  $\text{In}_5\text{SnSbO}_{12}$  ( $2.8 \times 10^{-3} \Omega\cdot\text{cm}$ ) [13]. This value of resistivity obtained in the case of new oxide  $\text{In}_{5.5}\text{Sn}_{0.5}\text{Sb}_{0.5}\text{Te}_{0.5}\text{O}_{12}$  is also comparable with ceramic ITO samples (3% Sn) prepared at  $1400^\circ\text{C}$  [19]. Moreover, the temperature dependence of  $\text{In}_4\text{Sn}_3\text{O}_{12}$  is practically semi-conducting instead of semi-metallic in the case of  $\text{In}_{5.5}\text{Sn}_{0.5}\text{Sb}_{0.5}\text{Te}_{0.5}\text{O}_{12}$  and  $\text{In}_5\text{SnSbO}_{12}$ .

## CONCLUSIONS

In conclusion we shown the opportunity to bring together the entire series of  $4d^{10}$  -type cations,  $\text{In}^{3+}$ ,  $\text{Sn}^{4+}$ ,  $\text{Sb}^{5+}$  and  $\text{Te}^{6+}$ , in the form of complex oxide  $\text{In}_{5.5}\text{Sn}_{0.5}\text{Sb}_{0.5}\text{Te}_{0.5}\text{O}_{12}$ . The latter was prepared by solid state reactions and studied from point of view of structural, optical and electrical properties. The structure calculation from XRPD data shows an ordered distribution of  $\text{In}^{3+}$ ,  $\text{Sn}^{4+}$ ,  $\text{Sb}^{5+}$  and  $\text{Te}^{6+}$  cations between the octahedral and seven-fold coordinated sites, respectively. The maximum reflectance around 500 nm is increased by approximately 20% with respect to  $\text{In}_4\text{Sn}_3\text{O}_{12}$ . The optical band gap is shifted to lower energies, i.e. higher wavelengths. A decrease of electrical resistivity by less than one order of magnitude if compare with  $\text{In}_4\text{Sn}_3\text{O}_{12}$  occurs.

## REFERENCES

1. H. Hosono, *Thin Solid Films*, 515 6000 (2007).
2. D. S. Ginley, C. Bright, *MRS Bulletin*, 8, 15 (2000).
3. B. G. Lewis, D. C. Paine, *MRS Bulletin*, 8, 22 (2000).

4. H. L. Hartnagel, A. L. Dawar, A. K. Jain, C. Jagdish, "Semi-Conducting Transparent Thin Films", I O P publishing, Bristol and Philadelphia, 1995.
5. A. J. Freeman, K. R. Poeppelmeier, T. O. Mason, R. P. H. Chang, T. J. Marks, *MRS Bulletin*, 8, 45 (2000).
6. H. Kawazoe, H. Yanagi, K. Ueda and H. Hosono, *MRS Bulletin*, 8, 28 (2000).
7. S. Lany, A. Zunger, *Physical Review Letters* 98, 045501 (2007).
8. G. Frank and H. Köstlin, *Appl. Phys. Solids Surf.* 27, 197 (1982).
9. R. B. H. Tahar, T. Ban, Y. Ohya and Y. Takahashi, *J. Appl. Phys.* 83, 2631 (1998).
10. J. L. Bates, C. W. Griffin, D. D. Marchant and J. E. Garnier, *Amer. Ceram. Soc. Bull.*, 65, 673 (1986).
11. H. Enoki and J. Echigoya, *Phys. Status Solidi*, 132A, 151, (1992).
12. T. Minami, Y. Takeda, S. Takata and T. Kakumumi, *Thin Solid Films*, 308, 13 (1997).
13. J. Choisnet, L. Bizo, R. Retoux, B. Raveau, *J. of Solid State Chem.*, 177, 3748 (2004).
14. J. Choisnet, L. Bizo, M. Allix, M. Rosseinsky, B. Raveau, *J. of Solid State Chem.*, 180 1002 (2007).
15. J. Rodriguez-Carvajal, Program Fullprof 3.5, (1997)
16. N. Nadaud, N. Lequeux, M. Nanot, J. Jové, T. Roisnel, *J. Solid State Chem.* 135, 140 (1998).
17. J. Choisnet, P. Mouron, *Mater. Res. Bull.*, 22, 1355 (1989).
18. R. D. Shannon and C. T. Prewitt, *Acta Cryst.* 25B, 925, (1969).
19. A. Ambrosini, A. Duarte, K.R. Poeppelmeier, M. Lane, C.N. Kannewurf, T.O. Mason *J. Solid State Chemistry*, 153, 41 (2000).



## EDUCATION AND TRAINING IN NUCLEAR SCIENCES: FIRST STEPS TOWARDS EUROPEAN INTEGRATION

D. CIURCHEA<sup>a,\*</sup>, O. COMȘA<sup>b</sup> and C. COSMA<sup>c</sup>

**ABSTRACT.** We summarize a timeline of the European integration efforts in the nuclear sciences education and training in Romania.

**Keywords:** *ECVET, EQF, E&T, nuclear sciences, nuclear engineering.*

### INTRODUCTION: The ECVET system

At the moment of this writing, the most important challenge for the educational system in Europe consists in application of the ECVET system [1]. The jobs in EU are listed while providing for each: job description, knowledge, skills and the competences (KSC). For every KSC item the EQF [2] level should be specified. The competences are of cognitive type, not to be confused with the learning outcomes (LO). This system known as “the Copenhagen process” by stressing the development of skills and continues the former “Bologna process” in which only the knowledge was addressed [3]. The EQF levels 6-8 correspond roughly to the BA, MD and PhD respectively [3]. A sample is given in Table 1.

In the nuclear power field, a number of 150 jobs were identified, yielding reference to the European education and training (E&T) system in nuclear sciences [4].

---

<sup>a</sup> Faculty of Physics, “Babes-Bolyai” University, 1 Kogalniceanu, 400054 Cluj-Napoca, Romania

<sup>b</sup> Center of Technology and Engineering for Nuclear Projects, 409 Atomistilor Street, Măgurele, Ilfov, Romania

<sup>c</sup> Faculty of Environmental Sciences and Engineering, “Babes-Bolyai” University, 30 Fantanele, 400294 Cluj-Napoca, Romania

\* Corresponding author: [dr.ciurchea@academic.ro](mailto:dr.ciurchea@academic.ro)

## 2. DEVELOPMENT OF EDUCATION AND TRAINING IN NUCLEAR SCIENCES IN ROMANIA

Nuclear technologies were the dream of Romanian scientists since the '50s in which the present authors. Since 1971, upon advice from the International Atomic Energy Agency, Romania made massive investments in CANDU type reactor, both research and technologies. Many stake-holders emerged, located mainly in Pitești, Bucharest, Râmnicu-Vâlcea, Drobeta-Turnu Severin, Cernavodă. Meanwhile the educational system remained framed by „knowledge“ pattern, so it is understandable that the stakeholders in the nuclear industry made a solution for developing skills and for specific training located first in Bucharest, within the Institute for Physics and Nuclear Engineering, while expressing explicit interest in all E&T activities. A timeline is given in Table 2.

**Table 1.** Example of ECVET file for a job profile drafted by the EU's Joint Research Centre, ref. [4].

	<b>JOB TITLE</b>	<b>OCCUPATIONAL CATEGORY</b>
1.3.18	OCCUPATIONAL SAFETY MANAGER	PROFESSIONAL
PHASE / AREA	<b>ALTERNATE JOB TITLE(S) – SPECIALISATIONS</b>	<b>FUNCTIONAL CATEGORY</b>
NPP N	----	MANAGEMENT
CONSTRUCTION		
<b>Role / Functions</b>		
Managing the safety and security department according to the regulatory authorities and plant procedures during construction.		
<ul style="list-style-type: none"> <li>• Perform the procedures of the Safety and Security department...</li> <li>• .....</li> </ul>		
<b>JOB REQUIREMENTS</b>		
<b>KNOWLEDGE (Cognitive competence)</b>		<b>EQF level (1-8)</b>
Safety and Security Management.		6
Security Systems, Applications and Concepts. (Security and safeguards, concept and application)		7
.....		

SKILLS (Technical and functional competence)	EQF level (1-8)
Specifying Safety and Security procedures content	5-6
Conduct assessment of risks in the workplace	5
.....	
COMPETENCE (Attitude; behavioural and personal competence)	EQF level (1-8)
Conscientiousness	6
Capacity to allocate tasks and organise work	5
Management of people	5
.....	

Accession of Romania to European Union obviously caught attention of the stakeholders, and therefore participation to both E&T and reserach includes industrial entities, regulatory bodies, reserch institutions and universities alltogether in national bodies and networks. A timeline is given in Table 3.

**Table 2.** Timeline of nuclear technology development in Romania, revised from ref. [5].

<p>1939 - Germans discover first Uranium ore deposits in Romania.</p> <p>1949 - Founding the Atomic Physics Institute as part of Romanian Academy.</p> <p>1956 - Atomic Physics Institute(Institutul de Fizica Atomica) is founded under the leadership of Horia Hulubei.</p> <p>1957 - Criticality of the Soviet VVRS research reactor(2MW) suplied by USSR.</p> <p>1970 - IAEA mission to guide the Romanian nuclear program.</p> <p>Founding "Uzina G" at Rm Valcea, a research facility to design the heavy water plant in Drobeta-Turnu Severin. Romania ratifies the Nonproliferation Treaty.</p> <p>1971 - Founding the "Institutul de Tehnologii Nucleare" from Pitesti - see ref. [6].</p> <p>1973 - Talks with AECLCanada for buying CANDU technology.</p> <p>1975 - The infrastructure of the platform in Pitesti is ready.</p> <p>1977 - Cooperation agreement between Canada and Romania for peaceful uses of atomic energy.</p> <p>1978 - Starting the "uzina R" for UO2 powder fabrication at Feldioara. The contracts with AECL Canada for the CANDU technology are signed.</p> <p>1979 - Starting the TRIGA reactor in Pitesti- Start new build of the The Cernavoda plant.</p>
--

1980 - Start of the nuclear fuel facility in Pitesti.  
1985 - In the spring of 1985 the fuel fabricated in Pitesti survived and behaved very well in a test in the Canadian NRU reactor. Even today the fuel burnt in the Cernavoda site is behaving very well.  
1988 - Starting the first heavy water module at the heavy water plant at ROMAG - Drobeta Turnu Severin.  
1996 - Starting the first reactor at Cernavoda.  
1998 - Founding "Societatii Nationale Nuclearelectrica" - reactor operations.  
Founding "Regia Autonoma pentru Activitati Nucleare" - fuel manufacturing, from ore to fuel bundle.  
2001 - Contract to finish the second reactor at Cernavoda which become operational in 2007.

**Table 3.** Timeline of institutional contacts between Romanian and European entities in the E&T in nuclear sciences.

1999 - CITON and later University „Politehnica“ of Bucharest join the European Nuclear Education Network (ENEN)  
2005 - The TENSP consortium [7] is formed. Description of the aims in refs [8-9].  
2006 - Romanian stakeholders join the Sustainable Nuclear Energy –Technological Platform (SNE-TP) [10] and EUTERP [11]  
2010 - The RONEN network is founded [12].  
2014-2015 - The Institute of Atomic Physics (IFA) along with the stakeholders in nuclear engineering join the prestigious EURATOM research framework. Before that date, only individual entities applied in these actions.  
Formation of a national ECVET network.

We cite only a few goals of this participation in E&T in nuclear sciences in the EURATOM project:

- Attracting and retaining students and junior scientists into the nuclear sciences, with emphasis on Radiation Protection
- Coordination and collaboration on E&T policy and strategy
- - European integration of junior scientist career development

## REFERENCES

1. ECVET=European Credit System for Educational Education and Training, <http://www.ecvet-team.eu/en/system/files/documents/13/ecvet-recommendation.pdf>; see also <http://www.ecvet-toolkit.eu/site/introduction/ecvethistoryandtimeline> and <http://www.ecvet-team.eu/en/ecvet-documentation>.
2. EQF=European Qualifications Framework, <http://www.ecvet-team.eu/en/european-qualification-framework-eqf> see also. In Romanian, [http://www.europass-ro.ro/pagina/cadrul\\_european\\_al\\_calificariilor](http://www.europass-ro.ro/pagina/cadrul_european_al_calificariilor).
3. G. van Goethem, Public address during launching the EURATOM call in Brussels, March 2014.
4. D. Ciurchea in "Towards the implementation of the European Credit System for Vocational Education and Training (ECVET) in the nuclear energy sector", report JRC85564(EUR 26443 EN), eds. Mihail Ceclan, César Chenel-Ramos, Petten, The Netherlands, 2014.
5. V. Andrei, I.C. Bilegan, F. Glodeanu, C. Racoveanu, „De la atom la kilowatt în România”, Modelsim, Bucharest, 2007, also in the TENSP archive at [7].
6. <http://www.nuclear.ro/en/history.php>.
7. <http://www.academic.ro/tensp>.
8. M. Ceclan, <http://www.euronuclear.org/e-news/e-news-11/romanian.htm>.
9. Mihail Ceclan, Ulrik Von Estorff, „The road map for ECVET implementation in the nuclear energy sector“, ECVET Magazine Nr.20, <http://www.ecvet-team.eu/en/system/files/documents/2485/ecvet-magazine-20-%E2%80%93june-2014.pdf>.
10. <http://www.sne-tp.eu>.
11. EUTERP=European Training and Education in Radioprotection, <http://www.euterp.eu/>
12. RONEN=Romanian Nuclear Education Network, <http://www.ronen.ro>.



## METHODS AND MODELS FOR CALCULATING NMR SPECTRA: LEVETIRACETAM AS A TEST CASE

RALUCA LUCHIAN<sup>a</sup>, RÉKA-ANITA DOMOKOS<sup>a</sup>, COSMINA CHIȘ<sup>b</sup>,  
MIHAI VASILESCU<sup>a</sup>, EMIL VINȚELER<sup>a</sup>, VASILE CHIȘ<sup>a,\*</sup>

**ABSTRACT.** The conformational and free energy landscape of levetiracetam (LEV) have been explored by DFT calculations, in gas-phase as well as in water, both for its monomeric and dimeric structures. The energetic order, relative free energies and Boltzmann populations have been calculated at B3LYP/6-31G+(2d,2p) level of theory. Six monomers and nine dimers of the three most stable conformers in water were considered. The identified monomers and dimers were then used to compute the population-averaged NMR spectra using Boltzmann statistics. Besides the two monomeric and dimeric structural models, two different procedures have been used for obtaining the calculated chemical shifts: the classical referencing method to TMS and the scaling procedure.

**Keywords:** *Levetiracetam; conformational analysis; NMR; DFT.*

### 1. INTRODUCTION

Levetiracetam (LEV) (IUPAC name (S)-2-(2-oxopyrrolidin-1-yl) butanamide (see Fig.1)), is the biologically active S-enantiomer of etiracetam. It is a second-generation antiepileptic drug (AED) used for the treatment of partial-onset seizures in patients with epilepsy [1,2].

---

<sup>a</sup> Babeș-Bolyai University, Faculty of Physics, 1 Kogălniceanu, RO-400084 Cluj-Napoca, Romania

<sup>b</sup> Children Emergency Hospital, Pediatric Neurology Department, 43 Victor Babeș Str., 400012 Cluj-Napoca, Romania

\* Corresponding author: [vasile.chis@phys.ubbcluj.ro](mailto:vasile.chis@phys.ubbcluj.ro).

Pandeya et al. [3] have proposed a pharmacophore model for the drugs having anticonvulsant activity. They suggested that such drugs must contain two hydrophobic binding sites A and C, one hydrogen-bonding site (HDB) and one electron donor group D. For levetiracetam A and C sites are prescribed to the ethyl side chain and methylene groups of the ring, HDB site to the amide group and D site to the carbonyl group located on the pentacyclic ring (see Fig. 1).

For a better understanding of the pharmacodynamics of LEV, the characterization of its liquid state structure is crucial. The analysis of the possible conformers of a particular molecule and the effect of the drug environment on their stabilities is essential for describing reliably its spectroscopic properties. The conformational landscape of LEV in water and dichloromethane was studied previously by Li et al. [4] who identified nine conformers. In the present work we identified twenty-two unique conformers of LEV in gas-phase and water. Subsequently, the six most stable structures were considered for computing the NMR spectra, which, in turn, were used to explain the experimental observations.

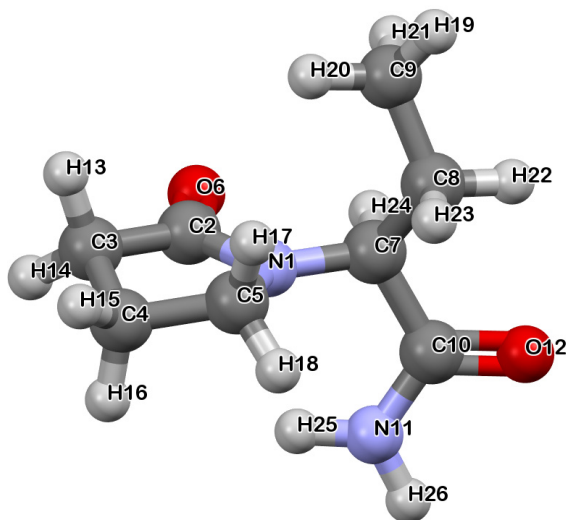


**Fig. 1.** Optimized molecular structure of the most stable conformer of levetiracetam in water at PCM-B3LYP/6-31+G(2d,2p) level of theory, with the atom numbering scheme

The spectroscopic response can be significantly affected by hydrogen bonding interactions. This is particularly important for NMR spectra recorded commonly in liquid state. Thus, a proper model containing dimers able to include such interactions must be used for a reliable assignment of the experimental spectroscopic data. Nine dimers containing the three most stable monomers in water were studied.

Previous NMR studies of LEV in chloroform have been reported [5-7]. However, when liquid state of a drug is envisaged, the solvent of choice should be water which is a physiologically adequate liquid. For this reason, in the present work LEV is studied by NMR spectroscopy in deuterated water and the experimental spectrum is explained on the basis of both monomeric and dimeric structures.

## 2. EXPERIMENTAL AND COMPUTATIONAL DETAILS

Levetiracetam was purchased from a standard commercial source (Tokyo Chemical Industry Co., Ltd.) and used without further purification. The  $^1\text{H}$  and  $^{13}\text{C}$  NMR spectra were recorded at room temperature on a Bruker AVANCE NMR spectrometer (400.13 MHz for  $^1\text{H}$  and 100.63 MHz for  $^{13}\text{C}$ , internal standard TMS). The samples were prepared by the dissolution of LEV in  $\text{D}_2\text{O}$  (signal for  $^1\text{H}$  at 4.78). The spectra were recorded using a single excitation pulse of 11  $\mu\text{s}$  for  $^1\text{H}$  and 7.5  $\mu\text{s}$  for  $^{13}\text{C}$ .

The conformational space of LEV in vacuum was initially explored with the Tinker software using the MMFF94 molecular mechanics force field [8]. As starting geometries we used the solid-state structures reported for LEV [9] as well as the LEV's geometries found in the anhydrous polymorphic forms and hydrate phase of etiracetam [10]. The identified stable conformers have been further optimized in gas-phase and water, based on DFT quantum chemical calculations. Frequency calculations confirmed that all the optimized geometries correspond to minima on the potential energy surface. DFT geometry optimizations and frequency calculations were performed with

the Gaussian09 software package [11] by using DFT approaches. Through this study, the hybrid B3LYP exchange-correlation functional [12-15] was used in conjunction with Pople's split-valence basis set 6-31G+(2d,2p) [16].

The calculation of NMR spectrum of LEV was performed using the GIAO (Gauge-Including Atomic Orbital) method [17,18], implemented in the Gaussian09 package, at the theoretical level indicated above. In order to express the chemical shifts in terms of the total computed NMR shielding tensors, we used two different approaches: i) the standard referencing method to tetramethylsilane (TMS) and ii) the scaling procedure based on linear regression analysis [19]. For the referencing procedure, the geometry of TMS molecule (in  $T_d$  symmetry) has been optimized and then its NMR shielding tensors have been obtained at the same level of theory as that used for LEV.

### 3. RESULTS AND DISCUSSIONS

The conformational landscape of LEV was initially obtained based on MM calculations of one LEV molecule in gas-phase using the Tinker software, with the MMFF94 molecular mechanics force field [20]. However, in liquid state the conformational landscape and equilibria of a solvated molecule can be drastically different, with the solvent playing a critical role in the structure and dynamics of the solvated molecule.

The geometries of the conformers obtained from molecular mechanics simulations were further optimized at B3LYP/6-31G+(2d,2p) level of theory, in gas-phase and water, using the Gaussian 09 program packages [11]. Solvent effects have been considered by using the continuum PCM solvent model. Twenty-two conformers have been finally identified. Relative Gibbs energies in gas-phase and water of the six most stable LEV conformers have been collected in Table 1.

LEV conformers have been generated by varying the torsion angle around three rotatable bonds (C8-C7, C10-C7, C7-N1) and by out-of-plane deformation of pentacyclic ring. The dihedral angles C9-C8-C7-N1, N11-C10-C7-N1, C8-C7-N1-C5 and C3-C4-C5-N1 characterizing the six most stable conformers shown in Fig. 2 are summarized in Table 1.

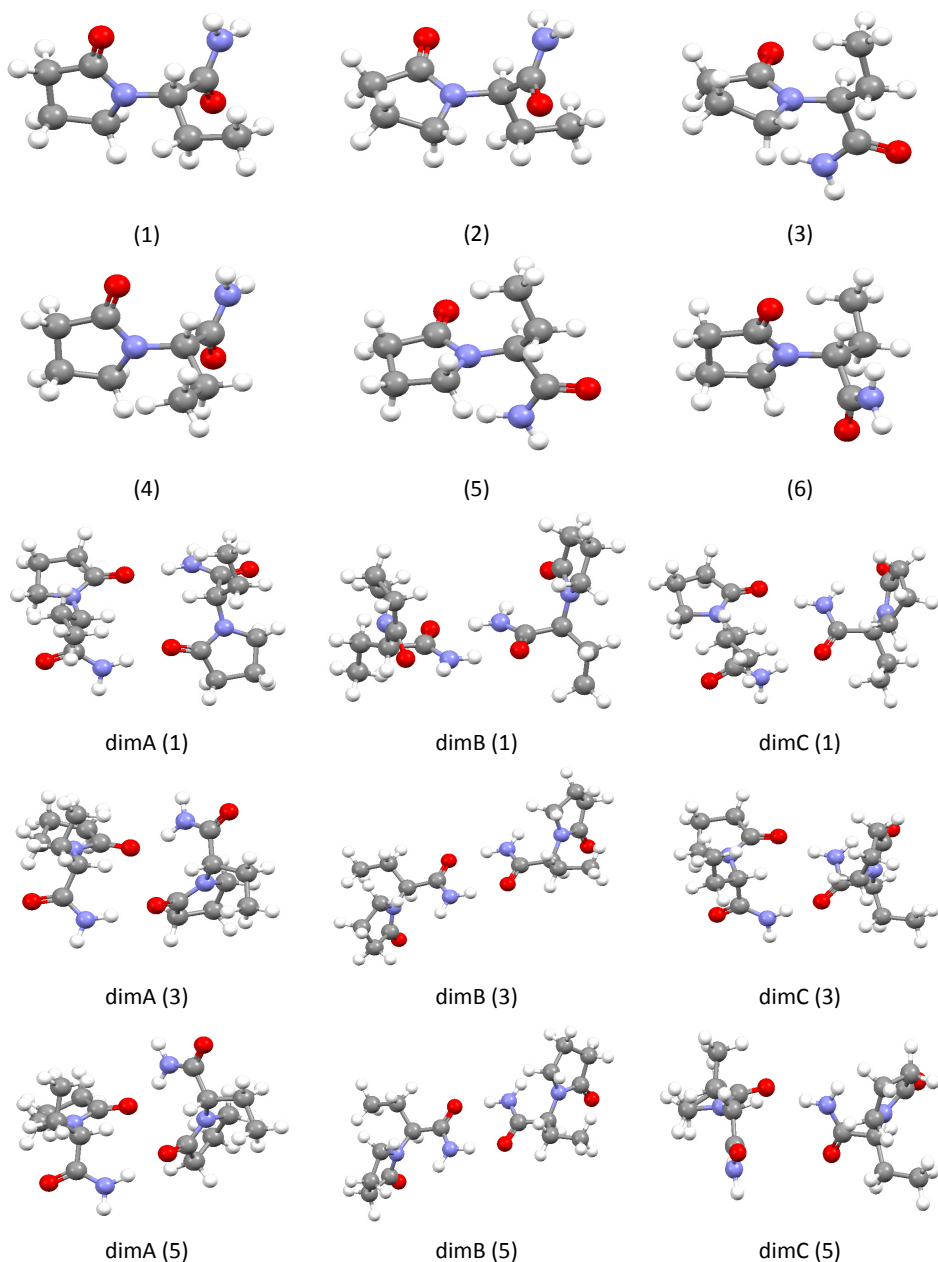


**Fig. 2.** B3LYP/6-31+G(2d,2p) optimized structures of the levetiracetam monomers and dimers in water: six most stable monomers and nine types of dimers.

**Table 1.** B3LYP/6-31+G(2d,2p) calculated relative Gibbs energies (with respect to the most stable conformer) and dihedral angles (degrees) characterizing the levetiracetam monomers in gas-phase and water (first and second entry, respectively) and dimers in water.

Conformer	$\Delta G$ (kcal mol <sup>-1</sup> )	C9-C8-C7-N1	N11-C10-C7-N1	C8-C7-N1-C5	C3-C4-C5-N1
<b>TG+G-C+ (1)</b>	0.00	-167.1	79.2	-45.6	26.6
	0.43	-170.9	103.6	-57.3	25.9
<b>TG+G-C- (2)</b>	0.32	-168.9	79.1	-36.0	-21.8
	0.73	-172.3	104.9	-50.3	-25.5
<b>G-G+G-C+ (3)</b>	0.33	-61.3	77.5	-47.7	27.0
	0.13	-59.0	22.3	-55.7	22.2
<b>G-G+G-C+ (4)</b>	0.33	-61.4	77.5	-47.6	27.0
	0.55	-59.5	107.2	-56.0	26.2
<b>G-G+G-C- (5)</b>	0.46	-65.2	77.0	-40.9	-20.5
	0.00	-62.0	18.7	-50.9	-26.7
<b>G-G+G-C- (6)</b>	0.47	-65.2	77.0	-40.8	-20.6
	0.71	-63.0	115.0	-49.0	-25.6
Dim A <b>(1)</b>	0.00	-172.0	107.8	-66.7	25.1
		-172.0	108.2	-66.6	25.1
Dim B <b>(1)</b>	0.87	-166.6	78.2	-47.3	26.0
		-166.6	78.2	-47.3	26.0
Dim C <b>(1)</b>	0.61	-170.7	113.8	-54.7	25.9
		-166.0	77.2	-46.7	26.1
Dim A <b>(3)</b>	1.43	-59.0	36.8	-64.1	22.6
		-60.0	114.2	-60.3	25.4
Dim B <b>(3)</b>	1.07	-59.2	16.8	-53.4	22.3
		-59.2	16.8	-53.5	22.3
Dim C <b>(3)</b>	0.41	-59.5	120.3	-53.1	26.0
		-61.0	71.1	-49.0	26.3
Dim A <b>(5)</b>	0.88	-62.0	116.4	-51.2	-25.4
		-61.6	28.7	-55.3	-24.5
Dim B <b>(5)</b>	0.51	-62.4	16.5	-49.3	-26.4
		-62.4	16.5	-49.3	-26.4
Dim C <b>(5)</b>	1.10	-62.2	17.5	-50.1	-26.1
		-63.2	15.4	-48.6	-26.7

The dihedral angle defining the relative orientation of the amide group, N11-C10-C7-N1, for the six conformers in gas-phase is between  $77.0^\circ$  (for **(6)**) and  $79.2^\circ$  (for **(1)**). As seen in Table 1, this angle is, expectedly, the most sensitive to the solvent effects, being significantly smaller for gas-phase conformers than for the liquid-phase partners. The relative orientation of whole butanamide group with respect to the oxopyrrolidin ring is defined by the C8-C7-N1-C5 dihedral, which, according to the present results is also significantly affected by the solvent. This dihedral takes values between  $-47.6^\circ \div -36.0^\circ$  in gas-phase, but it increases slightly for the conformers optimized in water.

By varying the torsion angle around the C8-C7 we obtained two types of conformers denoted using as the first character T or G- (see Table 1). Thus, for example, TG+G-C+ (**(1)**) is a trans-conformer with dihedral angle C9-C8-C7-N1 of  $-167.1^\circ$  and the lowest relative energy in gas-phase, while **(3)** is a gauche conformer with the same dihedral angle in gas-phase of  $-61.3^\circ$ . By varying the torsion angle around the C4-C5 bond we obtained two types of LEV conformers denoted by the fourth character as C- and C+, with dihedral angles C3-C4-C5-N1 between  $-21.8^\circ \div -20.5^\circ$  and  $26.6^\circ \div 27.0^\circ$  (see Table 1).

The conformational space of LEV in gas-phase is quite distinct from that in water. For conformers **(1)** – **(6)** such differences are observed for both N11-C10-C7-N1 and C8-C7-N1-C5 dihedrals. For a particular conformer, the C3-C4-C5-N1 dihedral that defines the chair or boat conformation of the oxopyrrolidin ring does not change appreciably between the gas and liquid phases.

There are three types of dimers formed from monomers with the same structure. The dimer dimA is formed as a result of two hydrogen bonds of the same type O6...H26N11, dimB is formed through two hydrogen bonds O12...H25N11, while the stability of dimC is due to two hydrogen bonds of different type O6...H25N11 and O12...H26N11. The monomers **TG+G-C+ (1)** that form dimers dimB in water have a structure similar to that in gas-phase. The hydrogen bonding interaction O12...H25N11 changes the N11-C10-C7-N1 and C8-C7-N1-C5 dihedral angles from  $103.6^\circ$  and  $-57.3^\circ$  (the values of free

monomer **TG+G-C+ (1)** in water) to  $78.2^{\circ}$  and  $-47.3^{\circ}$ , respectively (similar to values  $79.2^{\circ}$  and  $-45.6^{\circ}$  of free monomer **TG+G-C+ (1)** in gas-phase). The specificity of hydrogen bonding interaction involving the O6 atom (O6...H25N11 and O6...H26N11) is maintained also in dimC where the corresponding monomer **TG+G-C+ (1)** has dihedral values of  $77.2^{\circ}$  and  $-46.2^{\circ}$ , similar to values in gas-phase. Instead, the hydrogen interaction involving the O12 atom has the opposite effect, increasing N11-C10-C7-N1 dihedral angle from  $103.6^{\circ}$  to  $107.8^{\circ}$  in dim A and to  $113.8^{\circ}$  in dimC.

For the dimers having the same type of hydrogen bonding interactions, like dimA and dimB, it is expected that the structure of the two monomers to remain practically unchanged within the dimers. This, indeed, holds for dimers of type B, but for dimers of type A it holds only for dimA **(1)**. In dimA **(3)**, the hydrogen bonding interaction leads to the increase of the energy of the system and permits to fall in a new energy valley where one of the monomers **G-G+G-C+ (3)** transforms in the higher-energy conformer **G-G+G-C+ (4)**. The same holds for dimA (5) where one of the monomers **G-G+G-C- (5)** transforms in the higher-energy conformer **G-G+G-C- (6)**. This doesn't happen for dimA **(1)**, because the hydrogen interaction do not modify the dihedral angle C3-C4-C5-N1 and conformer **TG+G-C+ (1)** cannot transform in the conformer with higher energy **TG+G-C- (2)**.

NMR data for LEV in  $\text{CDCl}_3$  have been previously reported in refs. [5,9,21]. To the best of our knowledge, no such data exist for LEV in water and for this reason we decided to do an experimental work on both  $^1\text{H}$  and  $^{13}\text{C}$  NMR spectra of LEV in this solvent.

The  $^1\text{H}$  and  $^{13}\text{C}$  NMR spectra of LEV are given in Fig.3 and the experimental and theoretical chemical shifts are summarized in Table 2. For a reliable assignment of NMR spectra of organic molecules, the calculation of chemical shifts associated with their magnetic nuclei is essential. Thus, the experimental NMR data for LEV obtained in  $\text{D}_2\text{O}$  were explained on the basis of DFT calculations performed on the most stable conformers in water. As pointed out by Willoughby et al. [19], when different conformers with relative energies within few  $\text{kcal}\cdot\text{mol}^{-1}$  are possible for a given compound, they will contribute collectively giving rise to an averaged spectrum. For taking

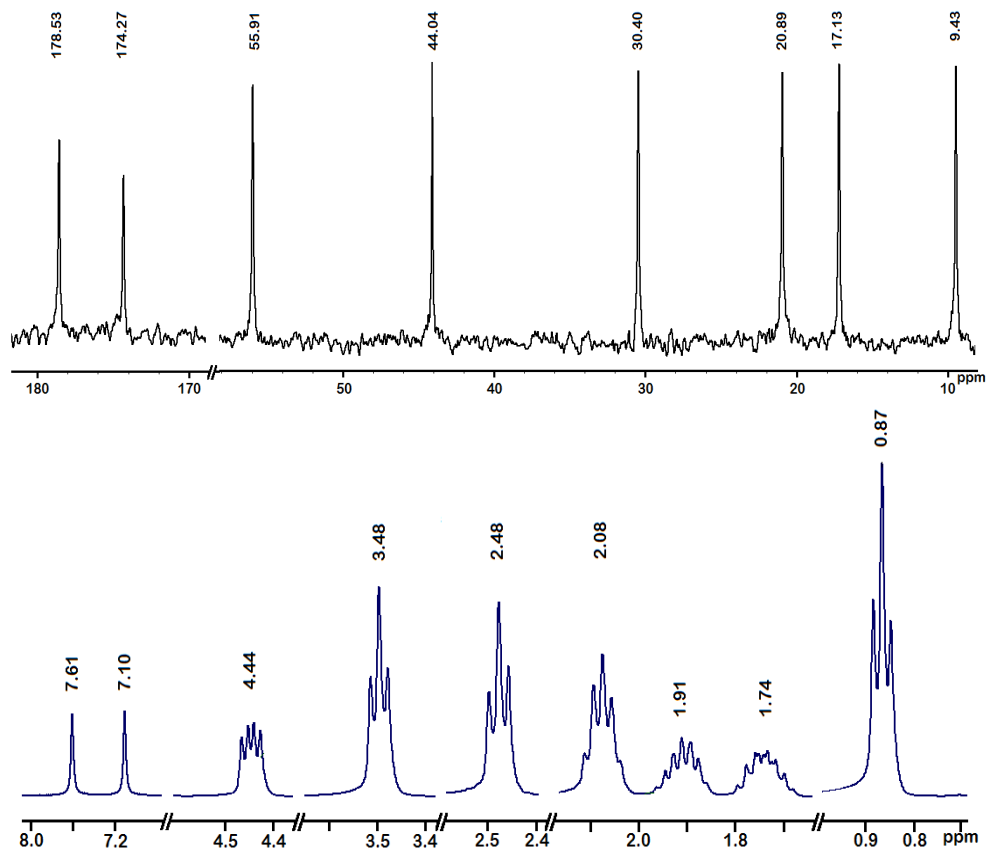


**Fig. 3.** <sup>1</sup>H (bottom) and <sup>13</sup>C (top) NMR spectra of levetiracetam in D<sub>2</sub>O solution

**Table 2.** Experimental and theoretical chemical shifts (in ppm) for LEV in D<sub>2</sub>O

Nucleus	Experimental data	Theoretical data TMS Monomers	Theoretical data scaled Monomers	Theoretical data TMS Dimers	Theoretical data scaled Dimers
C2	178.53	175.43	178.81	174.66	178.39
C10	174.27	170.71	173.89	170.74	174.26
C7	55.91	57.91	56.24	57.89	55.75
C5	44.04	45.66	43.46	47.00	44.31
C3	30.40	33.58	30.86	34.09	30.76

Nucleus	Experimental data	Theoretical data TMS Monomers	Theoretical data scaled Monomers	Theoretical data TMS Dimers	Theoretical data scaled Dimers
C8	20.89	24.40	21.30	25.63	21.87
C4	17.13	20.96	17.70	21.66	17.71
C9	9.43	11.97	8.33	12.01	7.56
H26	7.61, s	6.07	7.30	7.90	7.84
H25	7.10, s	6.06	6.72	6.80	6.76
H24	4.44, 1H, dd	4.76	5.37	4.70	4.69
H17, H18	3.49, 2H, t	3.51	3.79	3.51	3.53
H13, H14	2.48, 2H, t	2.44	2.45	2.34	2.38
H15, H16	2.08, 2H, quin	2.04	1.94	1.98	2.02
H23	1.91, 1H, m	2.18	2.12	2.00	2.04
H22	1.74, 1H, m	1.59	1.38	1.58	1.63
H19-H21	0.87, 3H, t	0.81	0.39	0.85	0.91

into account this effect, the LEV conformers found in gas phase have been re-optimized in water by considering the solvent effect using the polarized continuum model (PCM). The first six conformers with the lowest relative Gibbs energies are given in Table 1. Calculation of vibrational frequencies has confirmed that the six structures are stationary points on the potential energy surface with no negative eigenvalue observed in the force constant matrix. For chemical shift calculations, the structures of these six LEV conformers were taken into account, for each LEV conformer being assigned a Boltzmann weight at the room temperature. Then, for  $^{13}\text{C}$  and  $^1\text{H}$  nuclei, the isotropic part of the computed NMR shielding tensors are obtained as the Boltzmann weighted contributions of the six most stable conformers. Subsequently, the theoretical chemical shifts are derived from the computed NMR shielding tensors by using the scaling parameters (slope and intercept, respectively) derived from linear regression analysis, according to the procedure proposed recently by Willoughby et al. [19]. Calculated chemical shifts have been obtained also by referencing to the calculated shielding tensors of H and C nuclei in TMS molecule.

The most important differences between the chemical shifts obtained in D<sub>2</sub>O and CDCl<sub>3</sub> solvents are noted for C2, C10 and the amino protons. The resonances of the last two protons appear in D<sub>2</sub>O at 7.61 and 7.10 ppm indicating their de-shielding compared to the chloroform solution where these resonances are seen at 5.75 and 6.45 ppm [5,9,21]. Conversely, the C2 and C10 nuclei are slightly more shielded in water (178.53 and 174.27 ppm) than in CDCl<sub>3</sub> (175.9 and 172.7 ppm [5]).

On the other hand, as can be seen in Table 2, the largest discrepancies between the experimental and calculated (Boltzmann population-averaged) scaled chemical shifts for monomeric conformers are noted for C9 and H19-21 nuclei. All these nuclei belong to the ethyl side chain and most probably these slight mismatches are due to the flexibility of this chain.

It is important to note also that the protons of the methylene groups are chemically equivalent, excepting the group in the ethyl chain. The non-equivalence of the two H22 and H23 protons can be explained considering that this methylene group is directly bonded to the chiral center of the molecule. Thus, the environment is different and a quite large geminal coupling is expected for the two protons. Indeed, the quantum chemical calculations give a  $^2J_{22,23}$  coupling constant of 13.4 Hz, within the range characteristic for such couplings [22]. The nonequivalence of these protons is observed also in the splitting pattern of the H24 peak which is a doublet of doublets, due to the  $^3J$  coupling of this proton with the H22 and H23 protons. The <sup>1</sup>H NMR spectrum (see Fig. 3) shows that the peaks corresponding to the H13-14 and H17-18 pairs are triplets due to the vicinal  $^3J$  coupling with the H15-16 protons, while the peak of the last pair is a quintet due to the almost equivalent coupling with the four protons of the neighbor methylene units.

Comparing the two procedures used for the calculation of chemical shifts it is evident from Table 2 that the scaling procedure gives consistently a better agreement with the experimental data.

For <sup>1</sup>H chemical shifts, the dimer models improve significantly the agreement with the experiment for the amino protons. This behavior is due

the involvement of these protons in hydrogen bonding interactions between the monomers. Thus, the present reported data suggest the dimer formation at working concentration for NMR measurements.

## 5. CONCLUSIONS

Using DFT quantum chemical calculations, six LEV conformers have been identified in water, within a 0-0.71 kcal·mol<sup>-1</sup> energy window. Their energetic order changes significantly when going from gas-phase to water solution. Particular features of the geometries of monomeric and dimeric structures have been explained by considering the possible intra- or inter-molecular hydrogen bonding interactions and their structures were optimized at B3LYP/6-31G+(2d,2p) level of theory. Using the three most stable monomers, we constructed nine dimers formed from monomers of the same type and subsequently calculated their relative free energies and NMR spectra.

Both, <sup>1</sup>H and <sup>13</sup>C NMR spectra have been reliably assigned based on theoretical data derived at B3LYP/6-31+G(2d,2p) level of theory. Our data suggest that the formation of dimeric structures is evident at the working concentration used for recording the NMR spectra.

## ACKNOWLEDGMENTS

The research undertaken for this article was conducted using the Babeş-Bolyai University Research infrastructure financed by the Romanian Government through the programme PN II – Capacities – project title Integrated Network for Interdisciplinary Research – INIR.

V. Chiş highly acknowledges financial support from UEFISCDI PN-II-RU-TE-2012-3-0227 grant.

## REFERENCES

- [1] F. Gualtieri, D. Manetti, M.N. Romanelli, C. Ghelardini, *Curr. Pharm. Des.*, 8 (2002) 125–138.
- [2] C.M. Ulla, A. Towfigh, J. Safdieh, *Neuropsychiatr. Dis. Treat.*, 5 (2009) 467-476.
- [3] S.N. Pandeya, A.S. Raja, J.P. Stables, *J. Pharm. Pharmaceut. Sci.*, 5 (2002) 266-271.
- [4] L. Li, Y.-K. Si, *J. Pharm. Biomed. Anal.*, 56 (2011) 465– 470.
- [5] K. Chandra Babu, R. Buchi Reddy, K. Mukkanti, K. Suresh, G. Madhusudhan, S. Nigam, Hindawi Publishing Corporation, *J. Chem.*, (2013) 176512.
- [6] S. Hildenbrand, PhD thesis, Levetiracetam and Brivaracetam: Synthesis of Radioligands as Pharmacological Tools for Studying Their Interactions with Target Proteins, Bonn 2012, p.118.
- [7] K. Das Sarma, J. Zhang, Y. Huang, J.G. Davidson, *Eur. J. Org. Chem.*, 37 (2006) 3730-3737.
- [8] Y. Shi, Z. Xia, J. Zhang, R. Best, C. Wu, J. W. Ponder, P. Ren, *J. Chem. Theory Comput.*, 9 (2013) 4046-4063.
- [9] J. Song, K.X. Lou, X.J. Li, X.P. Wu, R.X. Feng, *Acta Cryst. E59* (2003) 1772-1773.
- [10] C. Herman, V. Vermylen, B. Norberg, J. Wouters and T. Leysens, *Acta Cryst. B69* (2013), 371-378.
- [11] M.J. Frisch, G.W. Trucks, H.B. Schlegel, G.E. Scuseria, M.A. Robb, J.R. Cheeseman, G. Scalmani, V. Barone, B. Mennucci, G.A. Petersson, H. Nakatsuji, M. Caricato, X. Li, H.P. Hratchian, A.F. Izmaylov, J. Bloino, G. Zheng, J.L. Sonnenberg, M. Hada, M. Ehara, K. Toyota, R. Fukuda, J. Hasegawa, M. Ishida, T. Nakajima, Y. Honda, O. Kitao, H. Nakai, T. Vreven, J.A. Montgomery, J.E. Peralta, F. Ogliaro, M. Bearpark, J.J. Heyd, E. Brothers, K.N. Kudin, V.N. Staroverov, R. Kobayashi, J. Normand, K. Raghavachari, A. Rendell, J.C. Burant, S.S. Iyengar, J. Tomasi, M. Cossi, N. Rega, J.M. Millam, M. Klene, J.E. Knox, J.B. Cross, V. Bakken, C. Adamo, J. Jaramillo, R. Gomperts, R.E. Stratmann, O. Yazyev, A.J. Austin, R. Cami, C. Pomelli, J.W. Ochterski, R.L. Martin, K. Morokuma, V.G. Zakrzewski, G.A. Voth, P. Salvador, J.J. Dannenberg, S. Dapprich, A.D. Daniels, O. Farkas, J.B. Foresman, J.V. Ortiz, J. Cioslowski, D.J. Fox, Gaussian09, Revision A.2, Gaussian, Inc., Wallingford, CT, 2009.
- [12] A.D. Becke, *J. Chem. Phys.*, 98 (1993) 5648-5652.
- [13] C. Lee, W. Yang, R.G. Parr, *Phys. Rev. B* 37 (1988) 785-789.

- [14] S.H. Vosko, L. Wilk, M. Nusair, *Can. J. Phys.*, 58 (1980) 1200-1211.
- [15] P.J. Stephens, F.J. Devlin, C.F. Chabalowski, M.J. Frisch, *J. Phys. Chem.*, 98 (1994) 11623-11627.
- [16] W.J. Hehre, R. Ditchfield, J.A. Pople, *J. Chem. Phys.*, 56 (1972) 2257-2261.
- [17] R. Ditchfield, *Mol. Phys.*, 27 (1974) 789-807.
- [18] K. Wolinski, J.F. Hilton, P. Pulay, *J. Am. Chem. Soc.*, 112 (1990) 8251-8260.
- [19] P.H. Willoughby, M.J. Jansma, T.R. Hoye, *Nature Protoc.*, 9 (2014) 643-660.
- [20] Y. Shi, Z. Xia, J. Zhang, R. Best, C. Wu, J. W. Ponder, P. Ren, *J. Chem. Theory Comput.*, 9 (2013) 4046-4063.
- [21] R. Mylavarapu, R.V. Anand, G.C.M. Kondaiah, L.A. Reddy, G.S. Reddy, A. Roy, A. Bhattacharya, K. Mukkanti, R. Bandichhor, *Green Chem. Lett. Rev.*, 3 (2010) 225-230.
- [22] E. Breitmaier, *Structure Elucidation by NMR in Organic Chemistry: A Practical Guide*, John Wiley & Sons, Ltd, 2002, pag.21.

# MICROWAVE-ASSISTED SYNTHESIS OF CARBON NANOPARTICLES USING A HIGH PERFORMANCE MICROWAVE REACTOR

R.V. BARITCHI<sup>a</sup>, G. KATONA<sup>b</sup>,  
B. MARTA<sup>a</sup> and S. ASTILEAN<sup>a,c,\*</sup>

**ABSTRACT.** The use of Microwave-Assisted Hydrothermal (MAH) production of carbon-based nanomaterials is frequent, but in practice the most common employed equipments are domestic microwave or digestion ovens. Here we investigate the synthesis of Carbon Nanoparticles (CNs) using a dedicated microwave reaction system (Monowave 300 from Anton Paar), aiming to define the operational parameters of the system in order to optimize the synthesis procedure. The optical properties of synthesized CNs were analyzed by UV-Vis absorption spectroscopy, steady-state and time-domain photoluminescence measurements while their size and morphology were characterized by Transmission Electron Microscopy (TEM).

**Keywords:** Carbon nanoparticles, photoluminescence, microwave.

## INTRODUCTION

Carbon-based nanomaterials such as carbon nanotubes and nanofibers, fullerenes, nanodiamonds, graphenes or, more recently, carbon nanoparticles (CNs) exhibit unique chemical and physical properties which are very attractive

---

<sup>a</sup> Nanobiophotonics and Laser Microspectroscopy Center, Interdisciplinary Research Institute in Bio-Nano-Sciences, 42 Treboniu Laurian, 400271 Cluj-Napoca, Romania

<sup>b</sup> Faculty of Chemistry and Chemical Engineering, 11 Arany János str., 400028 Cluj-Napoca, Romania

<sup>c</sup> Faculty of Physics, 1 Kogălniceanu str., 400084 Cluj-Napoca, Romania

\* Corresponding author: simion.astilean@phys.ubbcluj.ro

for both technological and biomedical applications [1]. Carbon-based nanomaterials are produced using a large variety of chemical or physical procedures which can be classified in “bottom-up” or “top-down” fabrication strategies. Among the bottom-up procedures, one of the most handily procedures is based on high temperature chemical reaction of various organic molecules which play as sources of carbon.

When the energy is delivered to chemical reaction using microwave radiation and the solvent used is water, the procedure is referred in literature as microwave-assisted hydrothermal (MAH) treatment [2]. The most important advantage of using microwaves is the almost instantaneous heating and the enhancement of reactions yield with a significant decrease of reaction time and of unwanted byproducts. In particular the use of a dedicated Microwave-Assisted Organic Synthesis (MAOS) equipment has several additional advantages due to close reactor or reaction tank (with the possibility to control the atmosphere), high heating rate and focused energy density trough a waveguide or “on demand” magnetic stirring option. The equipment also allows addition of metal ions and particles as catalyst or reactants. Consequently, an important feature of MAOS equipment relative to domestic microwave or digestion ovens is the very good reproducibility of the synthesis results. When used in nanoparticles production process, such equipments are referred as Microwave-Assisted Nanomaterial Synthesis (MANS) equipment [3].

It was observed that the properties of CNs fabricated by bottom-up procedures usually display very similar properties, almost independent by the raw materials used. In literature there are reported synthesis procedures starting from various pure materials like dextrin [4], or natural organic mixtures like orange juice [5], natural *Bombyx mori* silk [6] or coffee ground [7] with very similar results. In the present paper we investigate the production of CNs starting from a simple carbohydrate - glucose - using procedures similar to some described in the literature, with the important difference of using a dedicated equipment instead of regular microwave oven [2]. The aqueous glucose solution reaction at high temperature produces CNs (in occurrence microparticles) simultaneously with other chemical species as byproducts

and large amounts of gases (methane, carbon monoxide and dioxide) which can generate very high pressure in a close reactor. It is difficult to control the advancement of such reaction in a simple microwave oven working under constant power radiation and open atmosphere. Therefore in our case we had to find the equipment setup for production of CNs with properties similar to those described in the literature [8].

## EXPERIMENTAL

### Chemicals

Glucose (Alpha-d-glucopyranose, laboratory grade, Sigma-Aldrich), ultrapure water.

### Equipments

The equipment Monowave 300 (Anton Paar, Austria) is designed to provide high precision delivery of microwave power, reliable reading of temperature using both an IR sensor and immersed ruby thermometer and controllable magnetic stirring of reaction mixture (see Figure 1). The user has to write a setup file to pilot the sequences of heating, cooling or hold

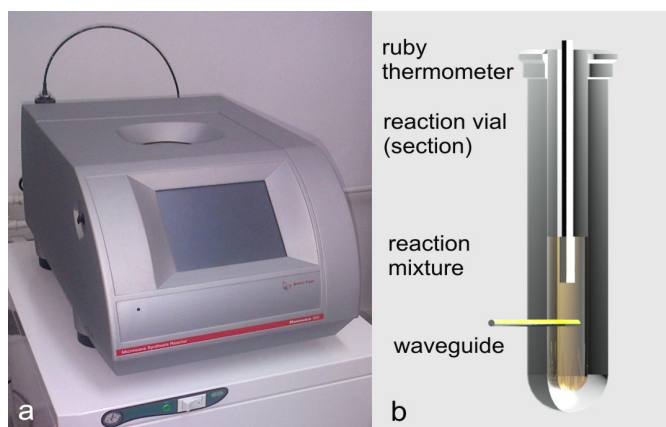


**Fig. 1 a.** Anton Paar Monowave 300 picture and **b.** a figure of the reaction vial.

procedure with or without magnetic stirring. In a 'hold' procedure, the reactor temperature is constant for the programmed period of time by delivering automatically the required microwave power. In principle, to produce CNs through the MAH process we can modify and optimize multiple parameters like: raw material composition and amount, temperature, atmosphere composition, heating curve, and stirring speed. The equipment allows a very large number of heating and cooling parameters, using an unlimited number of steps. The reaction mixture can be heated as fast as possible (for this procedure the use of the ruby thermometer is mandatory), either in a defined period of time or working under a constant power regime. The temperature reaction can be actively maintained in time and for each step the stirring speed can be adjusted. On effect, the number of setups that can be programmed and executed is almost unlimited. The existent limitations are regarding a minimal and maximal volume of reactant and the pressure inside the reaction vial (limited at maximum of 32 bars) which cannot be directly controlled, but only through the temperature versus volume of reactant ratio for a given synthesis.

UV-Vis absorption spectra of CNs and byproducts resulted from MAH of glucose solutions were measured on a Jasco V-670 spectrometer at 1 nm resolution and scan speed of 1000 nm per minute, using a 2 mm quartz cell. Steady-state photoluminescence spectra were recorded on a Jasco FP-6500 spectrofluorometer. Photoluminescence lifetime measurements were performed using a time-resolved confocal fluorescence microscope (PicoQuant MicroTime 200) equipped with a pulsed diode laser (LDH-D-C-375, PicoQuant) operating at 375 nm with a pulse repetition rate of 40 MHz. The photoluminescence collected by a 60x/NA 1.2 water immersion objective was spatially filtered through a 50  $\mu\text{m}$  pinhole, spectrally filtered using a low-pass optical filter (HQ405LP from Shemrock) and detected by Single Photon Avalanche Diode (SPAD) to be finally processed by PicoQuant PicoHarp 300 Time-Correlated Single Photon Counting (TCSPC) data acquisition unit.

A Hitachi H-7650 field emission TEM operating at an accelerating voltage of 120 kV and equipped with Olympus Keenview G2 CCD camera

was employed to obtain the TEM images. The samples were deposited on Formvar/Carbon 300 mesh film coated Cu grids with grid hole size of 63  $\mu\text{m}$ .

## RESULTS AND DISCUSSION

A stock solution of glucose in ultrapure water (180 mg/ml) was magnetically stirred for 1 hour and used as raw material for microwave treatment. The synthesis procedure begins with 3 ml of above solution poured in the reaction vial (see Figure 1.a) of 10 ml volume to be heated as fast as possible up to 200°C under 600 rpm stirring. The different samples were prepared by varying the hold time (0, 1, 3, 5, 7, 9, 11, 13 minutes) of MAH reaction at 200 °C followed by cooling down the reaction products at room temperatures. Two examples of parameters evolution as recorded by the machine for 1 and 11 minutes hold time are illustrated in the Figure 2. Finally, the resulted yellow color suspensions (see Figure 3) were subjected to dialysis procedure against ultra pure water for 24 hours.

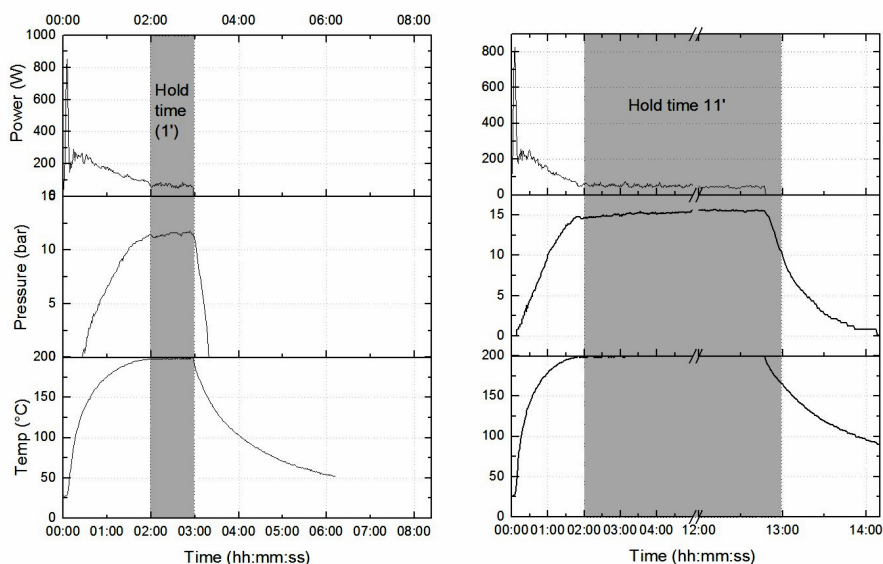


**Fig. 2.** Time-course of microwave power, pressure and temperature for the hold time of 1 and 11 minutes at 200 °C as recorded by MAOS machine.

The parameters of CNs synthesis are automatically monitored by our equipment as illustrated in the Figure 2 for the case of hold time of 1 minute and 11 minutes, respectively. It can be noticed that the time course of power, pressure and temperature correlate very well, which is essential to provide precision and reproducibility in any microwave-assisted synthesis.

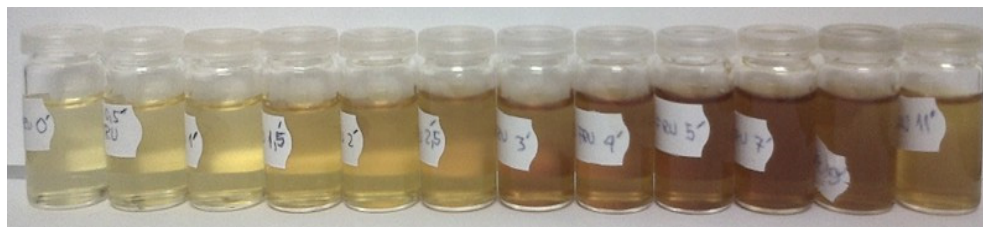


**Fig. 3.** Digital image of the samples resulted from different time reaction.

The amount of energy absorbed by each sample can be estimated by integration of the power curve as function of time. The first period of irradiation is characterized by a medium power of 147.6 watt and the second period by a constant power of 68.5 watt. The irradiation power is constant from sample to sample but the irradiation time increases in steps of 2 minutes for each consecutive synthesis.

The UV-Vis absorption spectra of products resulted after microwave treatment at increasing hold time are shown in Fig. 4.a. The spectra exhibit two well resolved absorption bands located at 228 and 282 nm which can be assigned to  $\pi$ - $\pi^*$  electronic transitions in C=C bonds and to  $n$ - $\pi^*$  electronic transitions in C=O carbonyl bonds, respectively. According to data in literature, CN exhibit electronic transitions in the same UV-Vis region of spectrum due to their aromatic domains and oxygen-containing moieties and, therefore, it is conceivable that their own spectra overlap with spectra of reaction byproducts [8, 9]. The as produced mixture possesses a sweet smell produced mainly by diacetyl (2,3-butanedione). The color of the mixture is mostly associated with the amount of caramelan and its polymers (carmelen, caramelin) byproducts. The discoloration of the samples with longer heating time indicates that these large molecules are consumed in the later reaction steps

like: equilibration of anomeric and ring forms, condensation, intramolecular bonding, isomerization of aldoses to ketoses, dehydration reactions, fragmentation reactions and unsaturated polymer formation [9]. We noticed that the UV-Vis bands intensity increases monotonically with the hold time up to around 11 minutes when an important decrease is noticed for longer hold times. For our purpose, the accelerated depletion of caramelans is associated with a fast - unwanted - increase in CN size, as resulted from TEM measurement (see text below).

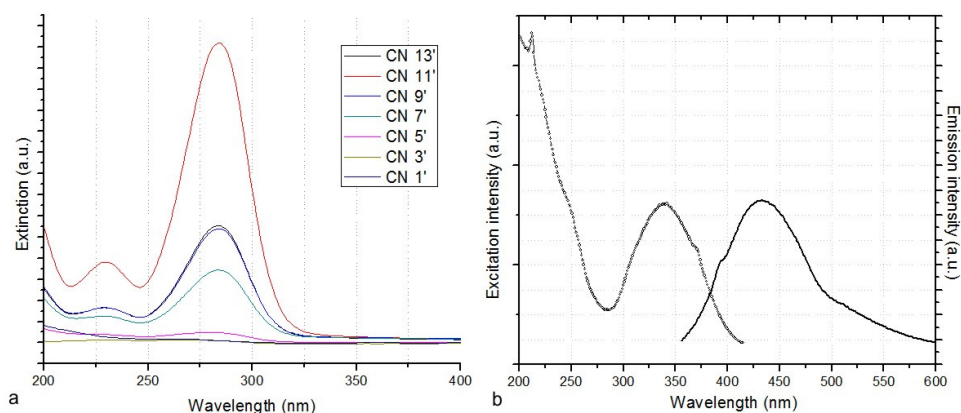


**Fig. 4 a.** UV-Vis absorption spectra of CNs suspensions as function of increased hold time; **b.** Photoluminescence spectrum for the excitation wavelength at 350 nm (continuous line) versus excitation spectrum recorded for detection wavelength at 450 nm (dotted line) of the CNs suspensions produced with a hold time of 3 minutes.

Next, we investigated the luminescence properties of the synthesized CNs. A typical emission around 440 nm was obtained when the sample was photoexcited at 350 nm (Figure 4. b – continuous line). The corresponding excitation spectrum (emission collected at 450 nm) shows two bands (Figure 4.b - dotted line), a well defined band at 340 nm and the other extended in 280-220 nm region corresponding to second electronic transition of CNs discussed above.

Photoluminescence spectra recorded in Figure 4 b feature large Stokes shift (distance between excitation and emission maxima) and large spectral interval of excitation which are typical to CNs characteristics in literature [10]. We further explored their luminescent properties by monitoring the excited-state decay of CNs on the nanosecond time scale using fluorescence time-correlated single photon counting (TCSPC) measurements on MicroTime 200 system. Figure 5 presents the excited-state luminescence decay profile of CNs when excited at 375 nm wavelength by a diode laser with a pulse repetition rate of 40 MHz. The decay curve can be fitted with a tri-exponential equation corresponding to three lifetime components, namely, 1.93, 0.62, and 4.58 ns, with respective relative amplitudes of 38.7%, 50%, and 10.3% which reveal a mean lifetime of 3.32 ns.

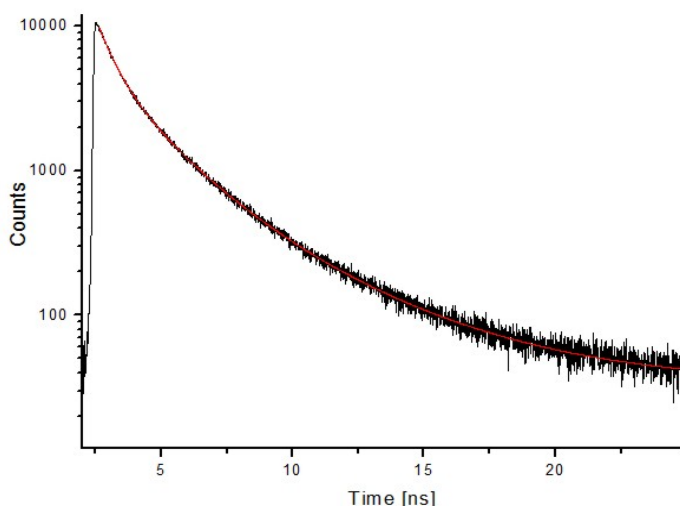


**Fig. 5.** Time-resolved PL spectra of the as-prepared CNs. Black line represents experimental data and red line the fitted curve.

The solid products resulted from the MAH were characterized by TEM. The analysis of TEM pictures presented in Figure 6 reveals formation of CNs of 9 nm average diameter in the case of sample treated for 3 minutes and a large amount of non-luminescent particles of 27 nm average diameter, in the case of sample treated for 13 minutes.

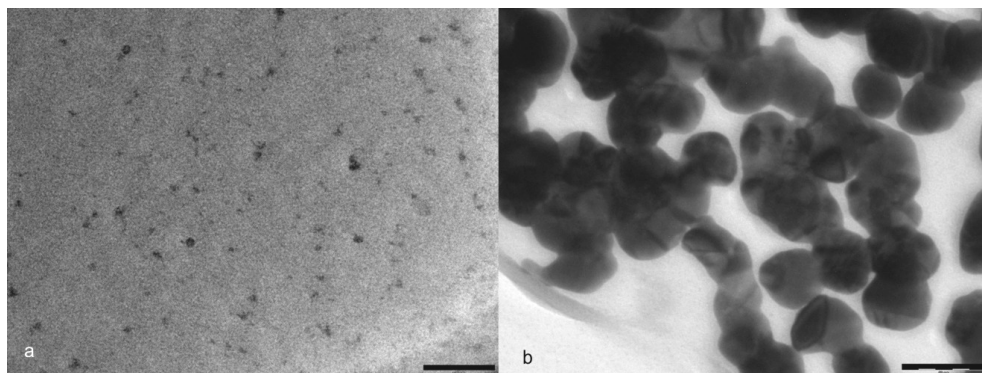


**Fig. 6.** TEM image of the CNs resulted: **(a)** in the case of sample treated for 3 minutes (scale bar 100 nm) and **(b)** in the case of sample treated 13 minutes (scale bar 50 nm).

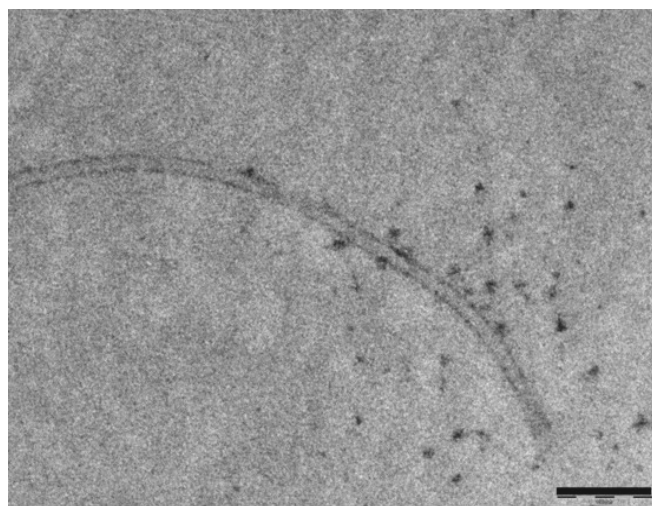


**Fig. 7.** TEM image of CNs and possible carbon nanowires (CNWs) produced in presence of metal ions (Mg). (Scale bar: 100 nm)

Interestingly, when a small amount of metal ions were present in solution, we discover that beside with formation of spherical CNs, a significant amount of carbon atoms are redirected to the formation of different carbon nanostructures like nanowires or nanotubes, as indicated in TEM image in Figure 7. This is an interesting result and the effect of metallic ions in solution and the role of the gas in the synthesis reactor will be addressed in future studies. For instance, when the reaction vial was purged

with Ar gas, the reaction does not produce any CNs but a large amount of a white, sticky and non fluorescent solution. The complex science of microwaves chemical reactions exceed the aim of the present study and can be found elsewhere [11].

The results of spectroscopic and microscopic measurements confirm the synthesis of carbon particles which exhibit all optical properties of true CNs. The as-synthesized CNs absorb light in the entire UV spectrum with two representative bands at around 230 nm (electronic transitions inside the aromatic core domains) and 280 nm (attributed to electronic transitions between states of the aromatic domains inside particles and states associated to surface functional groups). The comparative UV-Vis spectra of as prepared samples (Figure 4) are typical for passivated CNs and indicate an increased production of particles during the first 11 minutes (increased peaks intensity) and the prevalence of the Oswald ripping process lately (growing of larger particles on behalf of smaller particles).

## CONCLUSIONS

We reported the production of CNs by microwave-assisted hydrothermal (MAH) reaction of aqueous glucose solutions and their characterization by spectroscopic and microscopic methods. As first result we highlight the advantage of using a MAOS equipment relative to equipment operating in open atmosphere without full control over the reaction parameters. Secondly we define the setup parameters for a reliable synthesis of CNs and revealed that in a specific experimental arrangement the equipment can produce various carbon-based nanomaterials like carbon nanofibers and nanotubes.

## References

1. A.P. Demchenko and M.O. Dekaliuk, *Methods Appl. Fluoresc.* 1, 042001 (2013)
2. P. Lindstroem, J. Tierney, B. Wathey and J. Westman, *Tetrahedron*, 57, 9225-9283 (2001)

3. M. B. Gawande, S. N. Shelke, R. Zboril, and R. S. Varma, *Acc. Chem. Res.*, **47**, 1338–1348 (2014).
4. N. Puvvada, B N P Kumar, S. Konar, H. Kalita, M. Mandal and A. Pathak, *Sci. Technol. Adv. Mater.* **13**, 045008 (2012)
5. S. Sahu, B. Behera, T. K. Maiti and S. Mohapatra, *Chem. Commun.*, **48**, 8835–8837 (2012)
6. Z. L. Wu, P. Zhang, M. X. Gao, C. F. Liu, W. Wang, F. Leng and C. Z. Huang, *J. Mater. Chem. B*, **1**, 2868 (2013)
7. P.-C. Hsu, Z.-Y. Shih, C.-H. Lee and H.-T. Chang, *Green Chem.*, **14**, 917 (2012)
8. L. Tang, R. Ji, X. Cao, J. Lin, H. Jiang, X. Li, K. S. Teng, C. M. Luk, S. Zeng, J. Hao, and S. P. Lau, *ACS Nano*, **6**, 5102–5110 (2012).
9. H. Richter, J.B. Howard, *Progress in Energy and Combustion Science*, **26**, 565–608 (2000)
10. X. Chen, W. Zhang, Q. Wang, J. Fan, *Carbon*, **79**, 165-173 (2014)
11. I. Bilecka and M. Niederberger, *Nanoscale*, **2**, 1358-1374 (2010)

